PONTIFÍCIA UNIVERSIDADE CATÓLICA
DO RIO DE JANEIRO

Felipe Pinheiro Teixeira

Mechanical Behavior of Natural Fiber Cement Based Composites for Structural Applications

Tese de Doutorado

Thesis presented to the Programa de Pós-Graduação em Engenharia Civil of PUC-Rio in partial fulfilment of the requirement for the degree of Doutor em Engenharia Civil.

Advisor: Prof. Flávio de Andrade Silva

Rio de Janeiro
August 2020

PONTIFÍCIA UNIVERSIDADE CATÓLICA
DO RIO DE JANEIRO

Felipe Pinheiro Teixiera

Mechanical Behavior of Natural Fiber Cement Based Composites for Structural Applications

Thesis presented to the Progama de Pós-Graduação em Engenharia Civil of PUC-Rio in partial fulfilment of the requirement for the degree of Doutor em Engenharia Civil. Approved by the undersigned Examination Committee.

Prof. Flávio de Andrade Silva
Advisor
Departamento de Engenharia Civil e Ambiental – PUC-Rio

Prof. Daniel Carlos Taissum Cardoso
Departamento de Engenharia Civil e Ambiental – PUC-Rio

Prof. José Roberto Moraes d'Almeida
Departamento de Engenharia Química e de Materiais – PUC-Rio

Prof. Conrado de Souza Rodrigues
Centro Federal de Educação Tecnológica de Minas Gerais – CEFET-MG

Prof. Holmer Savastano Junior
Universidade de São Paulo – USP

Rio de Janeiro
August 14th, 2020

Felipe Pinheiro Teixeira

Bechelor of Architecture and Urbanism at Universidade da Amazônia in 2011 and Master of Mechanical Engineering at Universidade Federal do Pará in 2015. The area of interest encompasses natural fibers, cement-based composites, and experimental research.

Bibliographic data

Teixeira, Felipe Pinheiro

Mechanical Behavior of Natural Fibers Cement Based Composite for Structural Applications / Felipe pinheiro Teixeira; orientador: Flávio de Andrade Silva – 2020.

118 f.: il. color.; 30 cm.

Tese (doutorado) – Pontifícia Universidade Católica do Rio de Janeiro, Departamento de Engenharia Civil e Ambiental, 2019.

Incluir bibliografia.

1. Engenharia Civil e Ambiental – Teses. 2. Fibras naturais. 3. Compósitos à base de cimento. 4. Caracterização mecânica. 5. Ensaios estruturais. I. Silva, Flávio de Andrade. II. Pontifícia Universidade Católica do Rio de Janeiro. Departamento de Engenharia Civil e Ambiental. III. Título.

CDD: 624

Acknowledgment

To Prof. Flávio Silva, my advisor, for the trust, encouragement, and all the great discussions. His contribution was fundamental to my academic and personal improvement.

To the technical staff of LEM-DEC, for their skillful and fraternal dedication. Their expertise was crucial for the running of this research.

To my parents, for all their efforts in making my dreams come true. It would not have been possible without their unconditional care.

To Fernanda Salgado, my lifemate, for cherishing my heart and easing the difficulties. Our shared path is a fortune, which undoubtedly makes me feel complete.

To the friendships I made during this period and those of long-standing. For the moments of relaxation, outbursts, and advice, which were essential to mitigate the work. Their contribution, direct or indirect, was of great value and will not be forgotten.

This study was financed in part by the Coordenação de Aperfeiçoamento de Pessoal de Nível Superior – Brasil (CAPES) – Finance code 001.

Abstract

Teixeira, Felipe Pinheiro; Silva, Flávio de Andrade (Advisor). **Mechanical Behavior of Natural Fiber Cement Based Composites for Structural Applications**. Rio de Janeiro, 2020. 118p. Doctoral Thesis – Department of Civil and Environmental Engineering, Pontifícia Universidade Católica do Rio de Janeiro.

This work experimentally discusses the use of natural fibers in cement-based composites for the strengthening of concrete structural elements. For such, the morphology and durability of curauá, hemp, and sisal fibers were analyzed, as well as their mechanical properties. Among the studied fibers, the curauá presented the best performance, which justified its implementation as reinforcement for cement-based composites. For the composite design, it was decided that the volume of fibers would be applied splitted into three parallel layers, in a longitudinally aligned arrangement, like a unidirectional fabric. A layer of this fabric was performed under a tensile test aiming to better understand its mechanical behavior. The cement-based composites reinforced with curauá fabric were mechanically characterized by tensile, bending, combined load compression, and shear tests. After the investigation at the material level, the developed composite was applied over the surface of structural beams as laminates, seeking to provide its strengthening under two distinct loading conditions: bending and shear. The experimental results of the structural tests were confronted with analytical models for comparison. The composites showed a high mechanical performance, achieving the strain-hardening behavior in all cases. When used as a structural reinforcement, the composite provided to the beams increases of strength and ductility. It was also observed a yielding delay in the steel reabars.

Key-words

Natural fibers; Cement based composites; Mechanical characterization; Structural tests.

Resumo

Teixeira, Felipe Pinheiro; Silva, Flávio de Andrade (Orientador). **Comportamento Mecânico de Compósito à Base de Cimento Reforçado com Fibras Naturais para Aplicações Estruturais.** Rio de Janeiro, 2020. 118p. Tese de Doutorado – Departamento de Engenharia Civil e Ambiental, Pontifícia Universidade Católica do Rio de Janeiro.

Este trabalho discute experimentalmente a utilização de fibras naturais em compósitos cimentícios para o reforço de elementos estruturais de concreto. Para tal, foram analisadas a morfologia e a durabilidade de fibras de curauá, cânhamo e sisal, bem como suas propriedades mecânicas. Dentre as fibras estudadas, o curauá apresentou o melhor desempenho, o que justificou sua implementação como reforço nos compósitos cimentícios. Para o projeto do compósito, foi decidido que o volume de fibras seria aplicado dividido em três camadas paralelas, em um arranjo alinhado longitudinalmente, como um tecido unidirecional. Os compósitos cimentícios reforçados com tecido de curauá foram mecanicamente caracterizados por testes de tração, flexão, compressão e cisalhamento. Após a investigação no nível material, o compósito desenvolvido foi aplicado sobre a superfície das vigas estruturais como um laminado afim de aumentar a capacidade portante sob duas condições de carregamento: flexão e cisalhamento. Os resultados experimentais dos ensaios estruturais foram confrontados com modelos analíticos para comparação. Os compósitos apresentaram um comportamento mecânico de alta performance, tendo alcançado o comportamento *strain-hardening* em todos os casos. Como reforço estrutural, o compósito proporcionou às vigas aumentos de resistência e ductilidade. Foi observado também um atraso no escoamento dos vergalhões de aço.

Palavras-chave

Fibras naturais; Compósitos à base de cimento; Caracterização mecânica; Ensaios estruturais.

Summary

List of Figures

List of Tables

1. Introduction

1.1. Motivation

The use of natural fibers as reinforcement in cement-based matrices is presented as an economical and ecologically friendly alternative for the future of the construction industry. Many authors [1–9] described that this kind of composite material exhibits durability and excellent mechanical behavior, presenting increases of strength and strain capacity after the first crack, due to the multiple-cracking ability. However, even showing a high mechanical potential, its applications still limited to elements such as tiles [10–12], paving blocks [13,14], or non-structural masonry [15–17].

Therefore, to fill this gap, the present work develops and analyzes a cementitious composite reinforced with natural fibers, aiming its application as a structural reinforcement, evaluating its contribution to the strengthening of concrete elements.

1.2. Objectives

The present work seeks to study the use of a cementitious composite reinforced with natural fibers applied as a structural reinforcement. For this, three stages were developed: 1) the analysis of the morphology, mechanical strength, and durability of natural fibers; 2) the development and mechanical characterization of a composite reinforced with natural fibers; and 3) the application of this new natural fiber-composite as a reinforcement of structural elements and the characterization of its mechanical contribution.

This study seeks to explore the mechanical characterization of the composite to understand its failure mode and cracking processes, correlating its behavior at the material level to the structural performance and, finally, proving its potential for use.

1.3. Work Organization

Chapter 1: *Introduction*

This chapter presents the thesis motivation and objectives.

Chapter 2: *Literature Review*

This chapter presents a literature review on 1) natural fibers; 2) cementitious composite; and 3) natural fibers reinforced cement-based composites. It presents information about mechanical behavior, durability, and application of fibers reinforced composites.

Chapter 3: *Degradation Mechanisms of Curaua, Hemp, and Sisal Fibers Exposed to Elevated Temperatures*

This chapter presents the influence of elevated temperatures on mechanical behavior and morphology of different natural fibers. The thermal influence is discussed in a microstructural basis.

Chapter 4: *On the Use of Natural Curauá Reinforced Cement Based Composites for Structural Applications*

This chapter shows an investigation about mechanical behavior and cracking mechanisms of a cementitious composite reinforced with natural fiber, towards its use as reinforcement for a structural concrete element.

Chapter 5: *On the Shear Behavior of Natural Curauá Reinforced Cement Based Composite Systems*

This chapter seeks to comprehend the shear mechanical behavior of a cementitious composite reinforced with natural fibers and its application as a shear structural reinforcement.

Chapter 6: *Conclusions*

This chapter presents a general briefing on the issues discussed in the thesis.

2. Literature Review

2.1. Natural Fibers

The natural fibers can be primarily divided by their origins: vegetable, animal, and mineral [18,19]. The vegetable fibers have been used in composite research investigations [9,20–22] due to their properties like tensile strength and strain capacity. The natural fibers can be obtained from many parts of different plants (**Table 2-1**).

Table 2-1. Examples of natural fibers and where in the plant it is obtained (Kiciska-Jakubowska et al. [23]).

Fiber Plant	Obtained From
Flax (*Linum usitatissimum*)	Bast
Hemp (*Cannabis sativa*)	
Jute (*Corchorus capsularis*)	
Curaua (*Ananas erectifolius*)	Leaf
Palm (*Eleias guineensis*)	
Sisal (*Agave sisalana*)	
Cotton (*Gossypiun hirsutum*)	Seed
Poplar (*Populus tremula*)	
Coir (*Cocus nucifera*)	Fruit
Luffa (*Luffa aegyptiaca*)	
Bamboo (*Bambusa shreb.*)	Grass and Reed
Totora (*Scirpus californicus*)	

2.1.1. Mechanical, Morphological and Chemical Characteristics

The natural fibers are formed mainly by cellulose, hemicellulose, and lignin. According to Yan at al. [19], cellulose is a natural polymer whose glucose molecules form long and aligned chains that unit in bundles called microfibrils. The cellulose is a semicrystalline polysaccharide with a large amount of hydroxyl, which attributes to the fibers a hydrophilic nature (low resistance to the increase of humidity). Hemicelluloses are polysaccharides interspersed with the microfibrils, which has an open and completely amorphous structure with a large amount of hydroxyl and acetyl. The hemicelluloses are also hydrophilic and strongly bonded

to cellulose by hydrogen bonds. The lignin is a complex amorphous polymer made by aromatic hydrocarbons, which has a low water absorption capacity and provides rigidity to plants, acting as an adhesive within and between fibers.

Each microfiber is composed by a complex layered structure, formed by a primary cell wall, three secondary cell walls and the lumen. According to many authors [18,19,24,25], at the primary wall the microfibrils are disorderly arranged, similar to a reticulated mesh. The secondary walls (intermediary regions: S1, S2, and S3) determine the mechanical properties of the fiber; it has a helical arrangement of cellulose microfibrils immersed in a matrix of hemicellulose and lignin. The lumen makes the microfiber hollow, and may have different sizes [26], as shown in **Fig. 2-1**.

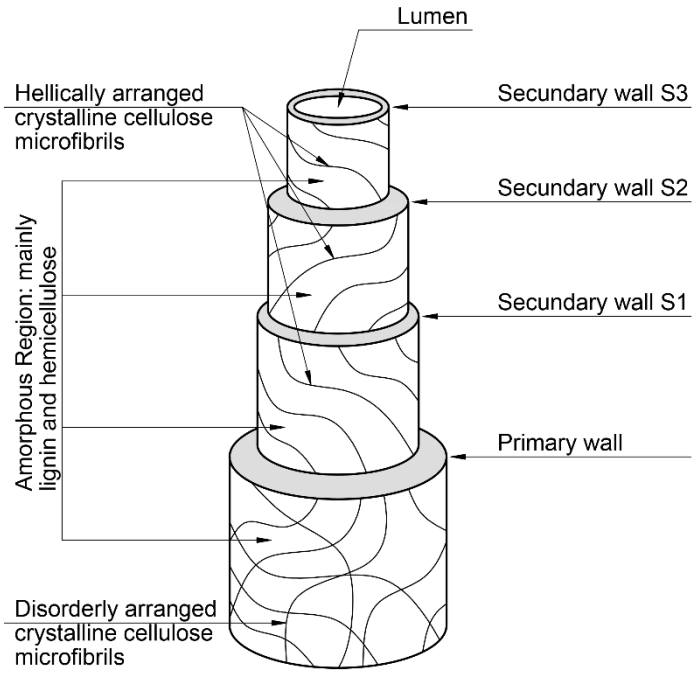

Figure 2-1. Structure of a microfiber, adaptaded from Azwa et al. [18].

The chemical composition of natural fibers is directly influenced by its species, its geographical and climatic conditions, and the maturity of the plant. **Table 2-2** shows the chemical composition of some natural fibers.

Table 2-2. Chemical composition of different natural fibers.

Fiber	Cellulose (%)	Hemicellulose (%)	Lignin (%)	Ref.
Bamboo	34.5	20.5	26.0	Yan et al. [19], Komuraia et al [8]
Curaua	81.0	20.0	4.0	Yan et al. [19], Komuraia et al [8]

Hemp	58.8	23.8	14.7	Ferreira et al. [27], Pereira [28]
Jute	61.0 – 71.0	13.6 – 20.4	12.0 – 13.0	Ferreira et al. [27], Khan and Khan [29]
Sisal	73.0	10.1	7.6	Sydenstricker et al. [30], Silva et al. [6]

The chemical composition of the natural fibers directly influences their mechanical properties, since the cellulose, the hemicellulose, and the lignin are mainly responsible for its mechanical adhesion and degradation [18]. Another important variable that influences the mechanical properties of the natural fibers is the angular orientation of the microfibril. The microfibrillar angle is the difference between the longitudinal axis of the fiber and the angle of their microfibrils. Smaller angles provide greater strength and stiffness, while larger angles make the fibers more ductile [18,19].

All this complexity at the physical arrangement of natural fibers can lead to a huge variety of mechanical and morphological characteristics in the same species and, especially, among species. Properties such as density, diameter, microfibrillar angle, and moisture gain have a direct influence on the strength of the fibers. **Table 2-3** and **Table 2-4** show some physical and mechanical characteristics of different natural fibers, respectively.

Table 2-3. Physical characteristics of different natural fibers.

Fiber	Density (g/cm^3)	Diameter (µm)	Microfibrillar Angle (Degree)	Moisture Gain (wt%)	Ref.
Bamboo	0.6 – 1.1	25 – 40	–	–	Yan et al. [19], Komuraiah et al. [8],
Curaua	–	25 – 600	6	12	Ferreira et al. [27], Silva et al. [6].
Hemp	1.4	7 – 10	–	–	Dittenber and Gangarao [31],
Jute	1.3 – 1.5	20 – 200	8	12.5 – 13.7	Onuaguluchi and Banthia [32],
Sisal	1.3 – 1.5	8 - 200	10 – 22	10 – 22	Spinacé et al. [33]

Table 2-4. Mechanical characteristics of different natural fibers.

Fiber	Tensile strength (MPa)	Young's Modulus (GPa)	Strain-to-Failure (%)	Ref.
Bamboo	140 – 800	11.0 – 32.0	2.5 – 3.7	Yan et al. [19], Komuraiah et al. [8],
Curaua	270 – 900	23.5 – 90.0	1.0 – 3.5	Ferreira et al. [27], Silva et al. [6].
Hemp	87 – 1150	11.8 – 96.0	1.3 – 4.9	Dittenber and Gangarao [31],
Jute	320 – 800	8.0 – 78.0	1.0 – 1.8	Onuaguluchi and Banthia [32],
Sisal	363 – 700	9.0 – 38.0	2.0 – 7.0	Spinacé et al. [33]

2.1.2. Durability

The major challenge about the use of natural fibers as an engineering material is its durability. Being a natural compound, formed by biodegradable components, natural fibers need some specific controls as thermal restrictions, moisture absorption precaution, chemical control, and care about low resistance to fungi and bacteria.

The pyrolysis characteristic of vegetables is related to their chemical composition. Separately, the components of natural fibers (cellulose, hemicellulose, and lignin) present thermal degradation at different temperatures, so the variation of these components in the chemical constitution of each species will influence its durability. In general, most natural fibers show up to 60% loss of mass at temperatures between 215 - 310 ° C [34]. The **Table 2-5** presents some natural fibers pyrolysis data, commonly shown in three stages.

Table 2-5. Natural fibers pyrolysis data.

Stage 1	Stage 2	Stage 3	Ref.
–	300 °C Despolimerização da hemicelulose e da ligação glicosídica.	360 °C Thermal degradation of α-cellulose.	Alvarez and Vázquez [35]
215 °C Lignin degradation.	290 °C Decomposition of hemicellulose.	340 °C Decomposition of α-cellulose.	Manfredi et al. [36]
0 – 250 °C Start of degradation.	250 – 420 °C Up to 72% of mass loss.	420 – 520 °C Ash content is approx. 20%.	Martin et al. [37]
290 °C Hemicellulose degradation.	320 °C Lignin degradation.	350 °C Cellulose degradation.	Krishnaiah et al. [38]

Among the components of natural fibers, hemicellulose is the main responsible for moisture absorption. Spinacé et al. [33] exposed curauá fibers to a temperature of 100 °C for 50 min and noticed that the moisture content decreased from 9.10 to 8.30 wt%. It is also important to know how long it takes to the fiber to reabsorb the moisture, as this information can be used to evaluate its handling time under specific conditions and the final properties of the material. The fibers of Curauá in conditions of relative humidity equal to 54.5% and temperature corresponding to 25 ° C showed a high absorption rate during the first 24h [33].

Studies on the wetting and drying process (hornification) of sisal fibers [39,40] showed that, after ten cycles, the fibers show a 30% loss in their humidity absorption capacity. It is explained by the stiffening of its polymeric structure during the process when the cellulose polysaccharide chains are rearranged closely due to the loss of water during drying, causing the approach of the microfibrils. The capillary voids of the fibers are progressively closed during drying process and can no longer be completely reopened with a new humidification cycle. Therefore, the dimensional variation is related to the loss of the absorption capacity (**Fig. 2-2**), where is possible to note the reduction of the lumens and, consequently, changes in their physical properties associated with densification of the cross-section.

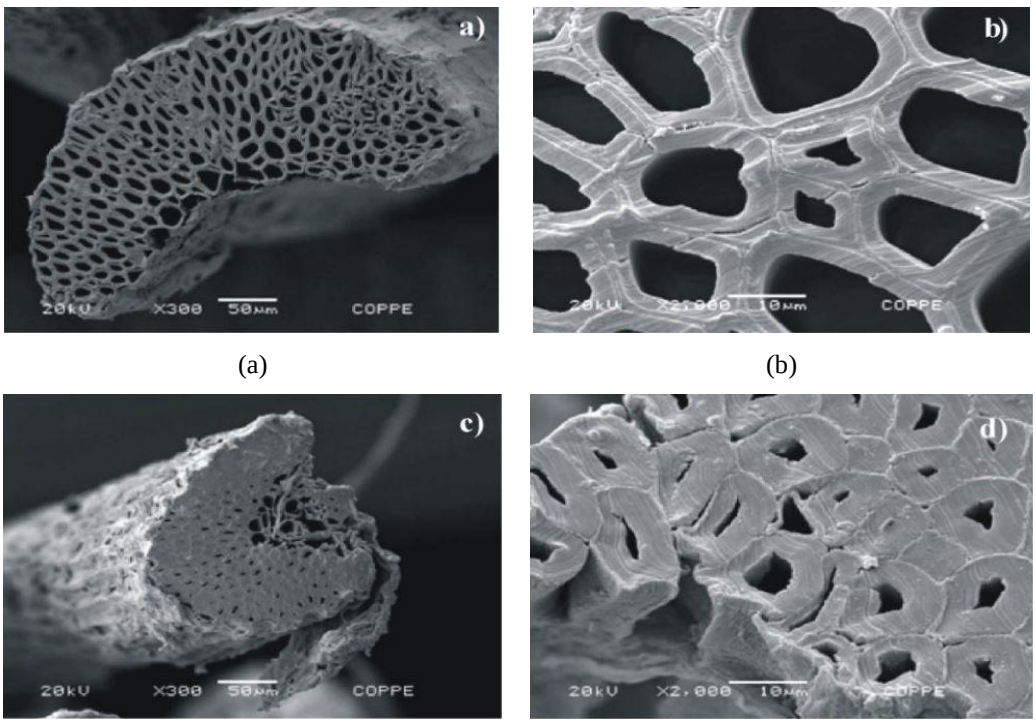

(a) (b)

(c) (d)

Figure 2-2. Cross-section of sisal fibers: (a, b) without treatment, and (c, d) after the hornification where it is possible to note the dimensional variation of lumens (Ferreira et al. [39,40]).

However, it is known that the high moisture content swells the cell walls until the fiber is saturated. From this point, the additional content no longer causes the fiber size to increase and behaves like free water between its empty spaces [33]. This mechanism influences the chemical degradation of the fiber, changes physical and mechanical conditions, and also increases the possibilities of biodegradation by bacteria [41].

High levels of temperature and moisture content make the natural fibers susceptible to biological degradation by microorganisms. These microorganisms cause the degradation of cellulose, decreasing its mechanical properties, and causing a bad odor, which also compromises the purity of the air [42]. Lignin is more stable thanks to its chemical structure; however, the other components of cellulosic fibers also decompose easily under the action of aerobic and anaerobic bacteria. In this context, the optimal conditions for the proliferation of fungi include relative humidity ranging between 70 and 90%, temperature between 24 °C and 30 °C and a pH around 6.0 [42].

Regarding the chemical control, it is worth to mention alkaline degradation, which means hemicellulose and lignin degradation due to the existence of calcium hydroxide (CH). Hemicellulose and lignin are responsible for the structural bonding of microfibrils, so their degradation can lead to microfibers' mechanical properties reduction. According to literature reports [19,43], the alkaline degradation can be divided into four stages: 1) degradation of lignin and part of hemicellulose, making its structures exposed to the alkaline solution present in the pores and the matrix phase itself; 2) hemicellulose degradation, which causes the decrease of integrity and stability of the cell walls; 3) after the degradation of lignin, hemicellulose, and intramolecular hydrogen bonds, there only remains unbonded micro-fibers, resulting in a macro-fiber structural collapse, which accelerates the degradation of cellulose; 4) the last step is the failure of cellulose micro-fibrils, which is caused by alkaline hydrolysis of amorphous regions containing non-reducing end, and leads to the complete degradation of the cellulosic fiber.

It is important to emphasize that, although alkalinity causes the degradation of cellulosic fibers, the controlled process of alkalinization can be used to reduce

its ability to absorb moisture and improve its interfacial adhesion. The alkaline treatment, commonly done with potassium hydroxide (KOH) or sodium hydroxide (NaOH), reduces the hydrogen bonds of cellulose, eliminating open hydroxyl chains that connect with the water molecules [44]. However, after the alkalinization process, the natural fibers must be carefully washed, otherwise, the alkali will continue to contribute to its degradation. In this context, Wong et al. [45] evaluated the effect of the alkalinization process on bamboo fibers immersed in NaOH concentrations of 1, 3 and 5% for a period of 24 hours, then washed with water and air-dried for another 24 hours. After treatment, the fibers subjected to a concentration of 1% (**Fig. 2-3b**) showed a reduction of impurities on the surface. For the fibers treated with a concentration of 3% (**Fig. 2-3c**), it is possible to notice the appearance of some cavities indicating that the NaOH has removed much of the soluble substance from these layers. The fibers conditioned to the 5% content of NaOH (**Fig. 2-3d**) revealed a surface quite different from that without treatment (**Fig. 2-3a**), which presented a higher porosity and roughness. Mechanically, the treated fibers showed a decrease in stiffness and an increase in ductility when compared to those without treatment.

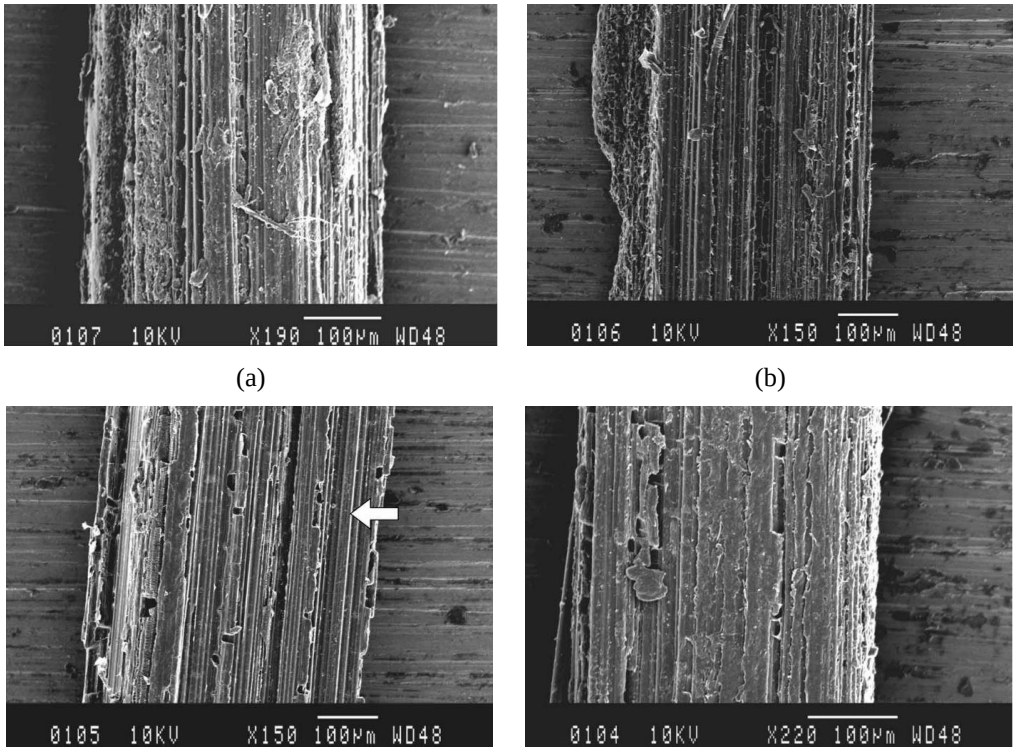

(a) (b)

(c) (d)

Figure 2-3. Scanning electron microscopy of untreated bamboo fibers (a) and treated with a concentration of 1% (b), 3% (c) and 5% (d) of NaOH (Wong et al. [45]).

Sari et al. [46] evaluated the chemical, physical, and mechanical effects of the treatment of NaOH on fibers from corn husks. The different NaOH treatments increased the α-cellulose content to 47.59% to 62.87% and decreased the hemicellulose and lignin contents to 27.28% to 13.62% and 8.98% to 5.55%, respectively. The loss of hemicellulose and lignin in the fibers upon alkali treatment increased the fiber density; treatments with 0.5%, 1%, 2%, 5%, and 8% NaOH provided fiber densities of 0.43, 0.56, 0.58, and 0.61 g/cm^3, respectively. The tensile properties of the fibers improved after all the alkali treatments. Compared to the reference samples, the fibers treated with 0.5%, 1%, 2%, 5%, and 8% NaOH exhibited improvements in tensile strength of approximately 39.6%, 43.8%, 10.03%, 47.9%, and 129.5%, respectively. The authors [46] concludes that the alkali treatment with NaOH removes hemicellulose and lignin from the fibers, resulting in decreased moisture content, more dominant cellulose content, higher crystallinity index, rougher fiber surface, and smaller lumen size inside the fiber bundles, as well as reduced fiber diameter. As a result, mechanical strength and thermal resistance become higher.

The natural fibers have excellent mechanical behavior, but a short service life when compared to synthetic fibers. However, many effective methods have already been developed aiming to extend its durability.

2.2. Cementitious Composites

The use of fibers as the cementitious matrix reinforcement started between the 60s and 70s, initially being used as a substitute for secondary reinforcement or for crack control in less critical parts of the construction, but today it is widely applied in industrial installations, shotcrete, and in precast structures [47–49]. Its main characteristic is the higher tensile strain capacity when compared to conventional concretes and mortars, which present the propagation of a single large crack. The fiber cement-based composite mainly presents two distinct mechanical behaviors: the strain hardening and the strain softening. The strain hardening occurs when, after the first crack, the material shows an increase in strain capacity without losing strength, that is why it is called Strain Hardening Cement Composites

(SHCC). Otherwise, if the material presents a single crack opening, it is called strain softening. Wittmann et al. [50] explain that the composites with such superior tensile responses can be engineered by tailoring the composite ingredients with the aid of micro-mechanically based formulations [51]. This has led to the terminology Engineered Cementitious Composites (ECC) or Strain Hardening Cement-based Composites (SHCC).

2.2.1. Mechanical Behaviour

The main property of SHCC is the capacity to present (after the linear elastic zone) a pseudo ductile behavior when mechanically loaded, unlike conventional concretes and mortars. It occurs because the fibers, after the first crack, act as a bridge across the matrix [51,52]. It can increase the composite strength by the load transfer across the crack (when fibers connect two separated matrix parts and transfer its load). When it provides gains of strength at the stress-strain curve after first cracking, this behavior is called strain hardening. The fibers increase the composite toughness providing the energy absorption mechanisms, by deboning and fiber pullout [51,52].

The strain softening is a behavior in which the tensile or flexural strength, after the linear-elastic zone, became only residual strength along the strain, presenting a single crack opening. The magnitude of these stresses and the mechanical response of fiber-reinforced cementitious composites, in general, strongly depend on the type and volume fraction of fiber (V_f). If a low amount of fibers ($V_f < 1\%$) is added to the cementitious matrix, the post-peak behavior of composite does not differ very much from that of the plain matrix. In the case of high fiber volume fraction ($V_f > 2\%$), the specimens show a strain hardening behavior after the first crack formation. As a result, the strength of the composite is higher than that at first cracking [53]. **Fig. 2-4** presents a schematic classification of tensile behaviour of fiber-reinforced cementitious materials.

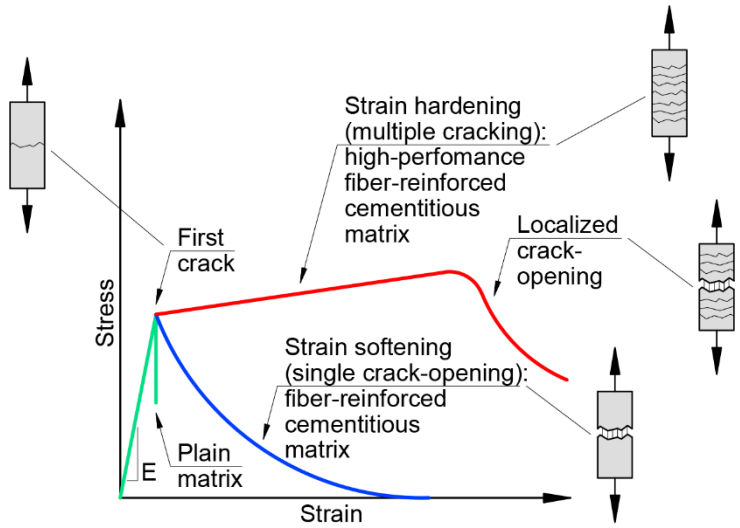

Figure 2-4. Classification of tensile behaviour of fiber-reinforced cementitious materials.

When a tensile load is applied to a fiber-reinforced composite, made by a low-modulus matrix reinforced with high-strength and high-modulus fibers, some of this loading is transferred from the matrix to the fibers. It will inhibit the formation of macro-cracks, which is replaced by sequential micro-cracks, responsible for the increase of material strength [52,54]. At the cracking moment, aim to avoid the catastrophic failure, the fibers load-bearing capacity ($\sigma_{fu}V_f$), must be higher than the load on the composite at first crack. This elastic quantification is presented by **Equation 2-1** [52]:

$$\sigma_{fu}V_f > E_m\varepsilon_{mu}V_m + E_f\varepsilon_{mu}V_f \qquad \textbf{(Equation 2-1)}$$

If this condition is fulfilled, meaning the fiber volume is sufficient, the cementitious composite will not present a brittle failure (as the plain matrix) after the first crack formation. The ductility will be increased, and the tensile strain capacity will be significantly improved as the critical crack opening. After the first crack, the failure will be marked by the fibers pullout followed by its deformation and broken. Also, considerable energy dissipation can be noticed [52,54,55].

The strain hardening behavior can also be described by five distinct stages of the stress-strain curve [4,56,57]: Stage I corresponds to the linear-elastic range where both matrix and fiber behave linearly, which ends by the first crack formation when the bend over point (BOP) is reached; Stage II describes the start of the first crack (BOP-) to its end (BOP+), after its propagation across the width of the sample;

Stage III exhibits a stiffness decreases due to the formation of distributed cracks at regular intervals and, after the total amount of cracks is done, the progressive debonding takes place to the fibers pullout at Stage IV; finally, the post-peak response occurs in Stage V, which only presents the residual strength (softening branch). This behavior during the failure of SHCC involves the development of stress bridging along the cracked faces, providing strain capacity without losing strength, as presented in **Fig. 2-5**.

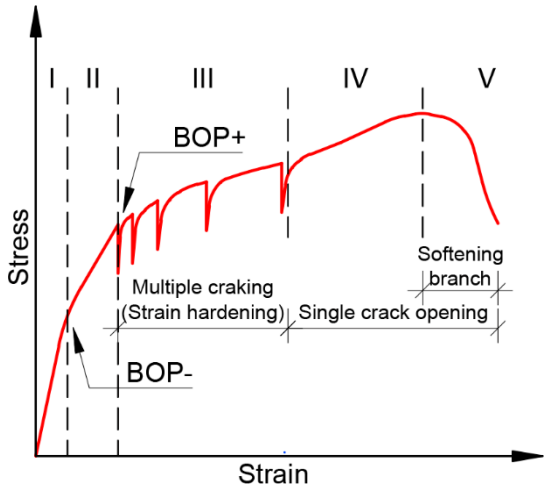

Figure 2-5. SHCC mechanical behaviour, based on Yao et al. [56], Silva et al. [4],and Mobasher et al. [57].

2.2.2. Fiber-Matrix Interface

According to Lofgren [54], the strength of cement-based materials is related to its microstructure. The mainly responsible for this microstructural development is the hydration reaction, process by which Portland cement becomes a hardened mass after the water addition. During the early stages (up to 24 h), approximately 30 % of the hydration occurs, and after about 24 h the heat rate of the reaction (exothermic) declines. The addition of fibers does not change the hydration reactions or the microstructure in the matrix. However, the pull-out behavior and the fiber bond are significantly influenced by the microstructure at the interface between the fiber and the matrix, which is called the Interfacial Transition Zone (ITZ). **Fig. 2-6** shows a schematic description of the ITZ.

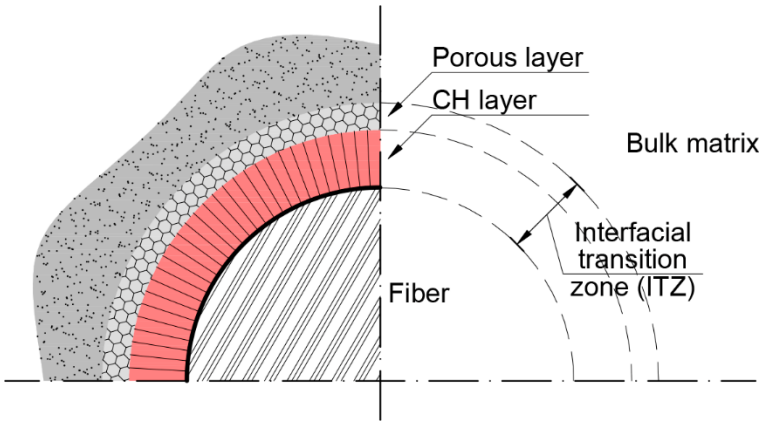

Figure 2-6. Schematic description of the ITZ, adapted from Lofgren [54].

The ITZ presents the formation of a higher CH crystals amount, and its resistance is substantially lower when compared to the bulk matrix. This region is deficient in the content of cement particles and therefore has a substantially higher porosity than the bulk matrix [58]. Bentur and Mindess [52] estimated that the interfacial transition zone in a typical concrete is 20-50 μm thick. Wang et al. [59] affirm that, although the size of the ITZ varies with different fiber types and size, as well as matrix details, most observations suggest a relatively large porous and weak layer on the order of 40 μm to 70 μm thickness. Xu et al. [60] presented that the steel fiber-matrix ITZ was nearly 30 μm wide, while polypropylene fiber-matrix ITZ's thickness was approximately 15 μm.

The density and packing of the ITZ are related to several conditions such as fiber size in comparison to the other constituents of the matrix, degree of the matrix packaging, and roughness and chemistry of the fibers' surface [52,58]. Some techniques aiming to improve the fiber-matrix interaction have proved to be very useful, such as: changing the chemical composition of the matrix directing to decrease the concentration of free CH, and consequently its crystalline formations and porosity [61]; and the improvement of the mechanical anchoring of fibers by their shape [52].

In the case of natural fibers, their roughness surface and variable shapes can improve the adhesional and frictional bond strength, playing an important role in the mechanical adhesion [5]. Investigations about the morphology of natural fibers [5,62] presented three typical cross-section shapes: horse-shoe shape, arched shape, and twisted shape. Castoldi et al. [63] and Ferreira et al. [64] observed that the sisal

fibers load after the beginning of the debonding remains considerably constant, governed by frictional shear strength, and continues until the complete fiber pullout.

2.3. Natural Fibers Reinforced Cement Based Composites

2.3.1. Mechanical Behaviour

The application of natural fibers as cementitious composites reinforcement has demonstrated a high-level mechanical response, mainly related to the cracks' control, preventing their propagation and providing a ductile behavior to the material. The fibers' irregular shape and naturally rough morphology can provide high mechanical adhesion to the cementitious matrix. An experimental investigation performed to understand the pullout behavior of sisal fibers from a cement matrix [5] presents that the general cross-section of the fibers can be distinguished into three types of shapes that alter the interfacial mechanical response: 1) Horse-shoe shape – located in the periphery of the leaf, these represents the majority of the fibers that can be found in the sisal plant. 2) Arched shape – located in the center part of the sisal leaf in a lower proportion than the horse-shoe shape. 3) Twisted arch shape – which is a result of the fiber extraction process. The highest values of bond stress were found for the twisted arch fiber type with an average adhesional and frictional bond strength of 0.92 and 0.42 MPa, respectively. For comparison, polypropylene fibers presented adhesional bond strength of 0.5 MPa [65].

Asprone et al. [66] presented the mechanical behavior of the bond between the hemp fibers and the cementitious matrix. It was adopted a three-embedment length (10 mm, 20 mm, and 40 mm), and an average adhesional bond strength from 1.02 MPa to 2.20 MPa was found. Fidelis [67] analyzed the adhesional bond strength of fiber jute filaments embedded in a cementitious matrix with 3 mm, 5 mm, and 10 mm of lengths. The 10 mm embedded sample presented the highest result, with 0.41 MPa, and it has been noted an increased adhesional strength with embedment length.

As presented, the natural fibers showed an optimum interaction response to the cementitious matrix and can be viably used as a component of composite materials. Thus, mechanical tests on natural fibers reinforced cement based composites has been deeply explored in many configurations: as the textile form

[20,68,69], in a continuous and aligned way [7,21,70], or short and randomly dispersed in the matrix [9,22,71].

Olivito et al. [72] studied the cementitious matrix reinforced with bidirectional fabrics of flax and sisal fibers. All composite specimens were reinforced with one fabric layer, and the final thicknesses of the samples were 5 mm and 8 mm, each. The results show that the tensile strength of the composites is slightly altered when varying the reinforcing fibers. Thus, flax and sisal fiber composites measuring 5 mm thick achieved tensile strengths of 3.83 MPa and 3.87 MPa, respectively, while their peers measuring 8 mm thick achieved tensile strengths of 2.22 MPa and 2.37 MPa, respectively. Both samples presented ductility behavior through multiple crack distribution. The authors [72] affirm that the strong tensile properties of sisal and flax fibers indicate a high-performance potential of these fabrics in fiber-reinforced composite applications.

Cementitious composites reinforced with 3 and 5 layers of jute fabrics were tested under tensile load [68]. The composites showed a high strain capacity and multiple cracking behavior. The composite reinforced with 3 layers presented 6 cracks while the composites with 5 layers showed 11 cracks. The composite reinforced with 5 layers of fabric supported an ultimate tensile stress 8% higher and strain capacity 8.7 % lower than the composite with 3 layers of fabric.

Souza et al. [21] studied the mechanical behavior of long unidirectional aligned curaua fibers reinforced cementitious composite. Three types of composites were fabricated, with one, three and five fiber layers, and as a result, the fiber volume fractions were 4 %, 7 %, and 8 %, respectively. All the composites presented a strain-hardening behavior with multiple crack formation. An evaluation of the toughness under tensile testing indicates superior values for the five-layered composite (14.7 MPa), which is justified by the greater curaua high volume fraction in the five-layered composite. The one and three-layered composites presented tensile strengths of 6.3 MPa and 9.7 MPa, respectively. The higher strain capacity (five-layered composite) reached the mark of 1.6 %. d'Almeida et al. [70] also studied long unidirectional aligned curaua fibers reinforced cementitious composite, but under flexural tests. The composites presented the deflection-hardening behavior and flexural strength up to 27.5 MPa.

Sadiq et al. [73] analyzed the mechanical behavior of aligned jute strands reinforced lightweight cementitious composite. The most significant used volume

fraction of the strands was approximately 6 % and 8 %, which corresponds to 3 and 4 layers, respectively. The specimens were tested in third-point loading and the results show deflection-hardening with multiple cracking, presenting ultimate load up to 3.5 kN.

Soltan et al. [71] studied cementitious composites reinforced with curaua short-fiber, with the average length varying between 10 mm and 20 mm. The tensile strain softening behavior was observed for the composite reinforced with 2 % by volume fraction of fibers. Fiber bridging capacity with 2 % by volume was not sufficient to generate any multiple cracking behavior. Instead, these specimens failed by the slow opening of the first crack formed in the matrix. However, the 4.4 % volume fraction reinforced composites presented the distributed micro-cracking and strain-hardening behavior, as previously mentioned by Fantilli et al. [53].

Hwang et al. [22] examined the effect of adding random, short coconut fibers to cementitious composites on the mechanical properties, using different volume fractions (0 %, 1 %, 2.5 %, and 4 %). The increase in coconut fiber content from 0 % to 4 % increased the flexural strength of the cementitious sheet and the modulus of rupture from 5.2 to 7.4 MPa and from 6.8 to 8.8 MPa, respectively. The addition of coconut fiber to the composite samples enhanced the first-crack deflection and the toughness indices remarkably. The first-crack deflection increased from 0.23 mm to 0.55 mm when the coconut fiber volume fraction rose from 0 % to 4 %.

In the work about cementitious composites reinforced with short curaua fibers (20 mm length and 4 % volume), Zukowski et al. [9] observed that the composite presented a multiple-cracking pattern (from 2 to 4) and the increased strain capacity in a range of 0.4 % to 0.8 %. The average first crack tensile strength was 1.75 MPa, and the final tensile strength was 1.9 MPa, about 9 % higher. So, the short fibers reinforcement was able to successfully bridge the cracked matrix with new fine cracks formation.

2.3.2. Durability

The natural fibers' durability in the cementitious matrix is deeply associated with its chemical and morphological characteristics. Filho et al. [74] described two types of natural fibers degradation in an alkaline environment: alkaline degradation (as mentioned before) and fiber mineralization. The fiber mineralization means the

migration of calcium hydroxide to the fiber structure, causing cellulose reduction, forming dense hydration products, and consequently decreasing its strength and ductility [75,76].

Mineralization can be divided into two mechanisms: CH mineralization and self-mineralization. The CH mineralization is caused by the migration of calcium hydroxide to the lumens and middle lamella, which induce a fiber volumetric variation by its crystallization and growth within the cell walls, damaging the connections between the fiber components and corroding cellulosic micro-fibrils [43,77,78]. Self-mineralization concerns the hydrolysis rate of amorphous components (lignin and hemicellulose). It is known that the precipitation (formation of solids during a reaction) of hydration products (calcium hydroxide) within the fiber structure is the main reason for cell wall mineralization [43,77,78].

Mohr et al. [78,79] analyzed the effect of wet/dry cycling on pulp fiber-cement composites. The samples were exposed to 1, 2, 5, 10 and 25 wet/dry cycles to verify its properties. It was noted that the highest loss of strength and stiffness occurred in the transition between the second and fifth cycles. An examination of the samples' fracture surface after twenty-five cycles indicated that fibers has becme brittle, probably due to mineralization. An energy dispersive spectroscopy (EDS) showed the transport of hydration products (especially calcium hydroxide) through the lumens, voids, and around the fibers. The authors [78] proposed a degradation mechanism divided into three phases: 1) debonding of the fiber-matrix interface up to the second cycle, 2) re-precipitation of hydration products within empty spaces of the fiber and at the debonded fiber-matrix interface (up to tenth cycle), and 3) weakening of the fibers due to mineralization, which occurs after the tenth cycle.

Although natural fibers do not present high resistance at the presence of calcium hydroxide, it is possible to implement methods that aim to neutralize their degradation under such conditions. The pozzolanic additions to precipitate the calcium hydroxide of the matrix as calcium silicate hydrate, or treatments with a higher concentration of CO_2 to precipitate the calcium hydroxide as calcium carbonate, can eliminate the degradation risks and improve the durability of this kind of composite [80].

Ferreira et al. [2,39] presented a Portland cement replacement by metakaolin (30 %) and fly ash (40 %) for their sisal fibers cementitious composites. The authors justify that such alteration provided a calcium hydroxide free matrix and,

consequently, the higher fibers durability. Wei and Meyer [81] showed by thermogravimetric analyses that the metakaolin (MK) and nanoclay (NC) addition significantly reduced the calcium hydroxide and the ettringite formation. The 30% and 50 % replacements of Portland cement not only improve the composites' strength but also reduce its alkalinity. Another positive effect of the Portland cement partially replacement by metakaolin and nano-clay was the fiber-matrix adhesion, resulting in a pullout energy 131 % and 196 % higher than reference samples. Analysis of fracture surfaces of fiber-reinforced specimens after flexural test indicate that combined replacement of Portland cement by MK and NC not only improves the interface bonding properties of sisal fiber in the matrix, but also prevent the fiber degradation from alkaline attack and CH mineralization.

Lima and Toledo Filho [82] analyzed sisal fibers cementitious composites by thermogravimetric after accelerated aging cycles. At the matrix with Portland cement partially replaced by 30 % of MK the presence of CH was not noticed. The mechanical properties of sisal fibers were maintained, and no evidence of degradation was seen. At the experiments [83] about the use of supplementary cementitious materials for mitigating degradation of natural fiber cementitious composites, the Portland cement was partially replaced by silica fume (SF), ground granulated blast furnace slag (SL), Class F fly ash (FA), Class C fly ash (CA), metakaolin (MK), and blends of calcined diatomaceous earth and volcanic ash (DEVA). All the specimens were analyzed after 1, 2, 5, 10 and 25 wet/dry cycles, and it was found that the use of pozzolans can decrease degradation by moisture retention by 10 % to 70 %, in addition to increase in strength and stiffness.

Wei and Meyer [43] presented an analysis of degradation mechanisms of sisal fiber in the alkaline and mineral-rich environment of cement matrices. By replacing 30 wt.% cement by metakaolin, the durability of sisal fiber-reinforced cementitious composites subjected to wetting and drying cycles was effectively improved. Therefore, it was noticed that an effective way to mitigate the degradation of natural reinforcements is to maintain the pH value of the pore solution at a relatively low level.

Silva et al. [84] analyzed physical and mechanical properties of durable sisal fiber–cement composites. In order to increase the durability of the composites, the Portland cement was replaced by 30% of MK and 20% of calcined waste crushed clay brick (CWCCB). By replacing 50% of Portland cement by the pozzolans, it was possible to develop a matrix that was free of CH at 28 days of age. A calcium (Ca) EDS

mapping was performed in the fiber–matrix interface to verify if leached calcium, from the CH, could have migrate to the interior of the sisal. It was observed a light red color that indicates low amount of Ca (**Fig. 2-7**).

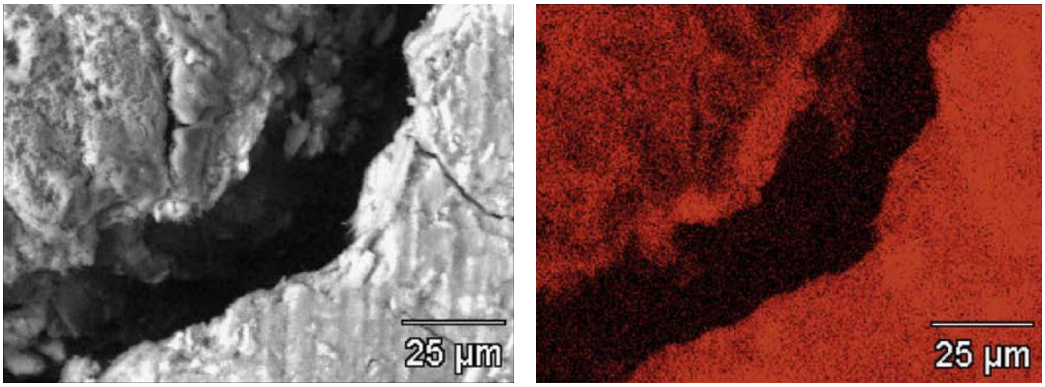

(a) (b)

Figure 2-7. EDS mapped region and (a) EDS mapping for Ca in the fiber–matrix interface (b).

Tonoli et al. [85] presented the effect of carbonation at early stages on fiber–cement composites and its impact on hydration, chemical and dimension stability. The specimens were preconditioned in water-saturated air for 1 h and then submitted to 10 h of accelerated carbonation in a climate chamber. Calcium carbonate polymorphs were observed filling the voids and the pore structure of the carbonated matrix, which resulted in the densification of the matrix. It improves the contact between fibers and cement matrix and thus preventing the movement of water due to the decrease in the pore size network and diffusion of degradation products into the composite. Additionally, another consequence of carbonation at an early age is volume stabilization, as indicated by the lower drying shrinkage and lower porosity.

The partial replacement of Portland cement by pozzolans or carbonation are not the only way to provide higher durability to the natural fibers. Its superficial treatments have also the intention to change their physical and morphological characteristics, aiming to increase their durability and to improve the adhesion of the fiber-matrix interface.

Toledo Filho et al. [86] evaluated immersion of the sisal fibers in a silica fume slurry before its addition to the cementitious matrix. The aligned long sisal fibres were immersed in slurried silica fume for 10 min then air-dried for 15 min. The treatment intended to fill the fiber cavities with silica microparticles, which can eliminate more efficiently the calcium hydroxide. The results showed that the presence of silica at the fiber-matrix interface creates a low alkalinity zone around the fiber, which can prevent fiber degradation by alkaline attack and mineralization.

Ghavami [87] tested the application of water repellents on bamboo and reduced the water absorption capacity from 30% to 4%. The treated bamboo showed higher durability and adherence to the cementitious matrix. Bilbo and Arsene [88] treated sugarcane bagasse fibers with silane aiming to improve their characteristics. The silane impregnated on the fibers formed a chain of polysiloxane molecules, changing its morphology, increasing its dimensions and decreasing its porosity and its water absorption capacity. The silane coating on the fiber surface improved the fiber-matrix interface, showing higher adherence after the cracking of the composite.

2.4. Applications

According to Naaman [89], fiber-reinforced cementitious composites have been used in numerous applications, either as stand-alone or in combination with reinforcing bars and prestressing tendons; they have also been used as support materials in repair and rehabilitation work. **Table 2-6** presents classes of applications of fiber-reinforced cementitious composites.

Table 2-6. Classes of applications of fiber-reinforced cementitious composites, adapted from Naaman [89].

Applications of fiber-reinforced cementitious composites	STAND-ALONE in liht structural elements	e.g., cement boards, sheets, pipes, slabs on grades, paviments, shells, piles, poles, light beans, pre-fab elements, …
	HYBRID in combination with RC, PC or steel structures	e.g., seismic and blast resistant structures, super high-rise structures, offshore structures, space-craft launching plataforms, very long bridges, encased steel trusses, fire protection, …
	HYBRID in selected zones where enheced properties are needed	e.g., beam-column joints in seismic frames, coupling beams, anchorage zones in PC beams, punching shear zone in RC slabs, …
	REPAIR AND REHABILITATION	e.g., tunnel lining, jacketing around columns, fire protection, …

However, the use of fibers for these structural applications is commonly related to synthetic fibers, mainly polymeric and steel, while natural fibers have been focused only on non-structural elements, such as roofing tiles [10,11]. Tonoli

et al. [12] presented a long term study (14 years) about natural weathering exposure of tiles made of natural fiber composite, leading to a better understanding of its degradation processes in a real application condition.

The natural fibers are also used in bricks or paving blocks, aiming to reduce its brittle breaking behavior without significantly changed the compressive strength [13]. As example, several authors [15,16,90] have tested the properties of hempcrete blocks (bricks made by lime and hemp concrete) showing how promising this composite can be for the construction industry. Abdullah and Lee [17], in their comparison between cement-fiber bricks utilizing rice husk, corncob, and coconut coir, reported how feasible is this concept of composite bricks for sustainable infrastructures. Kundu et al. [14] demonstrated that the use of jute fiber as reinforcement in concrete paving blocks not only enhanced the mechanical properties but also extended its service life, minimizing the maintenance cost as well.

Following the non-structural application, Lima et al. [91] evaluated short sisal fiber reinforcing concrete (SSFRC) block for one-way precast concrete slabs. Its behavior under flexural test presented a typical flexural hardening response characterized by five phases: 1) linear-elastic, multiple cracking formation, 2) widening of the existing cracks, 3) redistribution of moments and forces, 4) increase of load carrying capacity, and 5) structural softening. Compared to the commercial blocks (ceramic and EPS), the SSFRC presented more than twice of their resistance and non-brittle failure mode, reaching a load capacity 157 % higher than the minimum load required by the standard for the blocks for this type of slabs.

Although cementitious composites reinforced with natural fibers have already been extensively explored, mainly at the material level, and many authors have proposed its use in the construction industry, the literature about their structural applications is still not enough compared to other synthetic fiber-composites.

3. Degradation Mechanisms of Curaua, Hemp, and Sisal Fibers Exposed to Elevated Temperatures

The influence of elevated temperatures on mechanical behavior was studied for curaua, hemp, and sisal natural fibers. Tensile tests were performed on fibers heated at 100 °C, 150 °C, and 200 °C for 24 h, and reference samples were maintained without thermal treatment for comparisons. The cross-sectional area of the fibers was measured using a scanning electron microscope (SEM), and the image analysis was performed using the open source software Fiji/ImageJ. These data allowed the computation of the tensile stresses and the correlation of the fiber morphology with its macro-mechanical behavior. The thermal degradation behavior of the natural fibers was measured via thermo-gravimetric analysis (TGA) and X-ray diffraction (XRD). The morphological and mechanical characteristics were described and discussed on a microstructural basis. The results showed that the loss of moisture leads to a significant increase in tensile strength before reaching the limits of the degradation range.

Article published: January 8, 2019 – *BioResources*

3.1. Introduction

Research on the addition of natural fibers to engineering materials has been widespread, seeking environmentally friendly and energy-efficient solutions. Natural fibers are particularly interesting reinforcing components for composites, as they are biodegradable, harmless to the environment, and economically more viable than synthetic fibers. Therefore, the mechanical, morphological, and durability characteristics of fibers such as abaca leaf, cotton, curaua, flax, hemp, jute, sisal, *etc*., have been investigated [8,19,23].

Because these fibers are natural materials, they present morphological variety, which directly influences the tensile strength and Young's modulus. Disparities among measured values may be associated with the production efficiency, natural conditions, extraction methods, and processing conditions of the

fiber. These variations in the mechanical behavior can be described by morphological characteristics.

The morphologies of curaua and sisal fibers have been evaluated, correlating their mechanical properties *via* image analysis [3]. These fibers presented tensile strengths greater than 249 MPa and Young's moduli greater than 19 GPa, classifying them as high-performance fibers. The highest tensile strength was observed for curaua, at 543 MPa with a Young's modulus around 64 GPa, followed by sisal, at 484 MPa and 19 GPa, respectively. The correlation of morphology (by the real cross-section) with the mechanical properties showed that as the internal area of the lumens decreases and the secondary cell wall thickness increases, the fiber strength and Young's modulus increase.

Analysis of the influence of stem sampling area on the mechanical properties of hemp fibers showed that fibers from the middle of the stem exhibit the greatest ultimate strength and elongation, with the Young's modulus around 19 GPa and the tensile strength not exceeding 500 MPa [92]. Compared to bottom and top sampling areas, the ultimate tensile strength differences were approximately 23% and 18%, respectively. Liu *et al*. [93] showed that hemp fibers from the middle section also exhibited the best mechanical performance, presenting the highest ultimate tensile strength and strain of 842 MPa and 5.7%, respectively, and a moderate stiffness of 28.8 GPa. Fibers from the top section showed moderate mechanical properties, with an ultimate tensile strength of 809 MPa, a strain of 4.7%, and the highest stiffness, of 31.5 GPa. The variation in mechanical properties of fibers with stem section is explained by the differences in morphological features and composition.

In natural fibers, thermal degradation involves two main steps. The first is the thermal depolymerization of the hemicellulose and the cleavage of glycosidic linkages of cellulose. The second is related to the decomposition of the α-cellulose. The decomposition of lignin occurs at temperatures between 200 °C and 500 °C [36]. In derivative thermogravimetric (DTG) analysis of sisal fibers, the decomposition starts at 215 °C, the decomposition of the hemicellulose happens at 290 °C, and the maximum degradation rate occurs during α-cellulose decomposition at 340 °C. Yao *et al.* [34] analyzed the thermal decomposition process of 10 types of natural fibers, included wood, bamboo, agricultural residue and bast fibers. The thermal decomposition process resulted in a similar TG and

DTG curves due to being lignin cellulosic material. It was noticed an onset decomposition temperature about 215 °C for most of the natural fibers and weight loss in this range was observed around 5%. The maximum decomposition rate of main natural fibers happened about 290 °C, except for maple and pine (an average of 310 °C). These same ranges of decomposition were also presented by other authors [94–97].

The thermal characterization of sisal fibers by thermogravimetric analysis (TGA) presented a mass loss of approximately 3% from 30 °C to 220 °C, attributed to water loss in fibers (intramolecular and intermolecular dehydration reactions) [37]. The fibers' degradation begins around 250 °C and continues quickly as temperature increases, having a mass loss of 72% at approximately 420 °C. Due to the slow decomposition of residues, the mass loss from 420 °C to approximately 520 °C is only 5%. After 520 °C, the ash content is around 20%.

The thermo-mechanical behavior of hemp fibers at temperatures between 20 °C and 200 °C showed an activation of their visco-elastic properties, corresponding to relaxation of the constituent polymers (hemicellulose and lignin), and decreases in rigidity and endurance, attributed to thermal degradation of the cellular walls, at temperatures between 150 °C and 180 °C [98]. The literature presents extensive results about the thermal degradation of cellulose-based structures, especially through thermo-gravimetrical analysis, showing indices of moisture loss, decomposition and maximum weight loss until reaching the limits of the degradation range. However, such analyzes do not represent how these levels of thermal degradation can truly influence the mechanical behavior of exposed natural fibers. The present work investigated the mechanics of three different natural fibers (sisal, curaua, and hemp) and how elevated temperatures can influence their mechanical behavior. The morphologies and cross-sectional areas of each fiber were measured using a scanning electron microscope (SEM) and an image analysis routine. The different fibers were tested under direct tension before and after being exposed at 100 °C, 150 °C, and 200 °C. The mechanisms of degradation were explained through TGA and X-ray diffraction (XRD) analyses and by microstructural observation.

3.2. Experimental

3.2.1. Natural Fibers

The curaua fibers were provided by the Pematec Company (Santarém, Pará, Brazil). The fibers were obtained in the Amazon region, extracted from the *Ananas erectifolius* plant by the mechanical process of decortication [3,6]. The hemp fibers were obtained from Unipak A/S (Galten, Denmark), which manufactures skeins made of natural hemp for the plumbing industry. The sisal fibers were obtained from farms located in Valente, Bahia, Brazil. They were extracted from the leaf of the *Agave sisalana* plant by the same process used for the curaua fiber.

All the fibers were first treated with hot water (approximately 70 °C) for 1 h. This procedure aimed to eliminate the maximum amount of impurities retained on the fiber surface. Thereafter, the fibers were air dried for 48 h.

3.2.2. Mechanical Tests

For the tensile tests, the dried specimens were arranged according to ASTM C1557-14 [99] with gauge lengths corresponding to 20 mm. The fibers were fixed in kraft paper tabs (140 g/cm²) and then heated at 100 °C, 150 °C, and 200 °C for 24 h. Reference samples were maintained without thermal treatment (room at approximately 22 °C and 60% relative humidity) for comparison. The specimens were subjected to tensile loading performed in a servo hydraulic MTS 810 system with a 100 N load cell and an external LVDT (MTS, Eden Prairie, MN, USA) to achieve greater accuracy in data acquisition. Fifteen specimens of fiber were tested for each group (reference, 100 °C, 150 °C, and 200 °C) and the tensile tests were carried on under displacement control at a rate of 0.1 mm/min. All tests were performed at room temperature (approximately 22 °C) with a relative humidity of approximately 60%.

3.2.3. Microstructural Investigation

The fiber microstructure was investigated using a FEI Quanta 400 scanning electron microscope (Thermo Fisher Scientific, Hillsboro, OR, USA). For the dimensional analysis, the samples were prepared by cold embedding in epoxy resin [100]. A solid resin block 30 mm in diameter and approximately 12 mm in height

was drilled with a 1.5 mm diameter drill to create 15 holes, in which 10 mm length fiber samples were carefully placed, as illustrated in **Fig. 3-1a**. Thereafter, the holes with fibers were filled with more epoxy resin, and a vacuum pump was used to ensure no bubbles were formed during its curing. After curing, the block was ground and polished in an automatic polishing machine (Struers Tegramin 20, Cleveland, OH, USA). The grinding was performed with 125 µm, 40 µm, 9 µm, and 6 µm sized diamond-particle-impregnated metal discs, for 3 min, 4 min, 4 min, and 10 min, respectively. Then, the blocks were polished using 3 µm and 1 µm diamond suspensions for approximately 20 min each to produce a high flatness surface. Subsequently, the blocks were covered with evaporated carbon to become conductive, as shown in **Fig. 3-1b**. This preparation procedure can provide a suitable contrast in SEM images to analyze the fiber microstructure. The image analysis was carried out using the open source software Fiji/ImageJ [101,102]. A contour line was interactively drawn to delineate fiber cross-sections, and their areas were then measured.

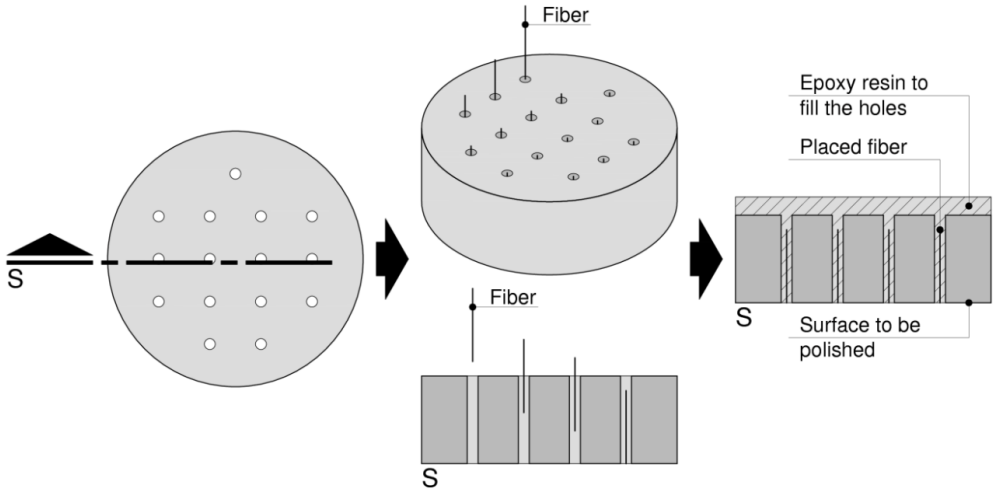

(a)

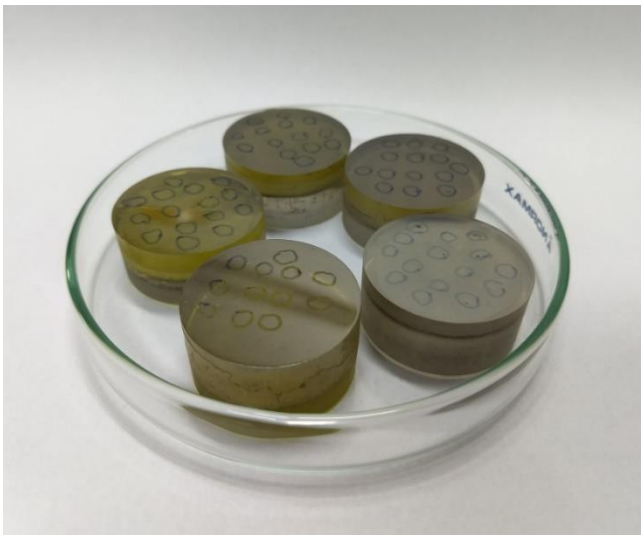

(b)

Figure 3-1. The sample preparation procedure: (a) schematic illustration of the block where fiber samples were placed and embedded within epoxy resin and (b) the blocks covered with evaporated carbon, to become conductive and provide suitable contrast in SEM.

3.2.4. TG and XRD Analyses

The thermogravimetric analysis (TGA) was performed under N_2 atmosphere, from 25 °C up to 500 °C, using a TA Instruments (New Castle, DE, USA) SDT Q600. Approximately 10 mg of each sample was used, and the analysis was conducted at a heating rate of 5 °C/min.

The XRD measurements were performed on a Bruker D8 set to 40 kV and 25 mA using CuKα radiation (λ = 1.5406 nm). The profiles were recorded in an angular range 2θ from 5° up to 100° with increments of 0.01°. For sample preparation, the fibers were scissor cut to particle sizes of less than 0.5 mm. Four samples by fiber type were analyzed for each group (reference, 100 °C, 150 °C and 200 °C). To determine the amount of crystallinity, the deconvolution method of crystalline peaks and amorphous halo was used. For this process, OriginPro8 software (OriginLab Corp., Northampton, USA) with a Gaussian function was used. The diffractogram was separated into various components that independently contributed to the formation of the peaks in each phase. The quantitative decomposition of XRD provided a measure of crystallinity index using **Eq. 3-1**, where CI is the crystallinity index of the material, Ac is the area of crystalline peaks, and Aa is the area of amorphous halo.

$$\mathrm{CI}\ (\%) = {}^{\mathrm{Ac}}/_{\mathrm{Ac}+\mathrm{Aa}} \times 100 \qquad \textbf{(Eq. 3-1)}$$

In order to evaluate the statistical significance of CI variations, the two-sample t-test was used as the statistical method. The parameter $\alpha = 0.05$ was set as the risk level in all statistical analysis, and $p < 0.05$ was considered to be statistically significant.

3.3. Results and Discussion

3.3.1. Fiber Morphology

Hierarchically, in a simplified way, a single natural fiber is formed by several microfibers that have their cell walls (primary cell wall and secondary wall divided into three layers around the lumen) constituted by a series of helically wound cellular microfibrils formed from cellulose molecules [25,41,103]. The studied fibers showed different morphologies when analyzed by dimensional parameters. The geometries of the cross sections were also distinct, and these variations were related to the quantity, size, and organization of the microfibers. **Table 3-1** summarizes the morphological characteristics of the curaua, hemp, and sisal fibers.

Table 3-1. Morphological Characteristics of Curaua, Hemp, and Sisal Fibers.

Fiber	Fiber Cross Section Area (mm²)	Amount of Microfibers per Cross Section	Microfiber Cross Section Area (μm²)	Cell Wall Thickness (μm)
Curaua	0.006 ± 0.001	404 ± 117	17.86 ± 9.86	1.58 ± 0.45
Hemp	0.002 ± 0.001	11 ± 4	224.55 ± 186.24	6.21 ± 2.98
Sisal	0.030 ± 0.010	228 ± 38	137.57 ± 50.42	2.95 ± 0.71

The cross section of the curaua fiber (**Fig. 3-2a**) presented a star shape with area around 0.006 mm² and a large amount of microfibers in its structure, approximately 404 per section, the greatest amount of microfibers among the three species studied. These microfibers presented an average area of 18 μm² and cell wall thickness of 1.6 μm, the smallest area and cell wall thickness of microfibers among the three species studied. The hemp fiber (**Fig. 3-2b**) showed the smallest area among the three fibers, measuring 0.002 mm², and could not conclusively be associated with a specific form due to their average amount of microfibers per

section being around 11, which together showed a relatively uniform geometry of agglomeration. However, their microfibers presented an area around 224 μm² with the cell wall thickness around 6.2 μm, the largest among the three fibers studied. The sisal fiber showed the largest cross section area, compared with curaua and hemp, measuring 0.030 mm². The sisal fiber (**Fig. 3-2c**) presented an arched shape [5], with approximately 228 microfibers, measuring about 137μm² in area with a cell wall thickness around 2.9 μm.

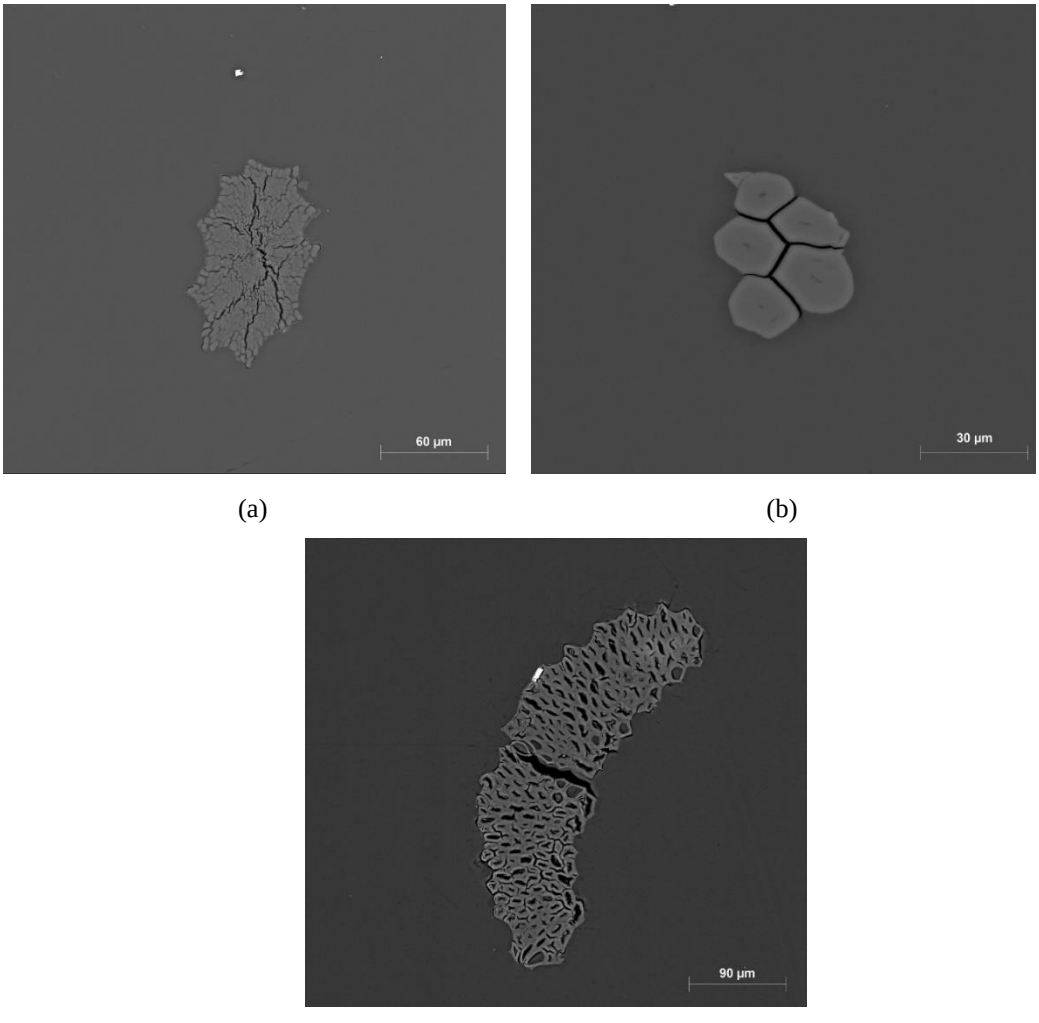

(a) (b)

(c)

Figure 3-2. Cross sections of curaua (a), hemp (b), and sisal (c) fibers by SEM.

Fidelis *et al.* [3] also investigated the morphological characteristics of curaua and sisal fibers, as showed in **Table 3-2**. Some of these results, such as the amount of microfibers per cross section, presented a wide variation: a reduction of 97% and 39% for curaua and sisal, respectively. However, even with this large rate

difference, the cross-sectional area results can be considered close. These variations can be explained by the morphological disuniformity presented by the natural fibers structure, which provides different characteristics, including the mechanical ones, due the influence of the morphology variation of fibers from stem's top, middle and bottom [92,93].

Table 3-2. Natural Fibers Morphological Characteristics from Literature

Fiber	FiberCross Section Area (mm²)	Amount of Microfibers per Cross Section	Cell Wall Thickness (µm)	Authors
Curaua	0.004	12	3.5	Fidelis *et al.* (2013)
Sisal	0.023	144	2.6	

When exposed to thermal treatments, the fibers showed different levels of degradation. The curaua and hemp fibers (**Fig. 3-3 and Fig. 3-4**) exposed at 200 °C presented delamination of the microfibers, with the weakening of the middle lamellas visible, especially in the hemp fibers that suffered total bond collapse.

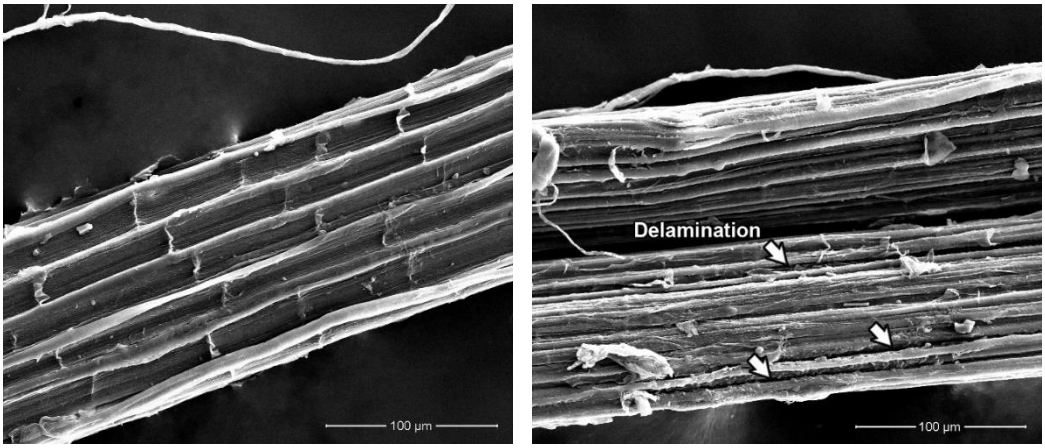

(a) (b)

Figure 3-3. The curaua reference (a) and treated at 200 °C (b).

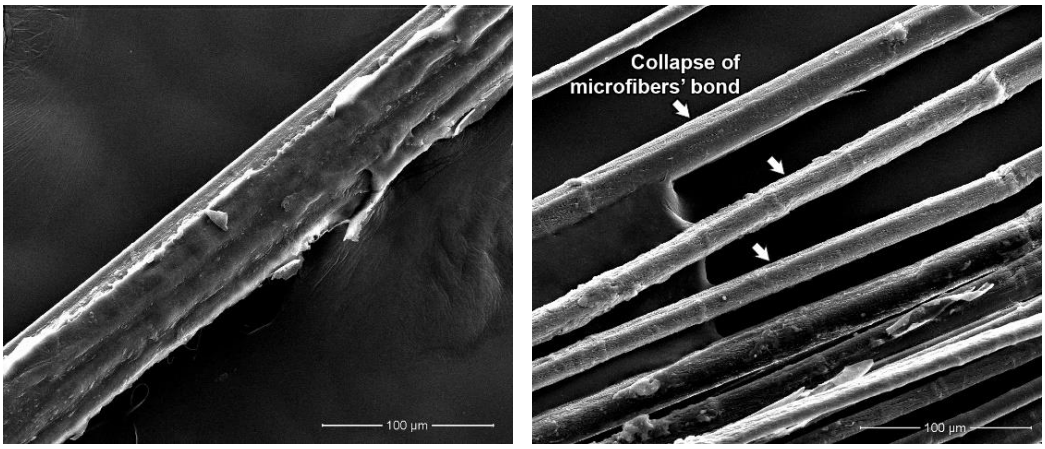

(a) (b)

Figure 3-4. The hemp reference (a) and treated at 200 °C (b).

The sisal fibers (**Fig. 3-5**) at 200 °C showed the greatest thermal resistance and did not show any signs of weakening. The high thermal resistance of sisal in comparison to curaua and hemp can be explained by the amount of hemicelluloses — curaua and hemp have hemicellulose amounts around 20% to 23% [8,19,27] but sisal only 10% [6,30] — which is responsible for most of the thermal degradation behavior of natural fibers [104,105].

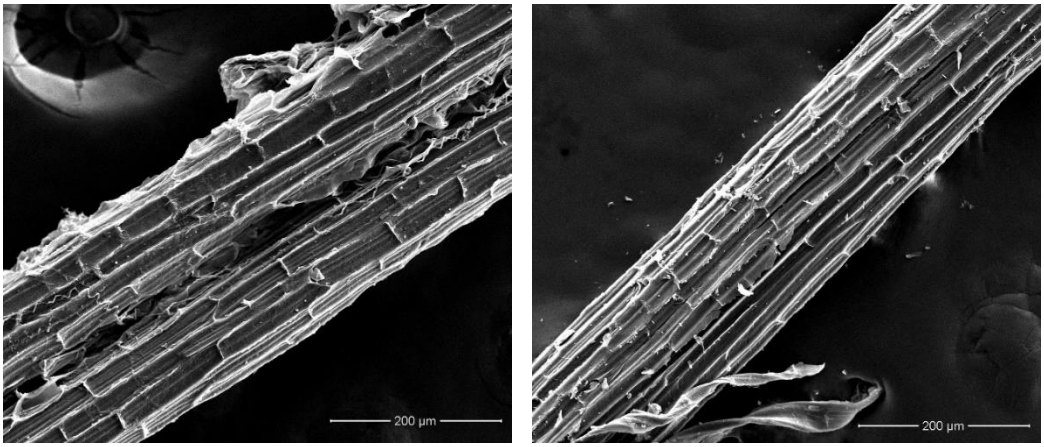

(a) (b)

Figure 3-5. The sisal reference (a) and treated at 200 °C (b).

3.3.2. TG and XRD Analysis

The TGA of curaua, hemp, and sisal fibers showed similar patterns of weight loss (**Fig. 3-6**). Up to 100 °C, the samples showed a moisture decrease, represented by a weight loss of approximately 9%, and then stabilized from that

point to 200 °C. From there to approximately 290 °C the hemicellulose degradation occurred and thereafter the thermal decomposition of cellulose remains up to approximately 350 °C, as also presented by many other authors [35–38]. At this point, the thermal degradation caused weight losses of 78%, 67%, and 72% for curaua, hemp, and sisal, respectively.

According with DTG analyses, the maximum weight loss was observed at 329 °C for hemp, 336 °C for curaua, and 342 °C for sisal, which is consistent with that observed in the XRD analysis where sisal fibers also showed higher thermal stability, probably due the lower content of hemicelluloses when compared to curaua and hemp fibers. The range from 100 °C to 200 °C by TGA and DTG showed no significant changes occurring with these fibers (beyond those already shown up to 100 °C).

The XRD analysis of curaua, hemp, and sisal fibers was performed for the reference and 200 °C treated samples, and the deconvolution of crystalline peaks and amorphous halo was performed in the range of 5° to 60° (2θ). The highest intensity peak in all cases was noticed at 2θ between 22.0° and 22.6° reflection assigned to the (002) crystallographic plane. The average intensity peak was observed at 2θ between 14.5° and 15.3° (101), with the lowest intensity peak at 2θ between 33.9° and 34.1° (040).

Only the hemp samples presented prominent peaks at 2θ between 15.9° and 16.2° ($10\bar{1}$). These results are compatible with other analyses about the crystalline structure of cellulose [2,107–109].

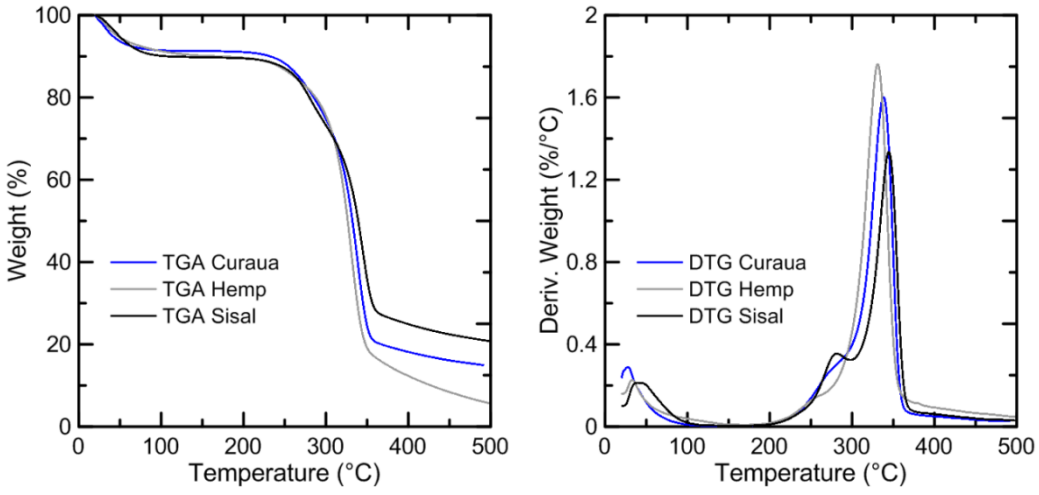

(a) (b)

Figure 3-6. TGA and DTG of curaua, hemp, and sisal fibers.

The peaks at 2θ from 33.9° to 34.1° (040) were not included in the deconvolution analysis due to their very low intensity [109] (**Fig. 3-7**). **Table 3-3** presents the natural fibers' crystallinity indexes.

Table 3-3. Crystallinity Indexes of Curaua, Hemp, and Sisal Fibers, Reference and after Exposure at 200 °C.

Treatment	Crystallinity Index (%)		
	Curaua	Hemp	Sisal
Reference	57.4 ± 1.4	59.2 ± 0.9	54.7 ± 2.0
200 °C	59.0 ± 1.4	61.4 ± 1.1	56.7 ± 1.2

Comparing the reference fibers with those exposed at 200 °C, the CI presented increases of about 3%, 4%, and 4% for curaua, hemp, and sisal, respectively. The crystallinity degree of cellulose is directly related to the rigidity and flexibility of the natural fibers: their rigidity increases, and flexibility decreases, with increasing ratio of crystalline to amorphous regions [108]. In this case, however, the CI increases at 200 °C probably were associated with the loss of humidity (at 100 °C). For curaua and sisal fibers, this difference in crystallinity index values between the reference and 200 °C samples were not statistically significant, as described by the *p*-values in **Table 3-4**. However, the hemp fibers presented $p < 0.05$, which indicates there was statistical significance concerning its variation.

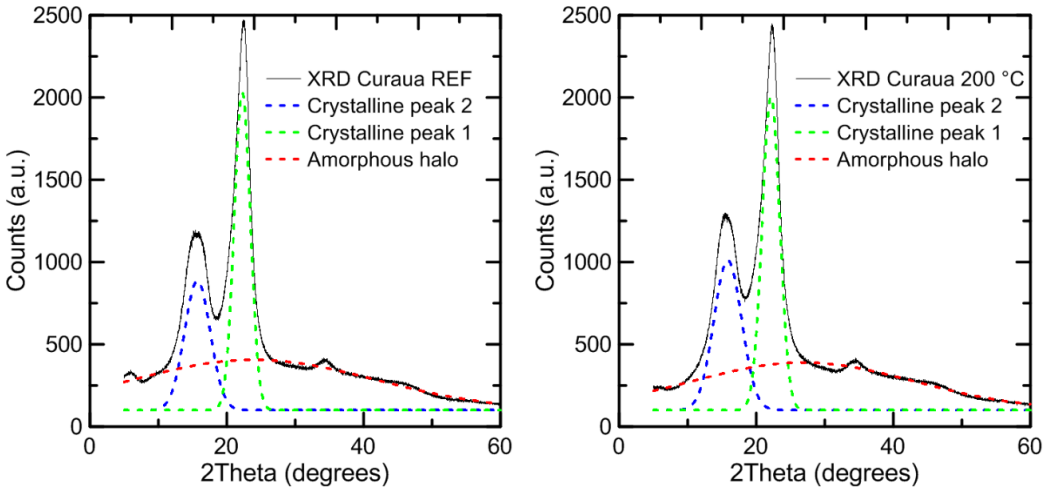

(a) (b)

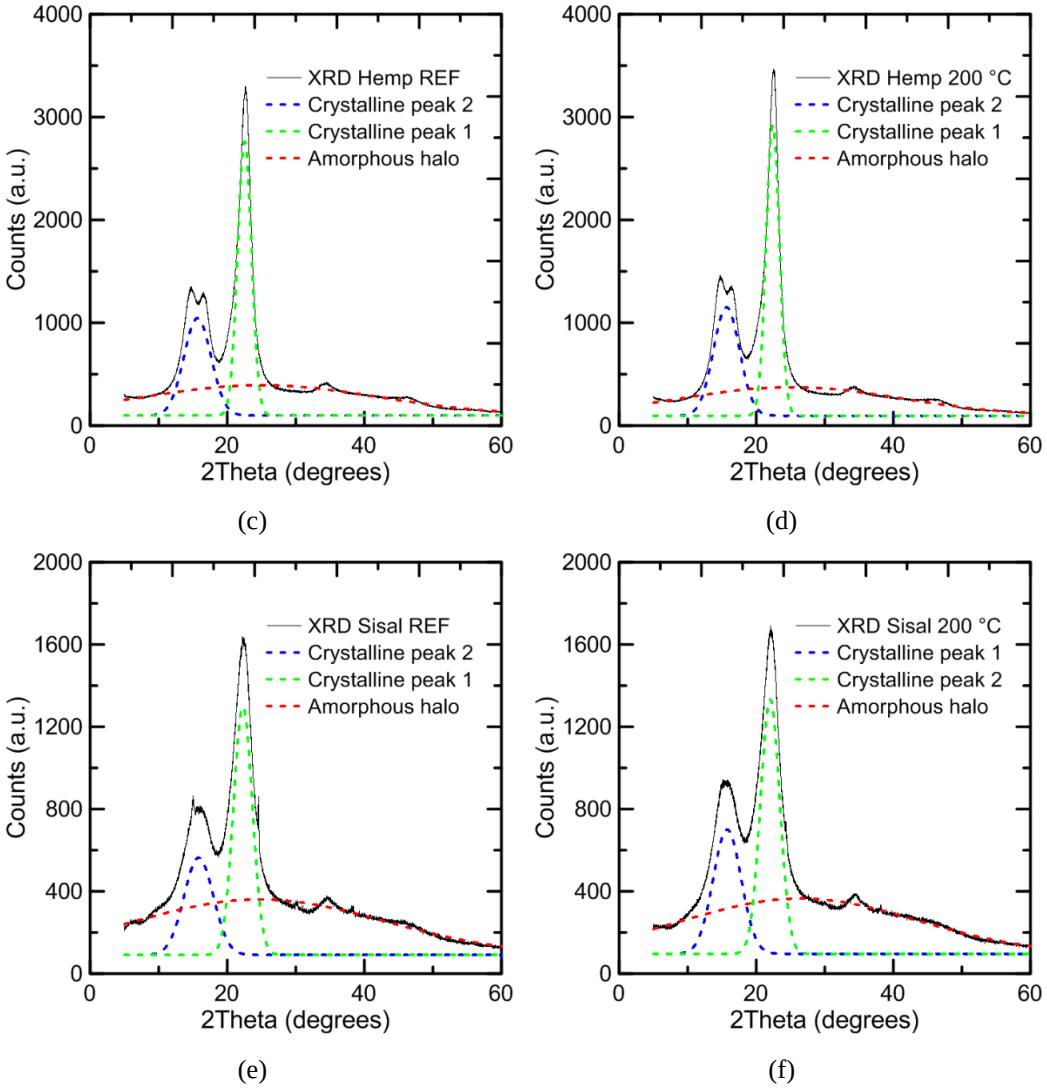

Figure 3-7. The XRD and software analysis to determinate the CI of curaua reference (a), curaua exposed to 200 °C (b), hemp reference (c), hemp exposed to 200 °C (d), sisal reference (e), and sisal exposed to 200 °C (f) (a.u. stands for arbitrary units).

Table 3-4. Statistical Significance of Crystallinity Index Values Between the Reference and 200 °C Samples by Two-Sample T-Test.

Samples	***t* (*df* = 6)**	***p*-value (two-tail)**
Curaua	-1.420	0.200
Hemp	-2.590	0.041
Sisal	-1.534	0.176

In this regard, other authors [106,110] reported a decrease about 10 % in CI of bleached natural fibers and affirmed that these variations does not affect significantly the biopolymer properties, however, these kinds of chemical results must be confronted with experimental mechanical analyzes.

3.3.3. Fiber Mechanical Behavior

The mechanical behaviors of all the fibers under all conditions are summarized in **Table 3-5**. The highest tensile strength among reference samples was observed for curaua (760 MPa), followed by the hemp (480 MPa) and sisal (357 MPa).

Table 3-5. Tensile Tests Results for Curaua, Hemp, and Sisal Fibers

Fiber	Treatment	Tensile Strength (MPa)	Young's Modulus (GPa)	Strain-to-Failure (%)
Curaua	Reference	760.02 ± 217.33	32.19 ± 8.08	2.4 ± 0.3
	100 °C	1480.40 ± 215.82	43.24 ± 6.88	3.3 ± 0.6
	150 °C	646.22 ± 168.04	35.41 ± 14.28	3.1 ± 1.1
	200 °C	51.75 ± 7.51	17.84 ± 9.94	0.4 ± 0.2
Hemp	Reference	480.25 ± 255.31	51.58 ± 18.50	1.0 ± 0.3
	100 °C	567.70 ± 237.98	39.20 ± 12.06	1.6 ± 0.4
	150 °C	510.63 ± 141.65	44.99 ± 14.11	1.4 ± 0.3
	200 °C	-	-	-
Sisal	Reference	357.16 ± 35.74	8.74 ± 3.32	14.7 ± 7.8
	100 °C	379.46 ± 96.79	11.38 ± 5.47	9.3 ± 7.0
	150 °C	306.51 ± 91.72	11.39 ± 4.16	3.3 ± 0.7
	200 °C	38.11 ± 6.97	7.06 ± 2.16	0.6 ± 0.2

The curaua and hemp fibers presented similar mechanical behaviors, both showing a high stiffness, while sisal tended to be more ductile, as shown in **Fig. 3-8a**. This is probably related to their microfibrillar angle (hemp approximately 6° and sisal between 10° and 22°) [8,19,31], where smaller angles lead to greater strength and stiffness and larger angles yield greater ductility [18]. In sisal fibers, a non-linear region at the initial portion of the curve can be explained as a collapse of the weak primary cell walls and delamination between microfibers [6].

Fig. 3-8b presents the relation between tensile strength and temperature from references up to 150 °C treated samples. In comparison with the reference samples, all studied fibers presented tensile strength gains when subjected to 100 °C for 24 h (**Fig. 3-8b**). The curaua, hemp, and sisal fibers at 100 °C showed tensile strength gains of approximately 94%, 18%, and 6%, respectively. This result shows that temperatures around 100 °C do not compromise the tensile behavior of natural fibers but can admit mechanical gains by the loss of humidity.

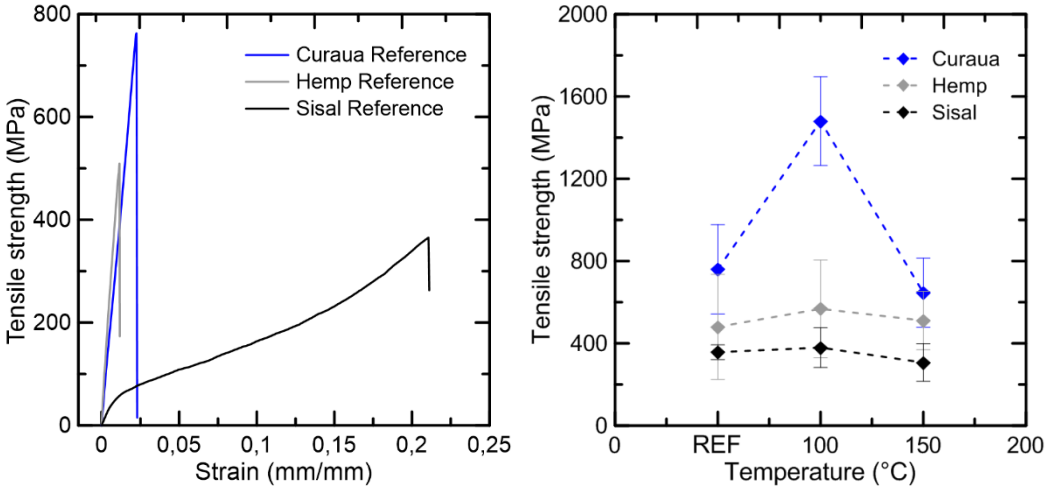

(a) (b)

Figure 3-8. Mechanical behavior of reference curaua, hemp, and sisal fibers (a) and the relation between tensile strength and temperature from references up to 150 °C treated samples (b).

Fig. 3-9 compares the fibers' tensile behaviors when thermally treated. At 100 °C, the curaua and sisal fibers presented Young's modulus increases of approximately 34% and 30%, respectively. Those fibers also presented increases in stiffness, while the hemp fibers exhibited a decrease of about 24% after being exposed at 100 °C. These variations in stiffness can be attributed to rearrangements and reorientations of the cellulose microfibrils and/or changes in the crystallinity fraction that may occur in the fibers [98].

At 150 °C, all fibers started showing losses in tensile strength. The curaua and sisal fibers showed values below their respective reference samples. The loss showed by the hemp fibers at 150 °C was not sufficient to place it below the reference samples, but at 200 °C these were the most damaged, presenting no mechanical resistance and easily breaking if handled, which agrees with the results of the statistical significance.

At 200 °C, curaua and sisal fibers had drastic decreases in tensile strength, around 51 MPa and 38 MPa, respectively (**Fig. 3-9d**). The thermal treatment at 200 °C completely damaged the fibers, which is attributable to the thermal degradation of the cellular walls at temperatures between 150 °C and 180 °C [98]. The same occurred with thermal treatments on kenaf bast fibers at 170 °C and 180 °C for 24 h in other experiments [111].

For the sisal fibers (**Fig. 3-9c**), the non-linear region occurring after 50 MPa

gradually disappeared as the temperature increased. The changes at the initial non-linear region may be associated with the loss of humidity in those thermal ranges, which can increase the stiffness of the fiber and, in this case, probably opposes the effect of the previously described delamination of the microfibers [6].

Comparing the mechanical results with the TG and XRD analyses, weight loss and CI can be described as stable in the range from 100 °C to 200 °C, but the mechanical degradation is notable. In the range between 100 °C and 150 °C, partial decreases in tensile behavior occur. From there to 200 °C, the fibers are already mechanically compromised.

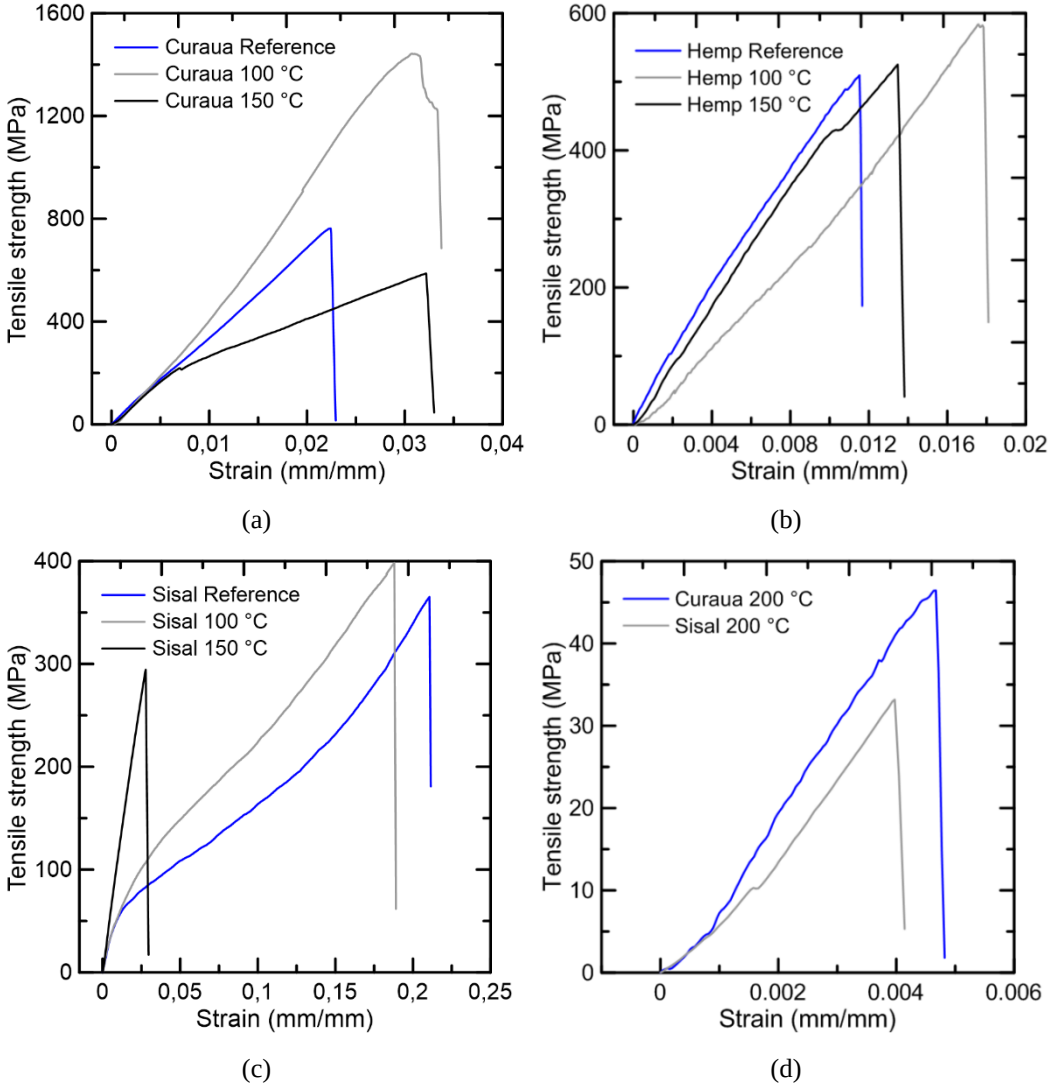

Figure 3-9. Comparison of curaua (a), hemp (b), and sisal (c) fibers' tensile behaviors when thermally treated; the curaua and sisal fibers at 200 °C (d).

3.4. Conclusions

Although similar at first, the curaua, hemp, and sisal fibers showed distinct morphologies. Characteristics such as cross section area and amount of microfibers per section evinced dimensional variability in microstructure, which influences mechanical behavior.

When exposed at 100 °C for 24 h, all fibers presented tensile strength improvements, especially the curaua fibers, which showed an increase of approximately 94%, followed by hemp and sisal, with increases of approximately 18% and 6%, respectively.

The curaua and sisal fibers also showed Young's modulus increases at 100 °C, presenting stiffness increases, while the hemp fibers exhibited a decrease in Young's modulus.

The behavior of all studied fibers presented on TG and XRD analysis for the range from 100 °C to 200 °C is described as stable, but their mechanical behavior showed severe degradation within the range from 150 °C to 200 °C. In this case the mechanical degradation can be traced back to the loss of bond among the several microfibers that compose the fibers.

All fibers exposed at 200 °C for 24 h became fragile and brittle, presenting drastic decreases in mechanical resistance. The curaua and hemp fibers showed clear microfiber delamination, especially the hemp, which suffered total bond collapse. The sisal fibers showed the greatest thermal resistance and did not show signs of weakening. Nevertheless, the sisal fiber mechanical bearing capacity was also compromised after 200 °C.

The overall analysis of elevated temperatures on the mechanical behavior of natural fibers showed that, in three cases with three distinct species (curaua, hemp, and sisal), heating up to 100 °C did not compromise their tensile behavior but could admit mechanical gains by the loss of moisture content.

4. On the Use of Natural Curauá Reinforced Cement Based Composites for Structural Applications

The construction industry demand for environmentally friendly and energy-efficient solutions has driven researchers to matching non-traditional materials, as natural resources, with modern building technologies. The present work investigated the mechanical behavior and cracking mechanisms of a cementitious composite reinforced with natural curauá unidirectional fabric towards its use as reinforcement for a structural concrete element. The experimental program included direct tension, bending, cyclic and combined loading compression tests in cement-based composites reinforced with curauá natural fabrics. Different specimen scales were tested under direct tensile loading in order to study the cracking mechanisms and strain sensitivity to size effect. A structural beam externally reinforced with this newly developed composite was tested under bending and an analytical model was proposed to corroborate the experimental tests. The proposed model gave very accurate prediction of the moment-curvature. The composite used as a structural reinforcement behaved efficiently, resulting in rebar yielding delay, providing to the beam a higher deflection capacity and a flexural strength gain of about 16 %.

Article published: August 11, 2020 – *Cement and Concrete Composites*

4.1. Introduction

Aiming to reduce the CO_2 emissions, many authors have been investigating alternatives to reduce the cement consumption, as partially replacing it by pozzolans such as blast-furnace slag, fly ash, metakaolin, rice husk, silica fume, and more [112–115]. The combination of low CO_2 emission cements with the use of natural fibers as reinforcement can result in an ultimate green composite system. The physical and morphological properties of natural fibers [3,8,19,23,97,106,116] and its durability in an alkaline environment [43,84,117] have been deeply studied. The cited works focus on the use of natural fibers as cementitious matrix-

reinforcement, providing strength enhancement, strain capacity, and work-to-fracture by the multiple cracking mechanisms, leading to a strain hardening behavior. Mechanical tests on cementitious composites reinforced with natural fibers are already deeply explored in many configurations: such as the textile form [20,68,69], in a continuous and aligned way [7,21,70], or short and randomly dispersed in the matrix [9,22,71].

In addition, the incorporation of natural fibers can mitigate the tensile stresses generated during plastic shrinkage [118]. This improved plastic shrinkage resistance is related to the higher elastic modulus of fibers compared to the cement matrix at early age and crack bridge and arrest mechanisms induced by these fibers [118–120]. The natural fibers can also contribute to the self-healing capacity of cementitious matrix acting as a water reservoir, resulting in a better internal curing and improving its autogenous healing [121]. These fibers can improve the bridging of new hydration products across the cracks at a higher damaged degree, which is not possible in normal concretes [121,122]. However, even with all the knowledge developed about cementitious composites reinforced with natural fibers on the mechanics and durability aspects, its use has especially focused on the non-structural elements, such as tiles [11,12], and there is practically no scientific literature about their applications at the structural level.

On the other hand, the use of synthetic fibers reinforced-cement composites is already widely applied in industrial installations, shotcrete, and in precast structures [47–49]. Many authors [123–125] presented results about the use of synthetic fibers reinforced-cement composites as reinforcement and repair for structural concrete elements. Schladitz at al. [126] presented a textile high-performance carbon reinforced-composite as concrete slabs reinforcement and noted that the load-bearing capacity increases uniformly at increasing textile carbon layer numbers. With four layers, the load-bearing capacity of the reinforced concrete slab could be raised to 3.5 times as compared to its unreinforced counterpart. At equal load levels, a decrease in deflections could be observed with increasing layer numbers. Kim and Yun [127] showed that the concrete beams repaired with polyethylene and polyvinyl fibers reinforced-composite demonstrated no crushing or spalling until final failure. It was noted that the composite application can improve moment strength and delay the yielding moment due to the bridging action of the fibers.

The present work investigated the mechanics of natural curauá reinforced cement-based composites and its use as a structural reinforcement material. The continuous fibers were divided into three layers and used as reinforcement in a continuous and aligned way. The mechanical behavior was evaluated by direct tensile, flexural, cyclic and combined loading compression (CLC) tests, where the laminate plate composites under tensile and flexural loads were manufactured in three different sizes for comparison. The crack pattern evolution on tensile tests were analyzed through Digital Image Correlation (DIC). After the material level characterization, the developed cementitious composite was applied as reinforcement for a structural concrete element, which was tested under four-point bending and compared with a non-reinforced reference. Finally, theoretical moment–curvature curves were developed and compared with the experimental results.

4.2. Material and Methods

4.2.1. Curauá Fibers

The Pematec Company (Santarém, Pará, Brazil) provided the curauá fibers as shown in **Fig. 4-1a.** The fibers were obtained in the Amazon region, extracted from the *Ananas erectifolius* plant by the mechanical process of decortication [3,6]. The fibers were first treated with hot water (approximately 70 °C) for 1 h. This procedure aimed to eliminate the maximum amount of impurities retained on the fiber surface [116]. Thereafter, the fibers were air-dried for 48 h and then brushed to be separated into individual filaments (**Fig. 4-1b**).

The leaves of curauá plant, from which the fibers were extracted, can reach up to 150 cm length with an average 4 cm width and 0.5 cm thickness [128]. However, by the mechanical extraction process, the fibers available for this work had an average length that did not exceed 80 cm. Mechanically, a single filament fiber can reach a tensile strength of about 760 MPa, with 32 GPa of elastic modulus, and strain capacity around 2.4 % [116]. The density of curauá fiber is equal to 1.1 g/cm³ as also presented in other works [129,130].

(a) (b)

Figure 4-1. Curaua fibers as received from Pematec Company (a), the same fibers after hot water treatment, air dry and brush (b).

4.2.2. Matrix Design

The mortar matrix for the composite was designed for the ratio of 1:1:0.4 (cementitious material:sand:water) and pozzolans supplementation was adopted aiming a calcium hydroxide free matrix, seeking to provide the natural fibers higher durability as previously reported [4,21,68,122]. The cementitious material was composed, in mass, by 50 % Portland cement type CPV (defined by the Brazilian standard ABNT NBR 16697 [131]), 40% metakaolin (obtained from Metacaulim do Brasil Indústria e Comércio Ltda), and 10% fly ash (from POZOFLY®). The used quartz sand had a maximum diameter of 1.18 mm and a density of about 2.67 g/cm³. The superplasticizer GLENIUM® 3500 used proportion was 0.7 % of the cementitious material mass to provide the necessary workability. The average compressive strength of the mortar matrix after 28 days was 81 MPa based on the axial compressive test results, and the flow table spread 375 mm.

For the structural concrete element, the mix design presented in **Table 4-1** was used. The design was based on the work of Lima et al. [132]. It consisted of Brazilian normalized Portland cement CPII-F32 [131], fine aggregate that passed through a 4.75 mm sieve with a fineness modulus (FM) of 2.74, and two different types of coarse aggregates (presenting 9 mm and 19 mm at maximum diameter). The superplasticizer PLASTOL® 4100 was used to adjust the workability of the

mix. The average compressive strength of the concrete matrix after 28 days was 33 MPa based on the axial compressive test results, and the slump was 75 mm.

Table 4-1. Concrete mix proportions.

Materials	**Kg/m³**
Portland cement (CPII-F32)	336.0
Natural sand	642.0
Coarse aggregate (9 mm)	441.0
Coarse aggregate (19 mm)	782.0
Water	168.0
Superplasticizer	0.5

4.2.3. Manufacturing

Firstly, the curauá fibers were dipped in water during 1 h, enough time to reach levels close to their maximum saturation [1], and then air-dried for 15 min to eliminate the excess humidity retained on their surface. This method aims to minimize the water absorption from the matrix mixture by the porous structure of the fibers and make it better workable during the manufacturing. The matrix was produced using a bench-mounted planetary mixer with a capacity of 20 L. The cementitious material and quartz sand were first mixed with 70 % of water for 1 min for homogenization. Thereafter, the superplasticizer previously diluted in the remaining 30 % of water was slowly poured into the running mixer and then mixed for more 3 min.

The composite laminate plates were produced in three different sizes. While the largest ones measured 1000 mm length and 120 mm width (LP1000), the others measured 500 mm (LP500) and 250 mm (LP250) length, respectively, both with 60 mm width. All specimens presented a thickness of about 10 mm. The total amount of curauá fibers per specimen corresponds to a volume fraction of 5 %, divided into three layers. The fibers were used in a continuous form and arranged in a longitudinally aligned way, as a unidirectional fabric. During manufacturing, the mortar mix was placed in steel molds by a manual layout technique, one layer at a time, followed by one layer of aligned curauá fibers.

For the LP1000 specimens, as the fibers available for this work do not present 1000 mm of length, it was necessary to develop a system of overlapped layer. In this method, each of the three fabric layers was cut into subparts, with an overlap equal to 70 mm, reaching the maximum length of 1000 mm. These overlaps were

organized alternately, aiming to avoid stress concetration that could produce a weaker zone. **Fig. 4-2a** shows the arrangement of L1000 overlapped layer system and **Fig. 4-2b** its manufacturing process. All the composite specimens were cured in the molds for 24 h and then underwater for 28 days.

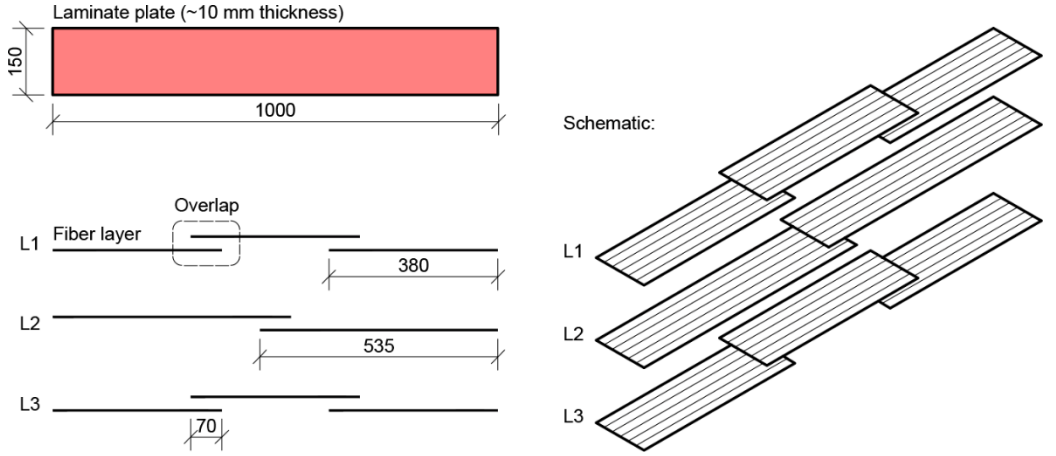

(a)

(b)

Figure 4-2. Arrangement of L1000 fibers overlapped layer system (a) and the manufacturing process (b).

For the Combined Loading Compression (CLC) tests, the specimens were cut out from the laminate plates (using a metallographic cutting machine Arotec Arocor 80) measuring 160 mm of length, 19 mm of width and thickness of about 10 mm. During the cut, the longitudinal extension of CLC samples was made following the continuous arrangement of fibers, so their fiber layers follow the exact same patterns as the tensile, bending and cyclic samples. To avoid undesirable end crushing, the specimens were tabbed with aluminum plates (2 mm of thickness),

glued with an epoxy resin (Sikadur-32), as shown in **Fig. 4-3**. To measure the strains, strain gages were fixed on each face, according to ASTM D6641/D6641M-14 [133], within the adopted 20 mm gage length. For comparison, axial compression specimens with no fibers were manufactured, measuring 100 mm of height and 50 mm of diameter.

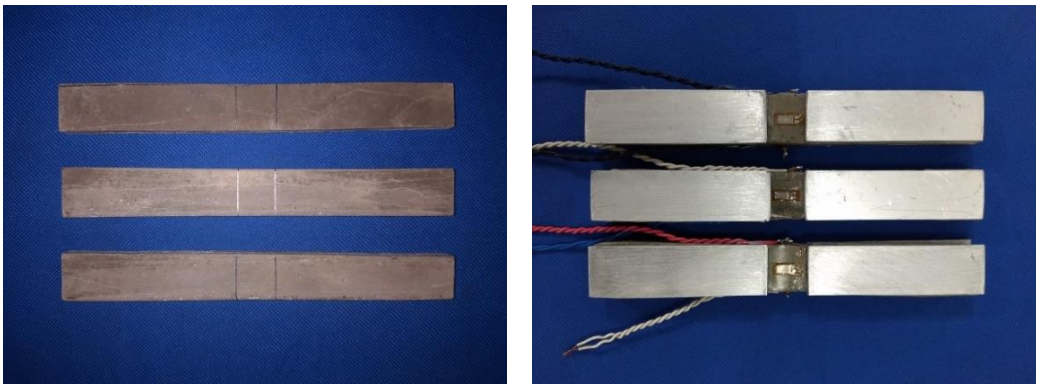

(a) (b)

Figure 4-3. CLC specimens cut out from laminate plates (a) and tabbed with the aluminum plates (b).

The concrete mixture for the structural beams was prepared in a concrete mixer with capacity of 400 L. The dry materials (sand, cement and coarse aggregate) were added and mixed for one minute before 70% of the water addition. Then, the superplasticizer previously diluted in the remaining 30 % of water was added. The mixing process lasted five minutes. The specimens were designed for the flexural tests, measuring 1200 mm length, 120 mm width and 150 mm height. For the conventional reinforcement, steel rebars with nominal yield strength of 500 MPa were used. The beams were designed to be under-reinforced while met the minimum required steel reinforcement. Shear reinforcement stirrups with 125 mm spacing were used to prevent failure due to shear. **Fig. 4-4** presented the schematic beam details and dimensions. At the composite application as structural reinforcement, a laminated plate was manufactured on the underside of the beam and then the 28 days of curing were counted until the tests. For the reinforcement application, the beam bottom surface was just cleaned and slightly moistened, then the same manufacturing process described to LP1000 was done.

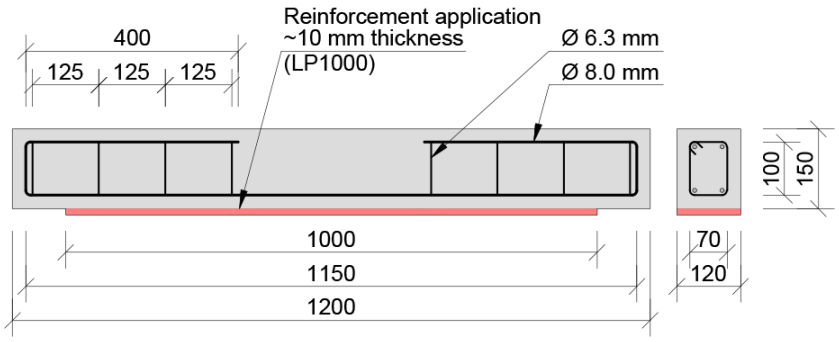

Figure 4-4. Schematic beam details and dimensions.

4.3. Mechanical Tests

4.3.1. Tensile Tests

The curauá unidirectional fabric consisted of bundle of fibers with 500 mm length and 60 mm width. The specimen thickness was defined by the relation of its known measures and volume – mass (4.05 g) and density (1.1 g/cm³). The material was tested under tensile load aiming to comprehend its mechanical properties. The used gauge length corresponded to 200 mm and the tensile loading performed in a servo-hydraulic MTS 811 system with a 1000 kN load cell and two external LVDTs (MTS, Eden Prairie, MN, USA) to achieve greater accuracy in data acquisition. The specimens were fixed in steel plates (**Fig. 4-5a**) with clamped screws controlled by a torque (15 N.m), and the tests were carried on under displacement control at a rate of 0.1 mm/min. Seeking a good fixation and stability of this kind of specimen at the setup test, polymeric block bases (epoxy resin Sikadur-32) were molded in both ends sides of the fiber bundle, as presented in **Fig. 4-5b**.

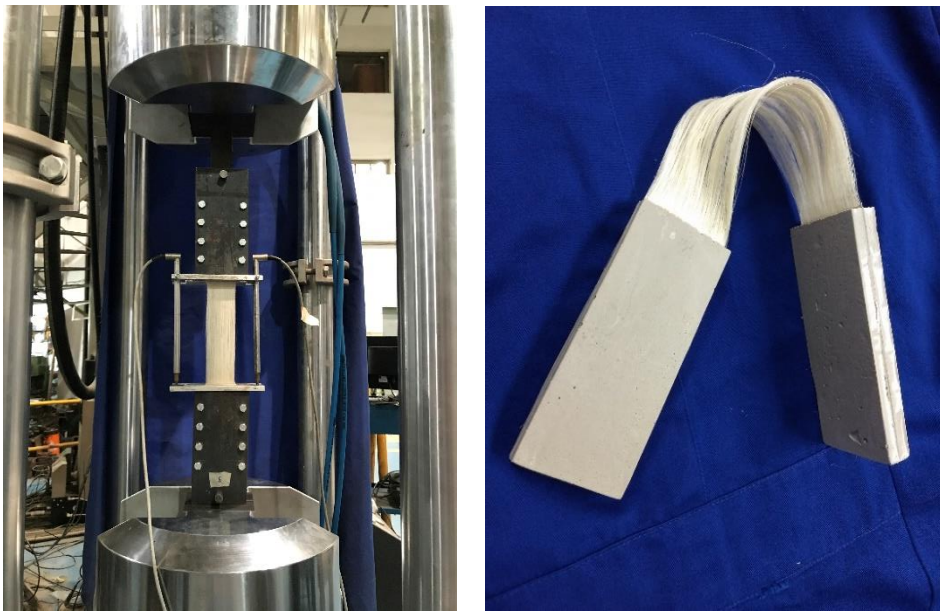

(a) (b)

Figure 4-5. Curauá fabric test configuration: experimental set-up (a) and detail of the fabric specimen (b).

The composite direct tensile tests were arranged with variable gage lengths, depending on the size of each sample. For the LP1000, LP500 and LP250 specimens' groups, the used gage length corresponded to 450 mm, 200 mm and 120 mm (**Fig. 4-6**), respectively. The specimens were subjected to tensile loading performed in a servo-hydraulic MTS 811 system with a 1000 kN load cell and a pair of external LVDTs (MTS, Eden Prairie, MN, USA). Three specimens of laminate plates were tested for the 500 mm and 250 mm groups. Due to the exhaustion of the curauá fibers from this same batch and in order to preserve the standardization of the raw materials (along with the difficulty of carrying out this kind of test), only a single LP1000 sample was performed. The specimens were fixed in steel plates with clamped screws controlled by a torque (8.5 N.m), and the tests were carried on under displacement control at a rate of 0.1 mm/min.

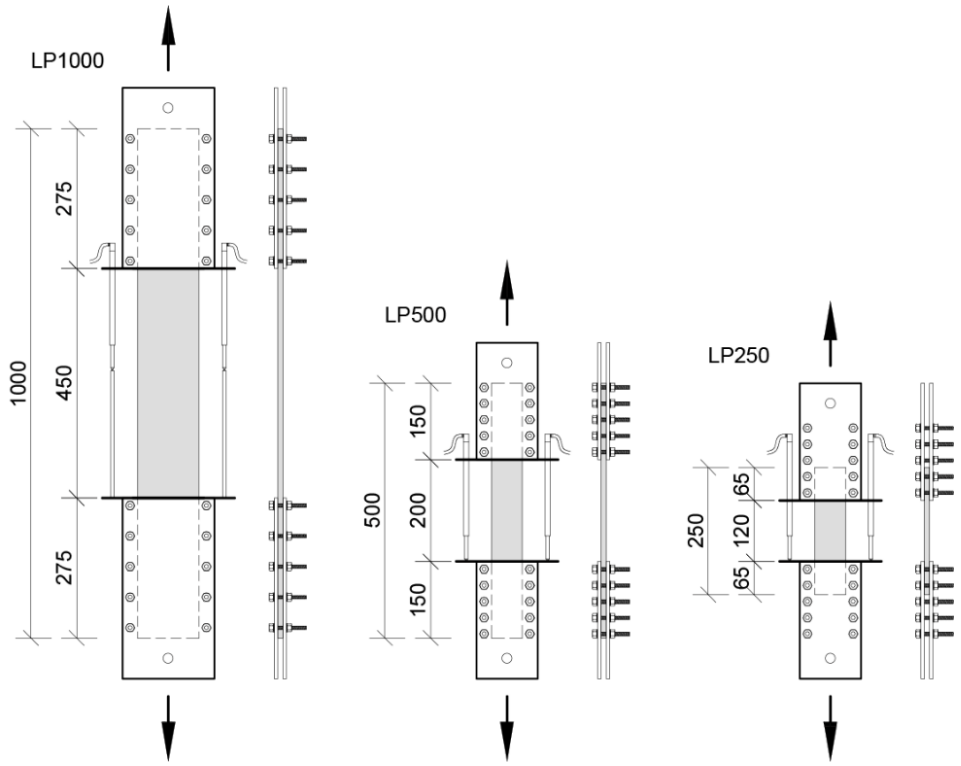

Figure 4-6. The composite direct tensile tests arranged with variable gage lengths.

4.3.2. Bending Tests

The composite four-point bending tests were performed in a servo-hydraulic MTS system with a 100 kN load cell. The vertical displacement was measured by a LVDT to ensure greater accuracy in data acquisition. The tests were carried on under displacement control at a rate of 0.1 mm/min with a 495 mm span between end supports for the LP1000, 270 mm for the LP500 and 220 mm for the LP250. Three specimens of each were performed for this test.

The cyclic bending tests were performed using the same equipment as the monotonic regime, and only the LP250 specimens were tested. These tests followed two steps: a displacement-controlled step, and a load-controlled step as also presented elsewhere [134]. The cyclic flexural testing involved unloading at 0.15, 0.30, 0.50, 1.00, 2.00, 3.00, 4.00, 5.00, 7.50, 10.00, 12.50, 15.00, 17.50, 20.00 and 22.50 mm of deflection displacement, controlled by an external LVDT (MTS, Eden Prairie, MN, USA), as described in **Fig. 4-7**. Three different displacements rates were used during the cycles: 0.15 mm/min from the first to third, 0.30 mm/min from the fourth to eighth and 0.50 mm/min from the ninth to fifteenth. The unloading was controlled by a servo-hydraulic machine and conducted under a constant rate of 0.4 kN/min for every cycle.

As described by Boulekbache *et. al.* [134], the flexural behavior under cyclic loading can be evaluated by two parameters: the degree of reversibility (R) and the cyclic modulus (E_{cyc}). The degree of reversibility is defined as the ratio of the reversible displacement (δ_r) and the total displacement (δ_t) of the loop ($R = \delta_r/\delta_t$). The reversible movement is the distance between the x-axis the major axis of the loop and load discharge arrow at the discharge. The cyclic modulus may be determined by the slope of the line connecting the two points reversing the strain direction. Finally, the initial tangent modulus (E_0) corresponds to the slope at the beginning of load-deflection curve, also shown in **Fig. 4-7**.

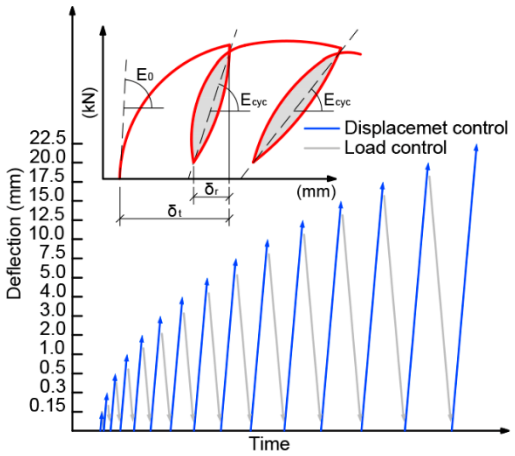

Figure 4-7. Cyclic loading procedure and parameters.

Structural concrete beams were tested in a 500 kN servo-hydraulic MTS actuator mounted in a steel test frame. Strain values were monitored by a total of seven strain gauges: six 10 mm strain gages on steel rebars (three on each rebar) and one 60 mm strain gage applied on concrete in compressed zone, as presented in **Fig. 4-8**. Three LVDTs were used to measure the deflection: one LVDT was placed at the midspan and the other two were located at the load-points alignment. The test was carried on under displacement control at a rate of 1.0 mm/min with an 1100 mm span between end supports.

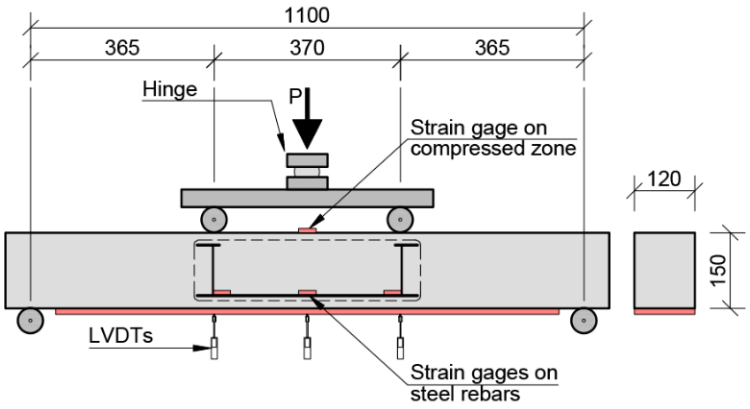

Figure 4-8. Schematic beam banding test details.

4.3.3. Combined Loading Compression (CLC) Tests

These tests were carried on according to the CLC method, adapted from ASTM D6641 [133], under a displacement controlled rate of 1.0 mm/min on a MTS 810 system with load capacity of 500 kN. The used gage length corresponded to 20 mm. The specimens were fixed between steel blocks with clamped screws controlled by a torque (8.5 N.m). All the specimens were instrumented with back-to-back strain gages in order to confirm pure compression. The strains were measured using strain gages positioned on the middle of the specimen's faces. **Fig. 4-9** presents the schematic CLC test setup.

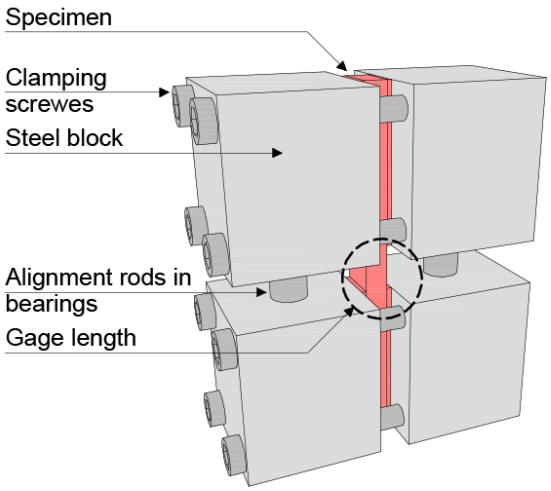

Figure 4-9. The schematic combined loading compression (CLC) setup.

4.3.4. Digital Image Correlation (DIC)

Aiming to better understand the crack evolution process of the composites, Digital Image Correlation (DIC) technique was used for the composite tensile tests. The DIC, a non-contacting method able to measurement full-field deformations

[135,136], has been very useful to analyses the cracking process parameters. The basic principle of DIC consists of an Area of Interest (AOI) which is manually specified and further divided into an evenly spaced virtual grid. The displacements are computed at each point of the virtual grid to obtain full-field deformation, where subsets (set of pixels) and steps (distance between subsets) are determined and, then, the movement of its center point from the reference image (before the deformation) is correlated at subsequent images, tracking the deformities [56].

To perform the technique, it was necessary to create a speckle pattern on the surface of the specimens, which consists of black dots (made by spray) randomly distributed over a white background. A digital recording camera Nikon D90 model was used, controlled by the Camera Control Pro 2 software, ensuring the capture accuracy of images (4200 x 2690 pixels resolution) at 10 s. The image analysis was performed by the software GOM Correlate, used to detect and quantify the cracks and its process during the failure.

4.4. Results and Discussions

4.4.1. Tensile Behavior of the Curauá Fabric Reinforced Composite System

The curauá fabric under tensile test showed a maximum strength of 123.2 MPa, which occurred at 1.03 % strain, as presented in **Fig. 4-10a**. The young's modulus of the bundle of curauá fibers was 14.9 GPa. During the tensile test, the load appeared to be equally distributed, with no region being more stretched than another. As the loading progressed, the more stressed fibers began to fracture. The single filament fibers did not fracture at the same time due to their high strength variability. This mechanism resulted in a type of pseudo strain hardening behavior that can positive influence the composite tensile behavior (**Fig. 4-10b**). At the end of the test, all fibers were completely fractured (**Fig. 4-10c**). Comparing to other fabrics, the curauá specimen presented a tensile strength 84 % higher than jute fabric (66.8 MPa) [137] but 77 % lower than glass fabric (546.4 MPa) [138]. However, the application of fabrics as reinforcement in a cementitious matrix also considers the fiber-matrix interface mechanisms and morphological characteristics.

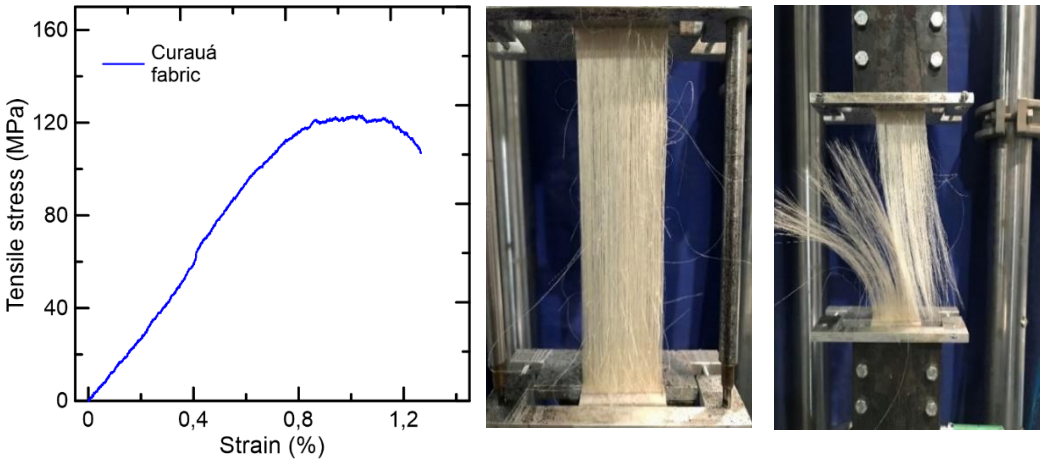

(a) (b) (c)

Figure 4-10. The curauá fabric tensile behavior.

Fig. 4-11 presents the tensile behavior of all composites investigated in the present work. The initial stress/strain response of the composite system was marked by a range of linear-elastic zone where the stiffness of the composite was mainly guided by the matrix properties (marked as zone I in **Fig. 4-11**), which justifies the similar behavior up to this point, especially for the LP250 and LP1000. The linear zone ended by the first crack formation (zone II), but the load carrying capacity continued to increase due the ability of the natural fibers in bridging and arresting the cracks. After the first crack formation, other matrix cracks also initiate to grow throughout the specimen at approximately regular intervals and begin to propagate across the length (zone III). A similar behavior was also observed for natural sisal fiber reinforced cement composites [4]. The decay rate shows that crack spacing decreases as the number of cracks increases, indicating an inverse relationship, as can be seen in **Fig. 4-11b** and **Fig. 4-11c**.

The average first-crack tensile stress up to the end of the linear-elastic zone was 4.6 MPa and 4.3 for LP500 and LP250, respectively, representing a difference of 7%. At the LP1000 curve (**Fig. 4-11d**) it was possible to notice a distinguishable Bend Over Point (BOP) indicating the crack propagation across the width of the specimen. A similar behavior was also observed for man made textile reinforced concretes [57]. All the laminate plates reinforced with three layers of curaua fibers presented multiple-cracking behavior followed by strain hardening under tensile loading. The mechanical behavior and DIC analysis of the specimens are summarized in **Table 2**.

The highest tensile strength was observed for the LP500 composite, followed by the LP250 and LP1000 (26 % and 33 % lower, respectively). The composite system provided high mechanical performance in all cases, even for the LP1000 which demanded the system of overlapped layers. It is worth to mention that this specific manufacturing method (LP1000) proved to be efficient, providing the same mechanical behavior found in continuous fiber-composites. Comparing the LP250 and LP1000 samples, and considered that LP250 represents 1/4 of the LP1000 length, the difference presented was approximately 10 %.

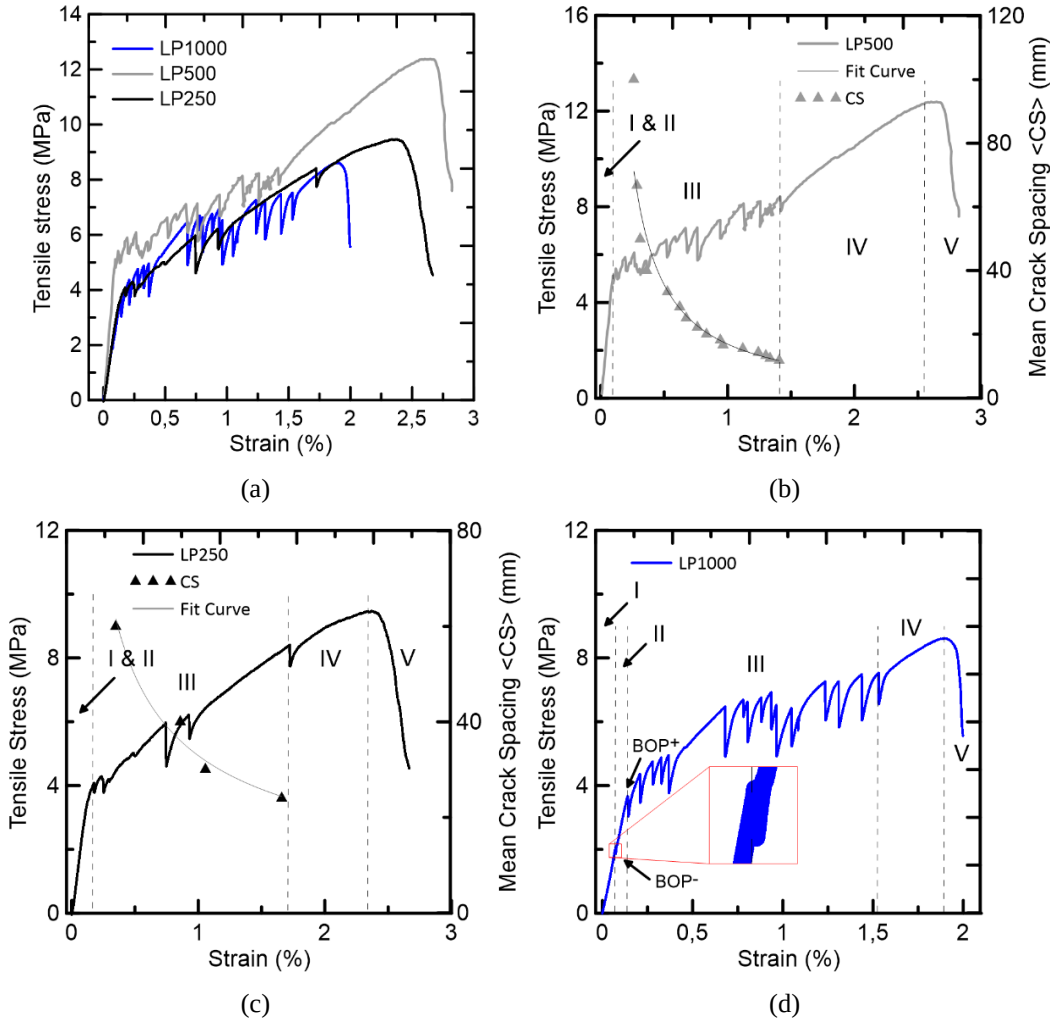

Figure 4-11. Tensile curves of all curaua reinforced composites (a), stress and crack spacing plotted against strain of LP500 (b) and LP250 (c), and LP1000 zoon separated first and second stages (d).

Table 4-2. The mechanical behavior and DIC analysis of Curaua Unidirectional Fabric Reinforced Composite.

Sample	Mechanical properties				DIC analysis	
	First-crack tensile strength (MPa)	**Ultimate tensile strength (MPa)**	**Strain to failure (%)**	**Young's modulus (GPa)**	**Number of cracks**	**Mean crack spacing (mm)**
LP1000*	3.67	8.60	1.9	2.83	11	37.5
LP500	4.60±0.25	12.79±1.63	2.7±0.2	4.75±0.75	16	11.7
LP250	4.35±0.30	9.54±0.80	2.4±0.6	3.33±0.20	4	24.0

* Only one specimen was tested.

Fig. 4-12 presents the cracking pattern of LP250, LP500 and LP1000 specimens, respectively, by the longitudinal strain fields (ε_{yy}) obtained from DIC analysis at approximately 8.0 MPa tensile strength. The 5 % of fraction volume and the arrangement of curaua fibers as reinforcement were able to bridge cracked matrix with new fine cracks formation for all specimens. The composite presented multiple cracking behavior during the tensile loading, which provided an increase at the ultimate tensile strength.

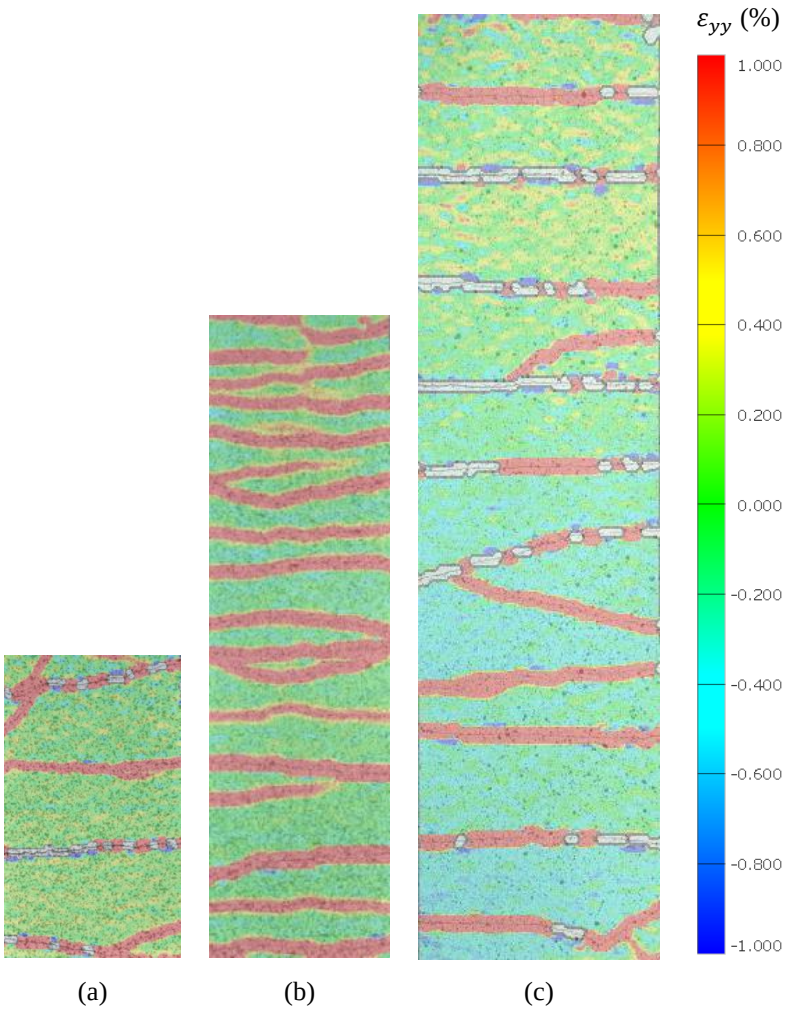

Figure 4-12. The cracking pattern of the composites during the tensile load by DIC: LP250 (a), LP500 (b), and LP1000 (c).

Fig. 4-13 corresponds to the distribution of the longitudinal strain (by DIC) along the normalized AOI length of specimens. Each peak represents a crack and the crack spacing can be measured as the distance between the strain peaks, so the number of cracks and the mean crack spacing (CS) were also obtained from the DIC data. The LP500 presented the highest number of cracks along the gage length (around 16), followed by LP1000 (11) and LP250 (4), respectively. It is possible to notice that the number of cracks was inversely proportional to its longitudinal strain.

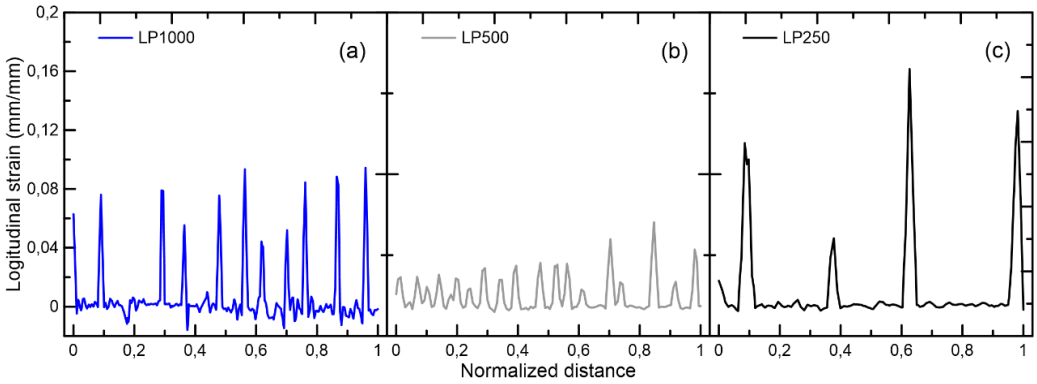

Figure 4-13. The crack formation pattern by DIC analysis of LP1000 (a), LP500 (b) and LP250 (c).

The LP500 higher mechanical performance may be associated with this relationship between the number of cracks and its strain. It can be assumed that as higher the number of cracks, less strained is the cracks (individually), thus, less concentrated is the stress in each crack. Therefore, the number of cracks can directly influence the strength of strain-hardening behavior. For the LP1000, which presented a higher number of cracks then LP250, the lower tensile strength may be associated with its manufacturing method. Even providing the same strain-hardening behavior as the other samples, it is possible that the system of overlapped layers causes to material a slightly loss of strength, but not compromising its final performance.

4.4.2. Composite Bending Behavior

All specimens (LP1000, LP500, and LP250) under four-point bending load presented multiple-cracking pattern and a deflection hardening behavior, providing deflection capacity without losing flexural strength, as presented in **Fig. 4-14**.

(a) (b) (c)

Figure 4-14. The deflection capacity without losing flexural strength of LP1000 (a), LP500 (b) and LP250 (c).

Comparing to the tensile test specimens, the behavior at the elastic linear region was very similar for all specimens (governed by the matrix properties), but in this case a trend line at the post-crack region can be noticed, which means that the composites presented a similar post-cracking stiffness pattern during the flexural-hardening. This behavior can be traced back to the composites design methodology (matrix and fibers arrangement) which resulted in a uniform mechanical behavior that did not present divergent characteristics. **Fig. 4-15** presents the behavior of all specimens under four-point bending tests.

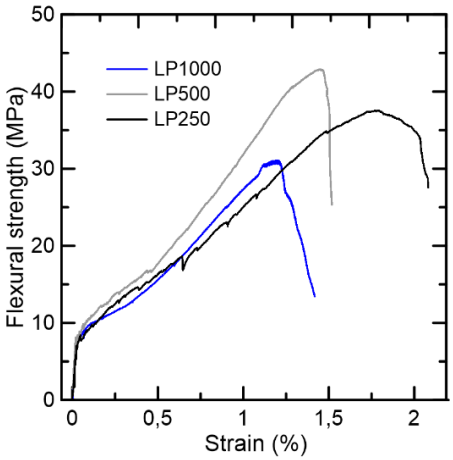

Figure 4-15. The mechanical behavior of all specimens under four-point banding tests.

Concerning the strain capacity of composites, the LP250 and LP500 presented a very close mean value up to the ultimate strength, 1.7 % and 1.6 % respectively, while LP1000 shows a 29 % lower result (1.2 %). These results can be explained by the geometries calculation, which consider the outer support span, while the deflection to failure results followed the expected according to the length of specimens, being LP1000 166 % and 90 % higher than LP250 and LP500, respectively.

About the ultimate flexural strength, LP250 and LP1000 specimens were approximately 16 % and 27 % lower than LP500. It can be explained by the fibers anchor length, including the region beyond the outer support span, which may have provided a better bending load distribution and providing the appearance of more cracks during the LP500 multiple cracking stage. This pattern was also observed in tensile testes, where LP500 showed higher strength followed by LP250 and

LP1000, respectively. **Table 4-3** summarizes the mechanical characteristics of the composites under four-point bending tests.

Table 4-3. Characteristics of composites under four-point bending tests.

Sample	First Crack Flexural Strength (MPa)	Ultimate Flexural Strength (MPa)	Deflection to Failure (mm)	Strain to Failure (%)	Young's Modulus (GPa)
LP1000	7.41±0.07	30.13±0.93	52.7±0.4	1.2±0.0	30.31±0.93
LP500	5.41±2.12	39.18±3.05	27.8±2.2	1.6±0.1	26.32±7.15
LP250	6.21±0.54	33.18±3.35	19.8±0.5	1.7±0.1	22.42±5.55

During the bending tests, at the ultimate tensile behavior, was noticed that the LP500 presented the highest load capacity while the LP1000 did not surpass the other samples. This behavior corroborates the previous hypothesis that the system of overlapped layers may have caused a slight loss of strength but without compromising the composite performance.

4.4.3. Cyclic Behavior

The specimens submitted to cyclic tests still presented the multiple-cracking formation and the flexural hardening behavior, even under the mechanical degradations caused by the cycles, as can be seen in **Fig. 4-16**. As expected, the unloading and reloading loops do not coincide when comparing their inclination, the E_{cyc} became more and more acute over the cycles and no parallel loop was noticed, as presented by other authors [63,139]. It means that there is a stiffness degradation for the entire loading-unloading range, even if the flexural strength still presents gains caused by flexural hardening. These gains by results in a significant increase of the cumulative energy, showed in **Fig. 4-16a**.

Comparing the cyclic to the monotonic loading curves (**Fig. 4-16b**), it is possible to verify that the initial behavior is the same: both curves presented a very close angle at the linear-elastic region but, after the first crack formation, a loss of stiffness can be seen for the cyclic loading curve during the flexural-hardening behavior zone. This behavior may be explained by the multiple crack formation, which during the unloading, do not entirely recover their initial stage after formation. It can be explained by the strain of the fibers, maybe the rupture of the curauá micro-structure (microfibers [24,116]), or even their displacement (pullout), which is directly related to composite degree of reversibility, making the material

less rigid, as described by Boulekbache *et. al.* [134]. Besides, in this case, the energy of the process did not concentrate on a single opening crack but fractioned in a multiple cracking system. The fit curves of reversibility degree presented a plateau (**Fig. 4-16c**) that may be associated to the flexural-hardening behavior of the composite, because of its deflection capacity without losing flexural strength after first-crack formation.

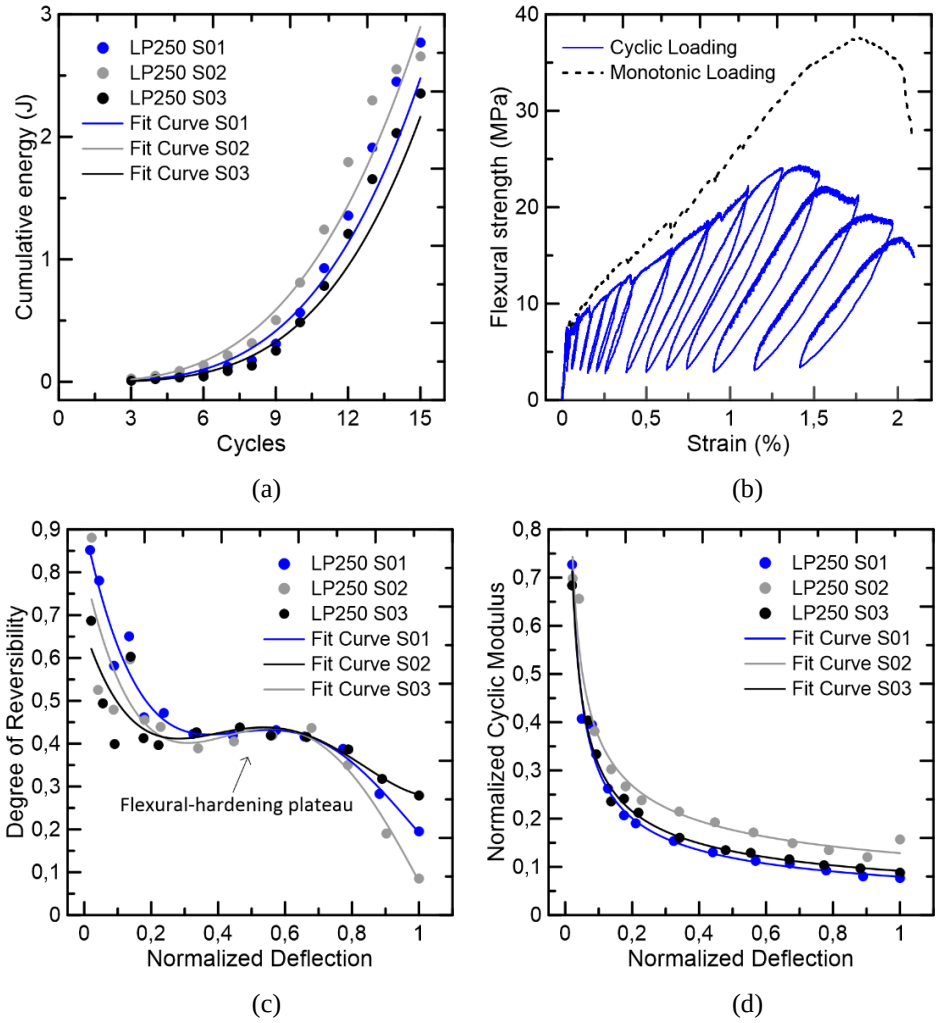

Figure 4-16. The cumulative energy along the cycles (a), the comparison between cyclic and monotonic curves (b), the curves of reversibility degree (c) and the cyclic modulus (d).

The normalized cyclic modulus (**Fig. 4-16d**) shows the evolution of material damage along with the deflection, which is also related to the stiffness loss over the cycles [63]. All specimens presented the same pattern of mechanical degradation where the fibers provided a progressive damage behavior, acting as a regulator of damage, instead of the abrupt rupture of the matrix. This understanding of composite mechanical degradation is fundamental to its application for

strengthening of existing structures aiming to improve bending capacity. In a real scenario, it must have the ability to prevent, or at least delay, a structural collapse.

4.4.4. Combined Loading Compression Tests (CLC)

Fig. 4-17a presented the compressive stress vs. strain behavior of the CLC specimens and conventional cylindrical tested under uniaxial compressive loading. Comparing the composite CLC and matrix axial compressive behavior, the CLC specimens presented strength results that are 13% lower. At first, it can be justified because the relation of these two groups of specimens involves different parameters, as material components and structural design, besides the test procedures. The fibers arrangement is another point to that influences the decrease in strength of the CLC specimens. When longitudinally arranged under compression loading, fibers do not perform as the proposed reinforcement, but act like a material imperfection. Said et al. [140] explains that the reason for this strength decrease at compressive tests are the low-elastic modulus of fibers compared with concrete, which cannot sustain any loading adequately after the first crack. The CLC specimens' final failure occurred within the gage section for all specimens and the failure mode occurred by delamination, governed by their laminate configuration, as showed in **Fig. 4-17b**. The **Table 4-4** summarizes the mechanical characteristics of the composites, under combined loading compression, and the matrix under axial load.

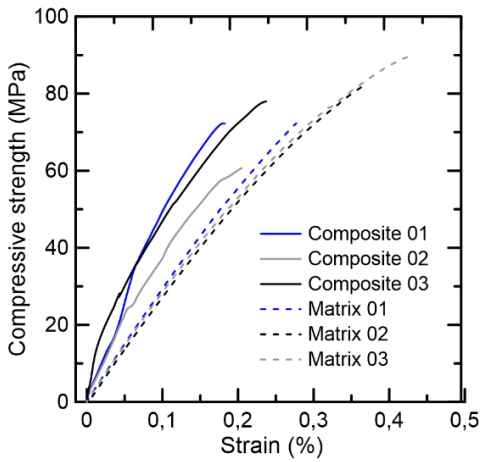

(a)

(b)

Figure 4-17. Behavior under compression load of Curauá cement-based composites: CLC composite tests and matrix conventional compression tests (a), and a representative failure mode of CLC specimen (b).

Table 4-4. Mechanical characteristics of composite (under combined loading compression) and the matrix (under axial load).

Sample	Compressive Strength (MPa)	Strain to Failure (%)	Young's Modulus (GPa)
Composite	70.30±7.19	0.21±0.02	35.07±5.85
Matrix	81.27±7.14	0.36±0.06	23.51±0.80

The specimens under CLC test presented a difference at strain capacity (49 % lower) and a modulus around 33% higher. This false increase in stiffness actually can be justified by the different acquisition methods of strain. While the CLC strain was measured by gages on the delaminated region, the strain of cylindrical matrix specimens was measured by a LVDT oriented by the longitudinal axis. However, even considering all the divergences, it was possible to notice a similar pattern during the compression loading probably ruled by the matrix properties (the same ratio presented in both test samples).

Even tested in its most deficient orientation, longitudinally (guided by fibers), the composite under the CLC test showed high strength and strain capacity, making it possible to compare it with the unreinforced matrix under axial load at the same graphic scale. This compressive stress comprehension is required for this material application, such as the strengthening of columns.

4.4.5. Structural Behavior

Fig. 4-18a presents the results of the structural tests performed in the reference beam (or Non-Reinforced Beam – NRB) and the beam reinforced with the Curauá composite. The Reinforced Beam (RB) presented the load peak of 41.9 kN at 9.18 mm of deflection, while the NRB load peak was 36 kN at a deflection point 76 % higher (16.16 mm). This can be traced back to the fact that the NRB load peak appears during the rebar yielding process. The post-peak behavior of RB under bending test may be characterized as a slip softening due the pull-out process of the reinforcement fibers, which occurs after the composite multiple cracking, causing a yielding delay on the rebars. Comparing both experimental moment-

curvatures (**Fig. 4-18b**), the RB showed higher stiffness and ductility, which also can be associated with the multiple cracking behaviors of the reinforcement material.

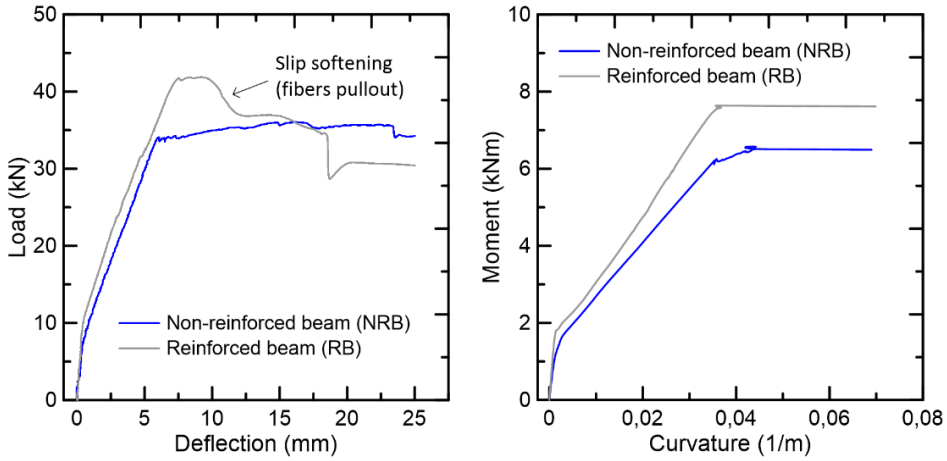

(a) (b)

Figure 4-18. The mechanical behavior of NRB and RB (a) and their experimental moment-curvatures (b).

Fig. 4-19 presents the load-deflection relationship along the beams at different loading stages. The deflection levels were measured by the three LVDTs on the beams bottom face. At 10 kN, both beams presented a linear behavior with already cracked concrete, however the RB demonstrated a higher stiffness. The RB also presented a higher stress level (41.7 kN) when compared to NRB at the start of the rebar yielding point (34.1 kN), about 22 %, and a directly proportional mid span deflection at this point (7.49 mm and 6.08 mm, respectively). This mechanism can be explained by the strength improvement and yielding delay due to the bridging action of the reinforcing fibers [127], which also may be improved by the excellent bond between beam and its reinforcement. From this point to the load peak, the deflections increased to 9.18 mm (RB) and 16.16 mm (NRB), within respective loads of 41.9 kN and 36 kN. At this range, the RB specimen presented an irrelevant load increase, while the NRB showed an increase of around 6 %. However, the increases in deflection were 23 % (RB) and 166 % (NRB).

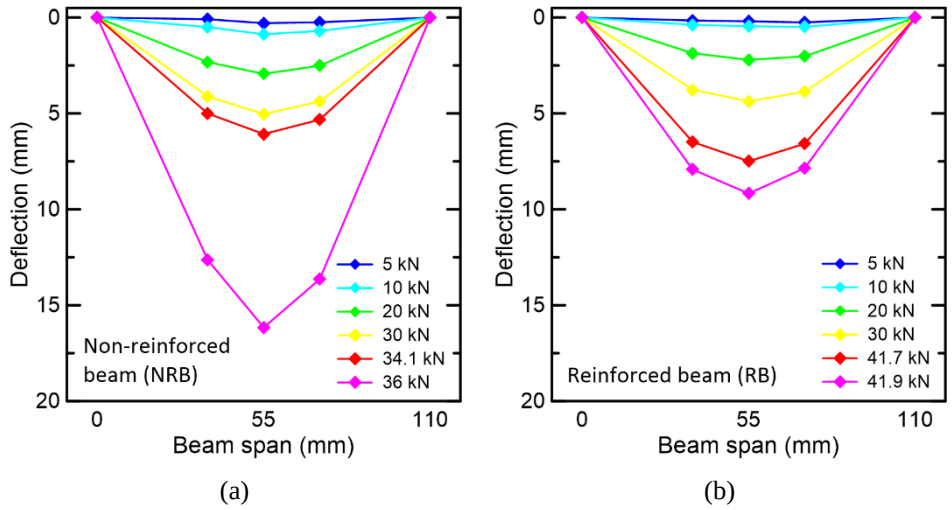

Figure 4-19. Load-deflection relationship along the beams at different load stages: NRB (a) and RB (b).

As mentioned before, this higher deflection presented by the NRB occurred because its peak appears during the rebar yielding stage, while the RB demonstrated a higher load capacity due the reinforcement strain-hardening behavior (which retarded the yielding process of the rebar). The same load capacity increase and deflection decrease was presented by Schladitz at al. [126] in textile high-performance carbon reinforced-composite as concrete slabs reinforcement. **Fig. 4-20** presents the load-strain (measured by strain gages) relationship along the steel rebars at different loading stages and makes possible to better comprehend these yielding delay mechanisms. For the reference beam (named NRB), after the cracking of concrete, the steel rebars tensile stress is locally concentrated (**Fig. 4-20a**), mainly in the cracked region, causing an early yielding. For the Reinforced Beam, on the other hand, even after the cracking of concrete the tensile stress remains equally distributed along the rebars (**Fig. 4-20b**), which may be associated to the strain-hardening capacity of the composite used as reinforcement, providing a higher strain capacity before the yielding stage.

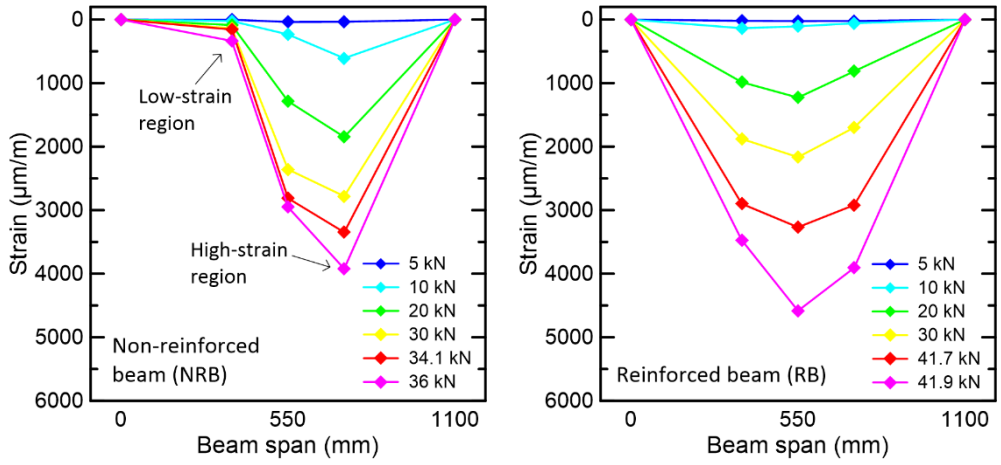

(a) (b)

Figure 4-20. Load-strain relationship along the steel rebars at different load stages: NRB (a) and RB (b).

Both specimens did not present signs of failure by shear. The used strain-hardening cementitious composite reinforced with unidirectional curaua fabric (LP1000 design) as structural reinforcement showed a high bond performance, even without any special surface preparation, presenting no delamination or debonding. The final failure was obtained by crushing the concrete at the top of the specimen, as presented in **Fig. 4-21**.

(a) (b)

Figure 4-21. The end of the bending test marked by the crushed concrete at the top of the specimen (a) and the stretched fibers at same point (b).

Aiming to corroborate the experimental tests, an analytical model for the bending capacity of concrete beam reinforced with natural fibers cement-based composites was proposed. In accordance with the design method for steel reinforced concrete, the proposed analytical model was based on the following assumptions: 1) Bernoulli's principle for plane sections; 2) Concrete´s tensile

strength was ignored; 3) Perfect bond between matrix, steel rebars, and natural fibers reinforcement; 4) At least one material reaches the ultimate strength, obtained by their experimental stress-strain curves.

For the reinforcement (steel rebars and natural fibers), an elastic-linear behavior was assumed until its ultimate strength. For each of the three layers of natural fibers reinforcement, the ultimate strength was determined using experimental results (previously presented at item 4.4.1). The behavior of the experimental compressive strength of concrete was described by **Equation 4-1**, according to BS EN Eurocode 2 [141]. **Fig. 4-22** presents a diagram for the stress-strain relationship of the material, based on the equilibrium of the forces. For each curvature, the equilibrium of forces creates a moment.

$$\sigma_c = f_{cd}\left[1 - \left(1 - \frac{\varepsilon_c}{\varepsilon_{c2}}\right)^n\right] \quad \textbf{(Eq. 4-1)}$$

For $0 \leq \varepsilon_c \leq \varepsilon_{c2}$, and $\sigma_c = f_{cd}$ for $\varepsilon_{c2} \leq \varepsilon_c \leq \varepsilon_{cu2}$.

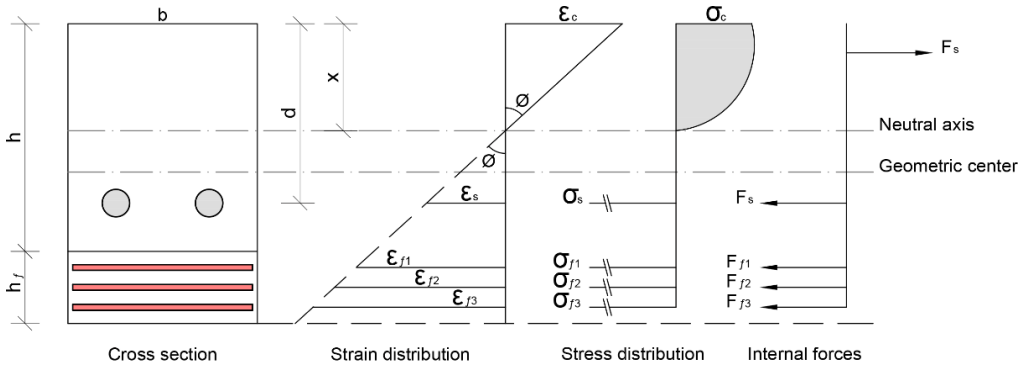

Figure 4-22. Scheme based on the equilibrium of internal strain and stress for the RB specimen.

The force predictions for curvatures were performed by an iterative calculation, and the neutral line position was determined by the forces and moments equilibrium. The operation was performed up to the ultimate strain limit of inputted materials is reached. The force interactions were determinate by the stress-strain diagram integrating. The analytical model of the section was calculated by the following equations (**Eq. 4-2 to Eq. 4-5**):

$$\sum F = 0: \; -F_c + F_s + F_{f1} + F_{f2} + F_{f3} = 0 \qquad \textbf{(Eq. 4-2)}$$

$$-[\int \sigma_c \, b d_x] + \sigma_s A_s + \sigma_{f1} A_f + \sigma_{f2} A_f + \sigma_{f3} A_f = 0 \qquad \textbf{(Eq. 4-3)}$$

$$\sum M = 0: \; -M_c + M_s + M_{f1} + M_{f2} + M_{f3} = 0 \qquad \textbf{(Eq. 4-4)}$$

$$-[\int \sigma_c b x d_x] + \sigma_s A_s \left(h_f + h - d\right) + \sigma_{f1} A_f \frac{h_f}{4} + \sigma_{f2} A_f \frac{h_f}{2} + \sigma_{f3} A_f \frac{3h_f}{4} = 0 \qquad \textbf{(Eq. 4-5)}$$

From the model interactions, the moment-curvature were determined for each position of neutral line and then the analytical curves were predicted for the NRB and RB. It is worth mentioning that the analytical model for the reference specimens (NRB) did not considered the natural fibers reinforcement elements. **Fig. 4-23** shows the experimental and analytical moment-curvature relationships for both tested beams. At the initial load application, during the linear elastic behavior, the specimens (analytical and experimental) of both groups presented the same stiffness. However, after the cracking of the concrete, the analytical curves presented a sudden drop that does not appear at the experimental curves. This can be explained as the analytical model performs an abrupt transition from one stage to another, while in practice, this transition occurs gradually with the appearance of several cracks along the beam.

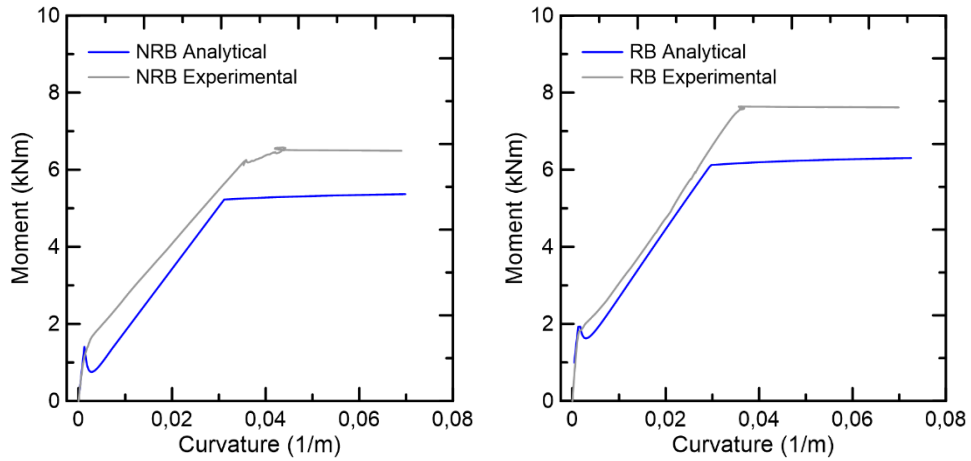

(a) (b)

Figure 4-23. Experimental and analytical moment-curvature relationships for the beams: (a) NRB and (b) RB.

Nevertheless, both the experimental and analytical moment-curvature relationships exhibit a yielding growth-curve up to a nearly horizontal yield plateau. These behaviors between the experimental and analytical curves are almost parallels.

4.5. Conclusions

The arrangement of cementitious composite reinforced with longitudinal curauá fibers provided strain and flexural hardening behavior for all specimens analyzed, even for the longer length systems which demanded the overlapped layers. The used overlap system demonstrated to be efficient, providing the desired mechanical behavior to the laminate plate composite under tensile and flexural loads.

Under cyclic loading, the composite material still presented the multiple-cracking behavior, but a loss of stiffness was detected when compared with its monotonic curve. The energy of failure was released gradually over the cycles and, about the reversibility degree, a plateau was noticed and associated to the flexural-hardening.

The application of the natural fiber composite as a structural reinforcement provided an increase at the ultimate strength of the structural beam (about 16%) before its maximum deflection was achieved. After this point, the reinforced beam first presents a split softening behavior by the fibers pullout before entering to a delayed yielding zone. The adopted theoretical model gave very accurate prediction of the moment-curvature for the beam reinforced with the laminate composite subjected to static load.

The developed natural fiber-composite demonstrated high performance in the material level and excellent behavior as a structural component, providing a higher load and strain capacity to the reinforced beam.

5. On the Shear Behavior of Natural Curauá Reinforced Cement Based Composite Systems

The use of fiber-reinforced cementitious matrix (FRCM) for shear strengthening of concrete structures has been widely investigated, and its field application is not an uncommon practice. However, most of this work is limited to synthetic fibers. Thus, the present study seeks to comprehend the shear mechanical behavior of a cementitious composite reinforced with curauá fibers and its application as a shear structural reinforcement. The experimental program comprehends Iosipescu tests and Digital Image Correlation (DIC) analyses for the composite specimens, and flexural tests for the strengthened structural beams. Analytical model predictions were compared to experimental results.

5.1. Introduction

Fiber-reinforced cementitious matrix (FRCM) exhibit mechanical improvements when compared to regular cement-matrix, presenting tensile ductility behavior. It occurs because the fibers act as a stress transfer-bridge, preventing the propagation of a single catastrophic crack and leading to the formation of several micro-fissures [51,52]. If the fiber composite, after the first crack, presents higher strain capacity with improved strength, it considered strain-hardening cement-based composite (SHCC) [52,53,55,57,142]. Due to its mechanical properties, in recent years, this type of composite has been applied for rehabilitation and strengthening concrete structures as an alternative to traditional techniques such as fiber-reinforced polymers (FRP) [143]. This method consists of an externally bonded reinforcement system, using dry fibers in the form of open mesh or fabric (usually basalt, carbon, and glass fibers) [144,145].

In the case of shear strengthening, the SHCC can be applied in the shear critical zone, in general with the fibers perpendicularly oriented regarding the longitudinal axis of the beam [144,145]. However, Lee et al. [146] investigated beams strengthened with carbon reinforced-composite, varying the orientation of

the fibers (0 °, 45 °, and 90 °), and concluded that the horizontal orientation (0 °) was the most effective in enhancing the beams load-carrying capacity.

Many authors presented a significant amount of shear performance tests comparing FRCM using different fabric types [147–151]. Loreto et al. [149] evaluated reinforced concrete (RC) beams strengthened in shear with polyparaphenylene-benzobisoxazole (PBO) FRCM, adopting one and four fabric layers, and reported that the increased shear strength was not proportional to the number of applied layers (the four-layered composite provided an increase of 25% higher than that of one layer). Ombres [150] also studied PBO-FRCM as shear reinforcement for concrete elements, presenting substantial results about the shear strengthening (enhancement up to 25%), and showed an experimental-theoretical comparison to corroborate it. Azom et al. [151] investigated cement-based and polymer-based composites as shear strengthening system for concrete beams, and concluded that the cement-based systems (carbon fiber reinforced polymer grid embedded in mortar, and carbon fabric reinforced cementitious mortar) performed more efficiently compared to the epoxy-based system (carbon sheet reinforced polymer), presenting a higher increase in ultimate load and no debonding.

In this field, another promising composite is the cement-based reinforced with natural fibers. This kind of composite presents significant mechanical properties [6,9,27,72,73,76,88,152], and its durability can be substantially improved in the alkaline environment [43,84,117], being an economical and eco-friendly alternative. However, there is a gap in the literature about the shear strengthening of structures by cementitious composites reinforced with natural fibers. The present work studied the mechanical shear behavior of a composite reinforced with curauá fibers and developed its application as shear reinforcement to a structural beam for performance evaluation. At the material level, Iosipescu tests were performed, complemented with Digital Image Correlation (DIC) analyses for accuracy of the results. At the structural level, flexural tests were performed and confronted with analytical models for comparison.

5.2. Materials and Methods

5.2.1. The Curauá Fibers

The curauá fibers used as reinforcement in this work were provided by Pematec Company – Santarém, Pará, Brazil. The mechanical and morphological characterization of these fibers are summarized in **Table 5-1**.

Table 5-1. Mechanical and morphological characterization of curauá fibers.

Mechanical	**Tensile strength (MPa)**	760.0 ± 217.3	
	Strain-to-failure (%)	2.4 ± 0.3	
	Modulus of Elasticity (GPa)	32.2 ± 8.1	
Morphological	**Fiber cross section area (mm²)**	0.006 ± 0.001	Teixeira et al. [116]
	Microfibers per cross section (unit)	404 ± 117	
	Microfibers cross section area (mm²)	17.9 ± 9.9	
	Cell wall thickness (µm)	1.58 ± 0.45	

The basic structure of a natural fiber (monofilament) is composed by a cluster of microfibers arranged in an aligned way, which are composed of countless microfibrils grouped in helical arrangements [18,153]. **Fig. 5-1** shows a curauá fiber cross-section (**Fig. 5-1a**) and its longitudinal surface (**Fig. 5-1b**) by a scanning electron microscope (SEM).

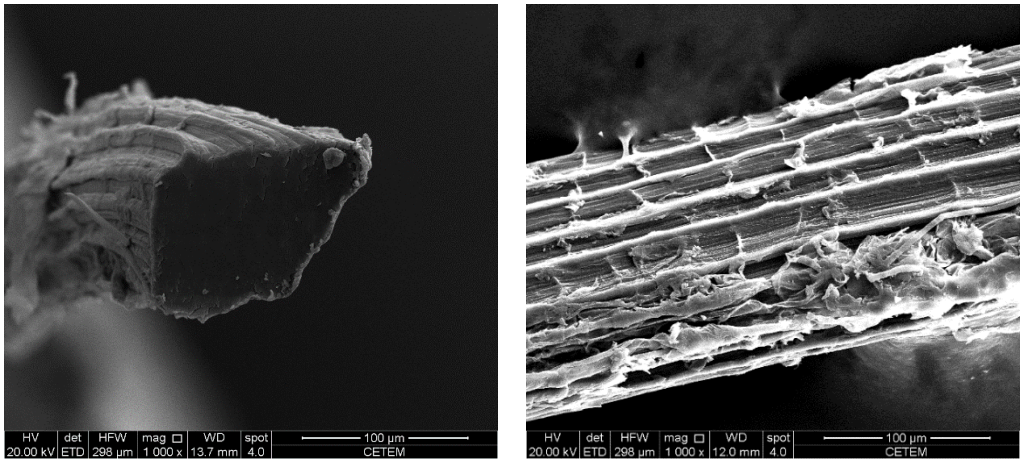

(a) (b)

Figure 5-1. The curauá fiber cross-section (a) and its longitudinal surface (b).

The density of curauá fiber was assumed equal to 1.1 g/cm³ [129,130] for the volume fraction computation purpose. The fibers were treated with hot water at 70

± 3 °C for 1 h, seeking to eliminate the maximum amount of impurities retained on the fiber surface [100,116].

5.2.2. Matrix Design and Mixing Protocol

The mortar matrix for the composite was designed for the ratio of 1:1:0.4 (cementitious material:sand:water). Pozzolans was added aiming a calcium hydroxide free matrix, which provides a higher durability to the natural fibers, as previously reported [4,21,68,122]. The cementitious material was composed, in mass, by 50 % Portland cement type CPV (defined by the Brazilian standard ABNT NBR 16697 [131]), 40% metakaolin (obtained from Metacaulim do Brasil Indústria e Comércio Ltda), and 10% fly ash (from POZOFLY®). The quartz sand had a maximum diameter of 1.18 mm and a density of about 2.67 g/cm³. The superplasticizer GLENIUM® 3500 used proportion was 0.7 % of the cementitious material mass to provide the necessary workability. The average compressive strength of the mortar matrix after 28 days was 81.0 MPa based on the axial compressive test results, and the flow table spread was 355 mm.

For the structural concrete element, the mix design presented in **Table 5-2** was used, based on the work of Lima et al. [132]. It consisted of Brazilian normalized Portland cement CPII-F32 [131], fine aggregate that passed through a 4.75 mm sieve with a fineness modulus (FM) of 2.74, and two different types of coarse aggregates (presenting 9 mm and 19 mm at maximum diameter). The superplasticizer PLASTOL® 4100 was used to adjust the workability of the mix. The average compressive strength of the concrete matrix after 28 days was 33 MPa based on the axial compressive test results, and the slump was 75 mm.

Table 5-2. Concrete mix proportions.

Materials	**Kg/m³**
Portland cement (CPII-F32)	336.0
Natural sand	642.0
Coarse aggregate (9 mm)	441.0
Coarse aggregate (19 mm)	782.0
Water	168.0
Superplasticizer	0.5

The curauá fibers were immersed in water for 1 h, enough time to reach levels close to their maximum saturation [1], and then air-dried for 15 min to eliminate

the excess of water retained on their surface. This method aims to minimize the water absorption from the matrix mixture by the porous structure of the fibers, and therefore increase the system workability. The matrix was produced using a bench-mounted planetary mixer with a capacity of 20 L. The cementitious material and quartz sand were first mixed with 70 % of water for 1 min for homogenization. Thereafter, the superplasticizer previously diluted in the remaining 30 % of water was slowly poured into the running mixer and then mixed for three more minutes.

The total amount of curauá fibers per specimen corresponds to a volume fraction of 5 %, divided into three layers. The fibers were used in a continuous form and arranged in a longitudinally aligned way, as a unidirectional fabric. During manufacturing, the mortar mix was placed in steel molds by a manual layout technique, one layer at a time, followed by one layer of longitudinal aligned curauá fibers. For the Iosipescu shear specimens, a mold was designed to adapt the geometry recommendations of the ASTM 5379/5379M [154], as shown in **Fig. 5-2**. It is worth to mention that the fibers at the notch's region were cut, not deviated.

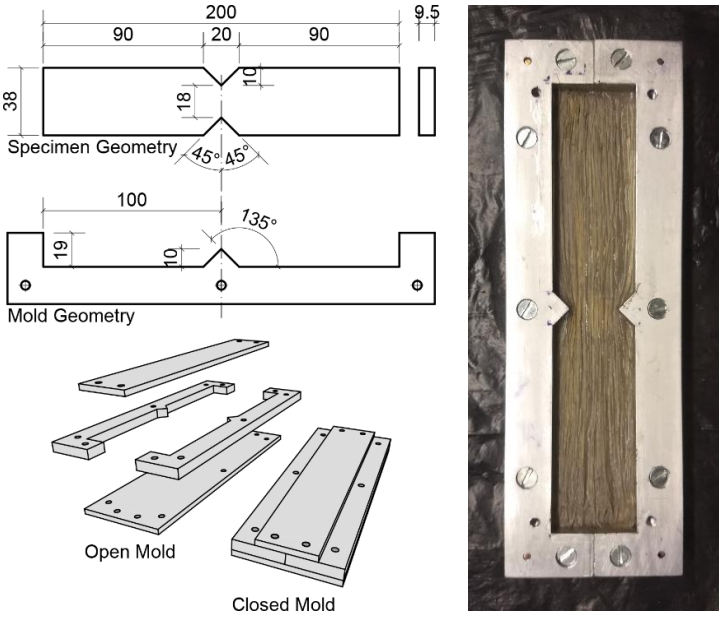

(a) (b)

Figure 5-2. The specimen geometry and a mold schematics (a), and the real mold during manufacturing with a placed layer of aligned curauá fibers (b).

For the composite manufacturing for application as structural external reinforcement, 10 mm thick laminates were produced, comprised of three curauá fiber layers (L1 to L3) and having 150 mm of width and 1000 mm of length (volume fraction of 5 %). To achieve the desired length, overlaps of 70 mm were adopted for continuity. These overlaps were organized alternately, aiming to avoid stress

concentration that could produce a weaker zone. **Fig. 5-3** shows a typical laminate configuration and the overlapping adopted.

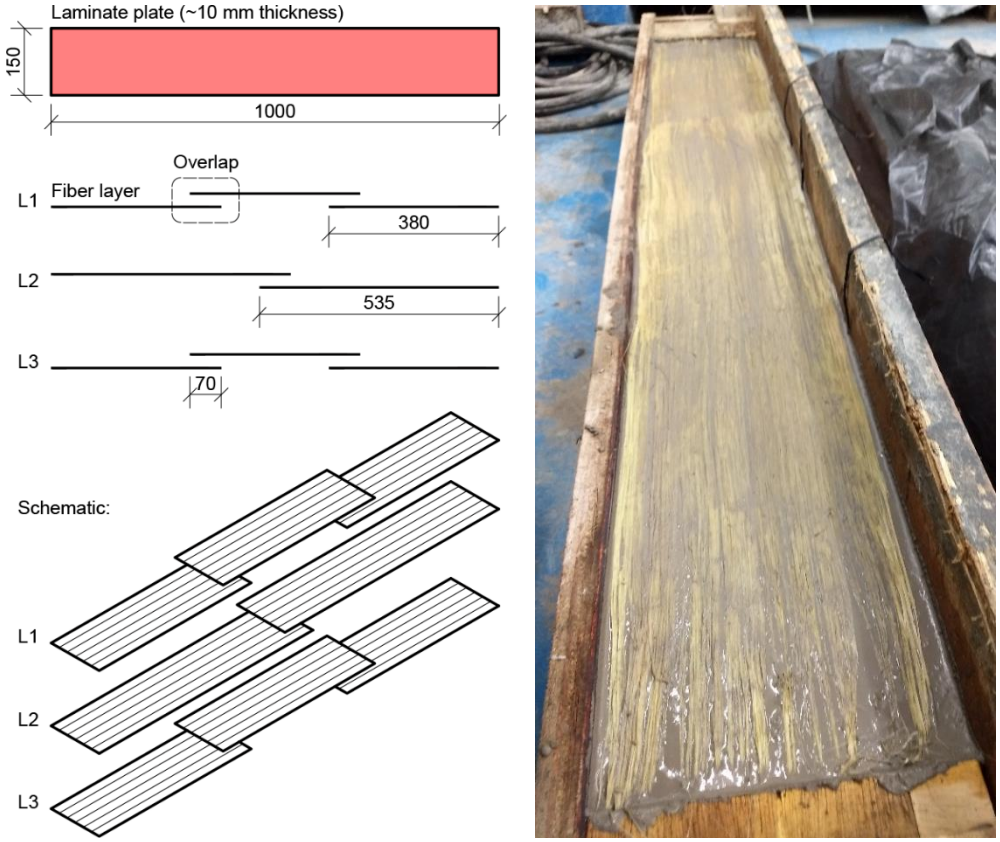

(a) (b)

Figure 5-3. The fibers overlapped layers system (a), and the already layered fibers and mortar over the beam (b). All dimensions in mm.

The 120x150x1200 mm beams were designed with a flexural reinforcement ratio of 0.55% (two 8 mm bars) and with no shear reinforcement along the testing region, seeking a shear-dominated failure mode. For the conventional reinforcement, steel rebars with the nominal yield strength of 500 MPa were used. The beam was cured for 14 days before the composite application. The laminates were fabricated as described in the previous paragraph directly over the lateral sides of the beam and cured for 28 days. For the reinforcement application, the sides of the beam were cleaned and slightly moistened. **Fig. 5-4** presents the schematic beam details and dimensions.

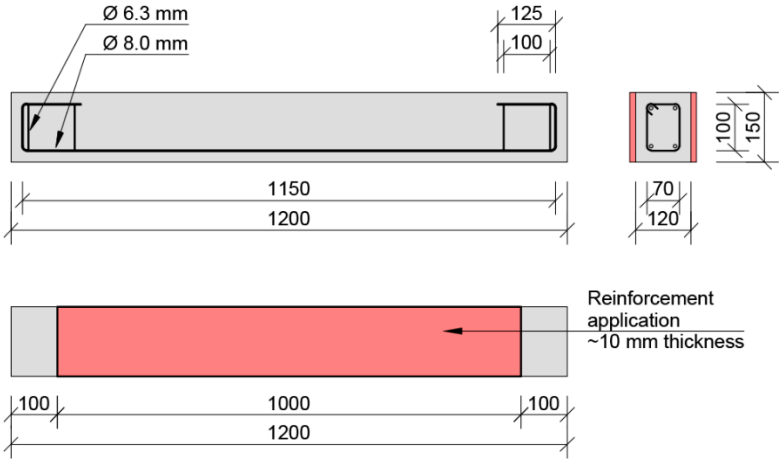

Figure 5-4. The schematic beam details and dimensions. All dimensions in mm.

5.3. Mechanical Tests

5.3.1. The Iosipescu Shear Test

The Iosipescu test followed the recommendations of the ASTM 5379/5379M [154], shown in **Fig. 5-5**. The tests were conducted in a servo-hydraulic closed-loop MTS system, with a 100 kN load cell, under a displacement-controlled rate of 0.1 mm/min. For higher accuracy on displacement measures, an LVDT was installed beside the setup, and, for strain measurement, a ±45° pair of strain gages were positioned at one face of the notched section. Three v-notched specimens were tested.

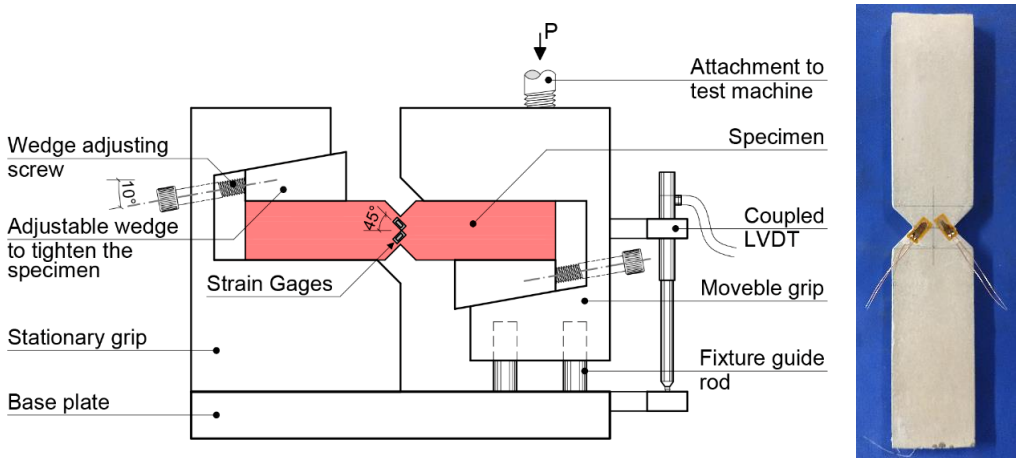

(a) (b)

Figure 5-5. The schematic Iosipescu test (a), and a specimen real specimen (b).

The Digital Image Correlation (DIC) technique was used for the composite shear tests, aiming to better understand the crack evolution process. The DIC, a

non-contacting method able to measurement full-field deformations [135,136], has been very useful to analyze the cracking process.

To perform the technique, it was necessary to create a speckle pattern on the surface of the specimens, which consists of black dots (made by spray) randomly distributed over a white background. This surface preparation was done on the opposite side of the gages. A digital recording camera Nikon D90 model was used, controlled by the Camera Control Pro 2 software, ensuring the acquisition of images with 4200 x 2690 pixels resolution at a rate of 1/10 s. The image analysis was performed using the software GOM Correlate, adopting subsets of 25 pixels. **Fig 5-6**. illustrates the camera position concerning the Iosipescu setup and shows a real speckle-surface specimen.

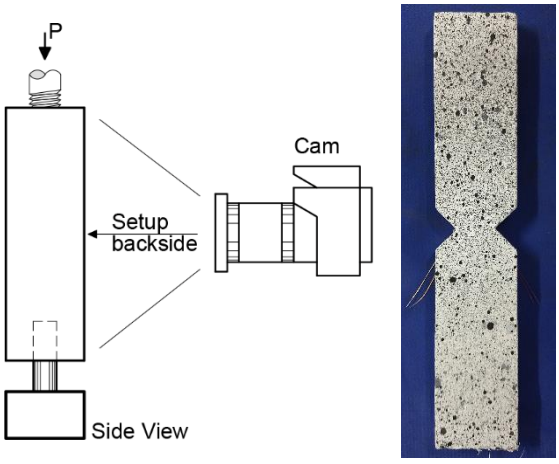

(a) (b)

Figure 5-6. The camera position concerning the Iosipescu setup (a) and shows a real speckle-surface specimen (b).

5.3.2. The Structural Tests

Structural concrete beams were tested in a 500 kN servo-hydraulic MTS actuator mounted in a steel test frame. Strain values were monitored by a total of six 10 mm strain gages on steel rebars (three on each rebar), as presented in **Fig. 5-7**. Three LVDTs were used to measure the deflection: one LVDT was placed at the midspan and the other two were located below load-points. The tests were carried under displacement control at a rate of 1.0 mm/min over an 1100 mm span. A shear span a = 365 mm was adopted, ensuring a ratio a/h between 2 and 2.5 for a shear failure (h = beam depth). Two specimens were tested, a reference without the external reinforcement and another with the side bonded laminate composite.

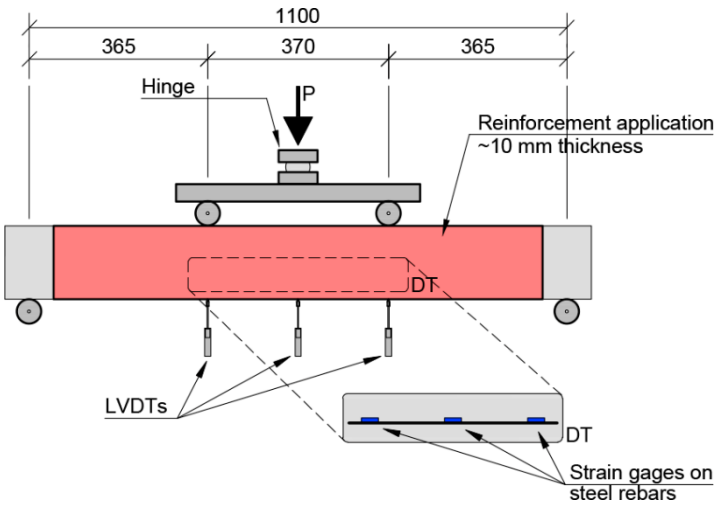

(a)

(b)

Figure 5-7. Scheme of beam test (a) and overview of the experimental setup (b). All dimensions in mm.

5.4. Results and Discussions

5.4.1. Shear Tests

The shear stress curves shown the Iosipescu specimens' mechanical behavior on shear failure (**Fig. 5-8a**). The shear stress was determined following the ASTM 5379/5379M [154], dividing the applied load by the cross section area between the notches. The specimens presented a similar strength capacity, but a significant variation at the shear sliding. The apparent shear strain calculated as the sum of the absolute readings of the strain gages also presented an expressive variation up to its failure, as can be seen in **Fig 5-8b**. It is important to highlight that, in the cracked

stage, there is a reorientation of stress trajectories and, therefore, the states of stress in the region of each strain gage are different, contributing to the dispersion of the results. About the shear mechanical behavior, the composite showed four distinct phases: I) a linear range up to crack formation (up to a shear sliding around of 0.09 mm); II) a shear stress increase accompanied by crack propagation; III) opening of main crack (induced by the notches) followed by the formation of new thin cracks, and a shear-hardening behavior; and IV) a shear-softening crack opening (post-peak). For comparison, Baghi and Barros [155] presented the shear stress versus crack sliding of SHCC reinforced with 2 % by volume of short discrete polyvinyl alcohol (PVA) fibers and described its curve behavior in just three main phases. At the first and second phases, the same mechanical behavior was observed, but without shear-hardening. After that, the shear-softening behavior was observed (non-linear post-peak). **Fig. 5-8c** presents the comparison between curauá and PVA composite curves and describes the four phases, and **Fig. 5-8d** shows the relation between crack opening (measured by DIC analysis) and shear stress during the Iosipescu test, making possible to better comprehend these phases of cracking process during the shear-hardening behavior. Appling the four phases over the crack opening curve, it can be observed that: there is no crack at phase I; in phase II, the formed crack remains with a very small opening, only propagating itself; in phase III, the crack opening increases exponentially up to maximum stress; and in the phase IV, crack opening remains while load capacity is reduced.

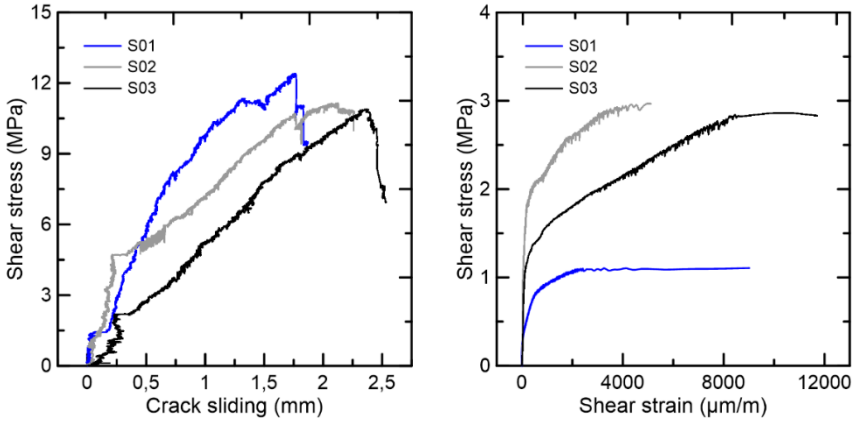

(a) (b)

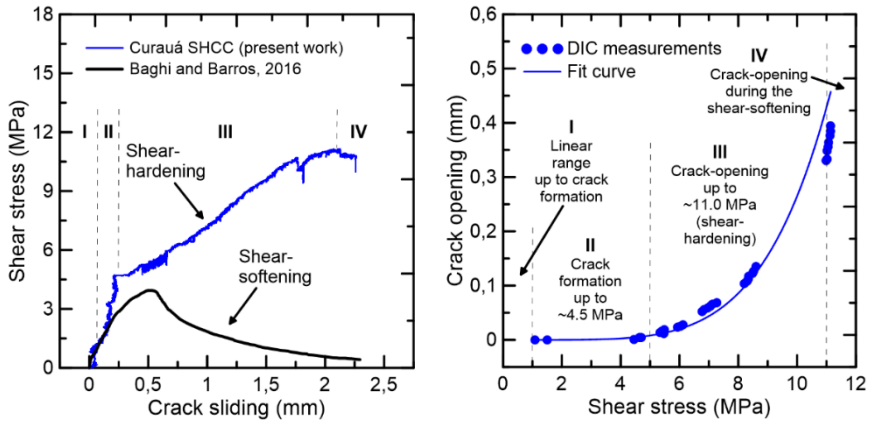

(c) (d)

Figure 5-8. The Iosipescu specimens' mechanical behavior by LVDT displacement (a) and strain gages (b), the comparison between curauá and PVA composite curves (c), and the opening crack behavior during the shear-hardening (d).

Table 5-3 summarizes the composite properties by mechanical and DIC analysis under Iosipescu shear tests. Due to their physical limitation, the pair of gages did not capture the shear strain at the maximum stress, but only up to the 2.3 MPa. It may be explained by the crack formation and opening, which exceeds the gages strain limit. Otherwise, the maximum stress (average of 11.5 MPa) can be correlated with the crack sliding (the axial displacement following the crack orientation) because the range of LVDT goes beyond the crack failure.

Table 5-3. Summarized composite properties by mechanical and DIC analysis under Iosipescu shear tests.

Mechanical analysis	**Max load (kN)**	1.96 ± 0.11
	Max shear stress (MPa)	11.5 ± 0.66
	Crack sliding (mm)	2.09 ± 0.25
	Shear strain (μm/m)	8278 ± 2345
	Modulus of Elasticity (GPa)	6.11 ± 1.49
DIC analysis	**Crack opening at max stress (mm)**	0.38 ± 0.04
	Number of cracks at max stress (unit)	3.33 ± 0.47

The failure mode showed that the crack started exactly at the notch, as expected, but changed its course along the test in approximately 90°, assuming a longitudinal alignment. This course change may have been influenced by the fiber's orientation inside the specimens (also longitudinal), which along the loading may have guided the cracking propagation to its orientation. **Fig 5-9a** shows the specimen strain fields (ε_{yy}) obtained from DIC analysis at approximately 4.5 MPa, where is possible to observe that the crack is slightly curved and, in **Fig 5-9b**

(approximately 11.0 MPa, close to the peak of stress), the same crack is reoriented towards the longitudinal orientation. The image analysis also provided the average crack opening measurement, about 0.4 mm at maximum stress, and the average number of cracks at the same point, around 3.

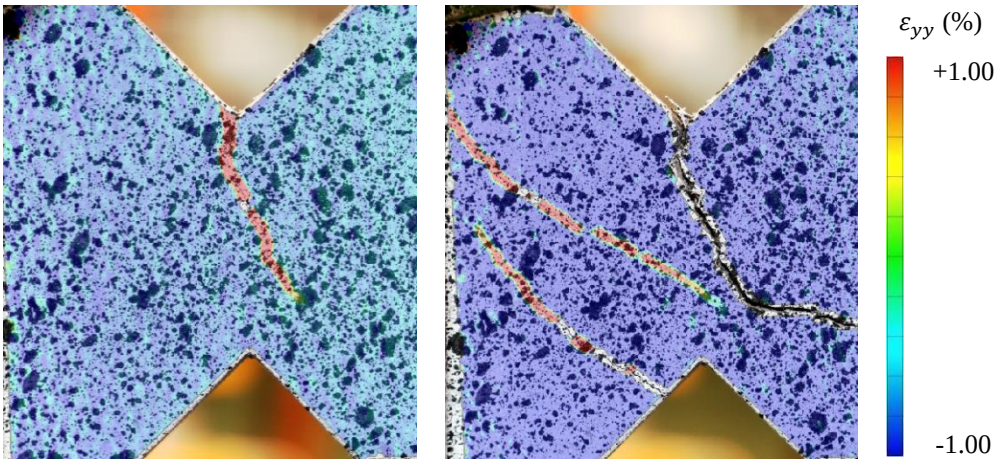

(a) (b)

Figure 5-9. The shear strain fields (ε_{yy}): Iosipescu specimen cracked at 4.5 MPa (a), during its propagation; and the same crack at 11.0 MPa (b), close to its peak of stress.

5.4.2. Structural Behavior

5.4.2.1. Shear Capacity, Load and Deformation Behavior

The load-deflection behavior showed a brittle response for both beams, characteristic of shear failure and almost the same deflection at their ultimate load. Azam et al. [151] also presented this same deflection behavior in their concrete beams, without stirrups, externally reinforced with carbon fiber composite. It can be seen that the externally reinforced beam (RB) was able to provide an increase in shear capacity of about 28% with respect to the non-reinforced beam (NRB), as well as a higherstiffness. The maximum experimental shear resistance (V) of the tested beams were calculated according to **Eq. 5-1**, where L is the distance between supports, d is the shear span (from the load point to the support), and F is the maximum load capacity. For comparison purpose, the shear response beams were normalized, defining μ (**Eq. 5-2**) as the ratio between the applied shear force (V) and the shear capacity of the reference beam (V_c).

$$V = d\frac{F}{L} \qquad \textbf{(Eq. 5-1)}$$

$$\mu = \frac{V}{V_c} \qquad \textbf{(Eq. 5-2)}$$

The mechanical behavior of the tested beams demonstrated that the double side reinforcement was not able to prevent sudden failure but provided to the RB a higher strength capacity. **Fig. 5-10** presents the experimental curves of the normalized shear forces (μ) versus the axial displacement, and the **Table 5-4** summarized the beams mechanical properties.

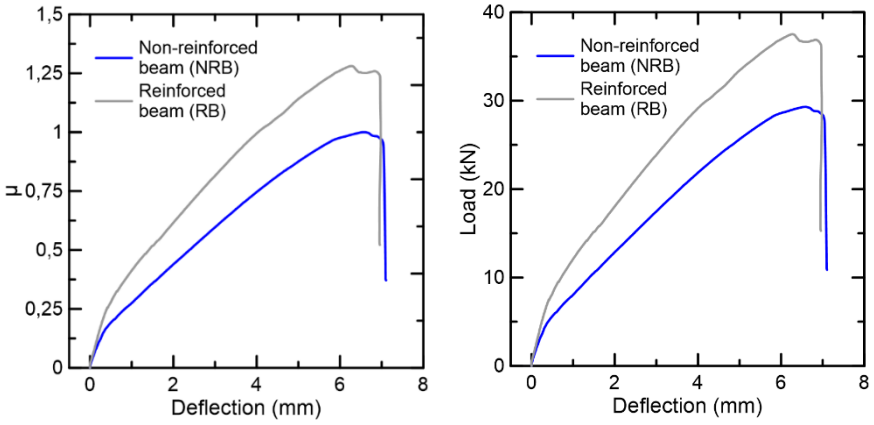

(a) (b)

Figure 5-10. The NRB and RB experimental curves of the normalized shear forces (μ) versus the axial displacement (a), and the load versus the axial displacement (b).

Table 5-4. The NRB and RB summarized mechanical properties.

	NRB	**RB**
Max load (kN)	29.3	37.5
Deflection at failure (mm)	6.6	6.3
Shear resistance (kN)	9.7	12.4
Rebar strain (μm/m)	2581	2880

About the shear strengthening increase, Contamine et al. [147] conducted a comparative study with carbon and glass textile-reinforced mortar as shear reinforcement for concrete beams, adopting two wrapping layouts: the side bonding and the U jacketing, and Escrig et al. [148] also studied reinforced concrete beams shear strengthened with different types of textile-reinforced mortar, using basalt, carbon, PBO (Poliparafenil-benzobisoxazole), and glass fibers, adopting only the U jacketing system. **Table 5-5** shows the maximum load increase provided by each textile composite system regarding their respective reference specimens. For comparison, the increased load capacity of the beam reinforced with the curauá composite was also added. It can be noted that the curauá fabric cementitious composite as shear reinforcement for concrete beams showed a high performance

and did not present an expressive divergence when compared to other systems, especially those based on basalt and glass fibers.

Table 5-5. Comparative of load capacity increase provided by textile composite system as shear reinforcement.

Textile base	Wrapping layout	Increase of ultimate load (%)	Reference
Basalt	U jacketing	30.6	Escrig et al. [148]
Carbon	U jacketing	6.9	Contamine et al. [147]
Carbon	U jacketing	36.4	Escrig et al. [148]
Curauá	Side bonding	28.1	Present work
PBO	U jacketing	43.4	Escrig et al. [148]
Glass	U jacketing	35.6	Escrig et al. [148]
Glass	Side bonding	31.4	Contamine et al. [147]
Glass	U jacketing	37.7	Contamine et al. [147]

Fig. 5-11 presents a load-deflection comparison between the glass (GLSS) [147], carbon (CRBN) [148], and the curauá fiber-composite reinforced beams studied in the present work (CUR). The CUR and the GLSS reinforcement were applied following the side bonding system, while the CAR wrapping was made as U jacketing. Aiming to focus only on the increased properties comparison, all curves were normalized by their references maximum load capacity (kN) and deflection at failure (mm). The curves obtained from the cited references were digitally replicated using the Grapher^{TM} software, and the quantitative comparisons were made based on their respective published data [147,148]. Compared to CUR, GLSS and CRBN provided increased loads of 2.6 % and 6.5 % higher, respectively. It may be stated that CUR provided almost the same range of strengthening as GLSS, considering that the curauá fibers are a natural resource and free of industrial processing. About the deflection capacity, both GLSS and CRBN provided an improvement of more than 90 % compared to the CUR.

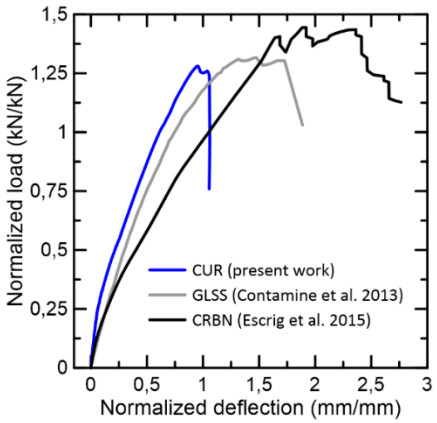

Figure 5-11. The comparison of increased load-deflection properties between the fiberglass-composite and the curauá-composite reinforced beams.

Analyzing the NRB and the RB deformation behavior, the load-deflection relation along the beams at different load stages (**Fig. 5-12**) have shown that the deflections (measured by the three LVDTs) were higher for the NRB at all load stages, corroborating the RB higher stiffness. At the 20 kN load, the NRB showed a deflection level 18 % higher than RB, which means that the composite fulfills its role as reinforcement, absorbing part of the energy during the loading process and providing a higher strength at a lower deflection level. Similar stiffness enhancement was presented by Schladitz et al. [126]. At their ultimate load strength, although both beams have almost the same deflection limits (NRB = 6.6 mm and RB = 6.3 mm). However, the RB presented a higher ultimate strength at the same deflection, around 28 % of increase.

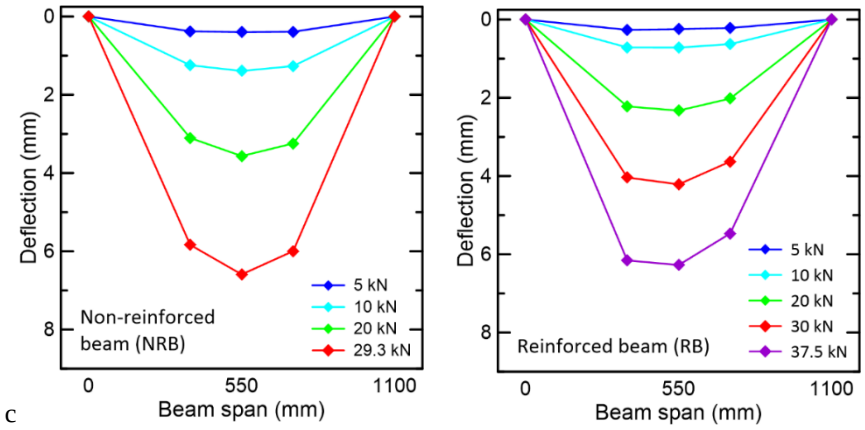

c

(a) (b)

Figure 5-12. The load-deflection relation along the beam at different load stages: non-reinforced beam (a) and reinforced beam (b).

Fig.5-13 presents the load-strain relation (measured by strain gages) along the steel rebars at different loading stages. In general, the NRB showed higher rebar strains at all initial known loads (5 kN, 10 kN, and 20 kN). At the 20 kN load, the NRB rebars strain was 33 % higher than RB, but when their ultimate loads are reached (29.3 kN and 37.5 kN, respectively), the RB presented the higher rebar strains (about 12 %). It can be assumed that the improvement caused by the curauá composite as shear reinforcement provided to the rebars a higher strain capacity. Furthermore, the enlarged cross-section also may have contributed to the increase of stiffness. It is worth mentioning that, in both configurations (NRB and RB), the

longitudinal rebars did not reach nominal yielding at failure, as also reported by Loreto et al. [149].

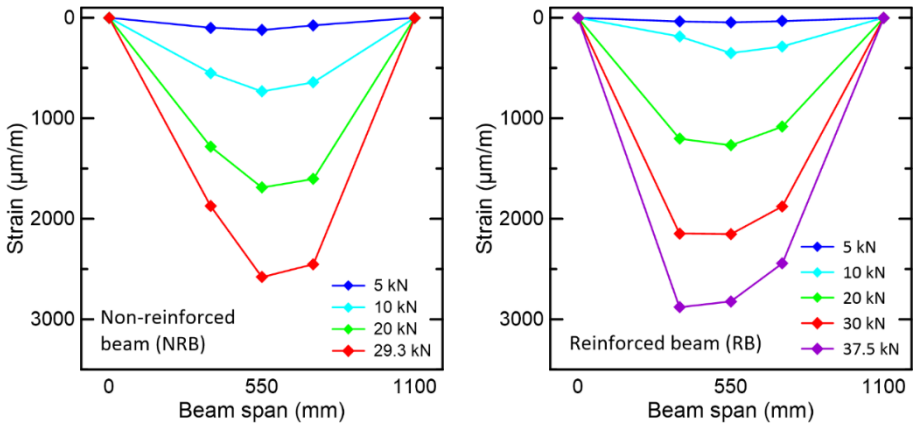

(a) (b)

Figure 5-13. The load-deflection relation along the beam at different load stages: non-reinforced beam (a) and reinforced beam (b).

5.4.2.2. Failure Modes and Crack Patterns

The composite as structural reinforcement showed a high bond performance, even without any special surface preparation, presenting no delamination or debonding from substrate. Both specimens presented the shear failure mode, with the critical crack propagating from the load application towards the support. The NRB presented a typical inclined crack (**Fig 5-14a**), while the RB specimen showed a critical crack comprised of inclined and horizontal segments, similar to the Iosipescu specimens (**Fig. 5-14b**). **Fig 5-14c** shows both crack patterns: 1) a linear propagation of the NRB crack which did not reach the support, and may be justified by the stirrups concentrated only at the end of the beam (avoiding dowel splitting); and 2) a crack propagation that presents a staggered pattern (RB). It is worth to mention that most of curauá fibers did not fail at the final of the test but kept being stretched under a pullout mechanism (**Fig. 5-14d**). It must also be noted that the fibers tend to deviate from their original orientation, accompanying the crack kinematics (opening and sliding). This is possible due to the curauá fiber flexibility and is likely to be followed by local rupture of matrix surrounding the fibers, previously reported in literature for the pullout of inclined short fibers [156]. Along with the shear transfer mechanisms of aggregate interlock, this re-orientation is ultimately responsible for the improvement of shear capacity even though fibers are

not oriented as usual. Due to the low flexural reinforcing ratio, the neutral axis in the cracked stage is very close to the top of the beam and, therefore, it is expected a low contribution of the shear transference through the uncracked zone.

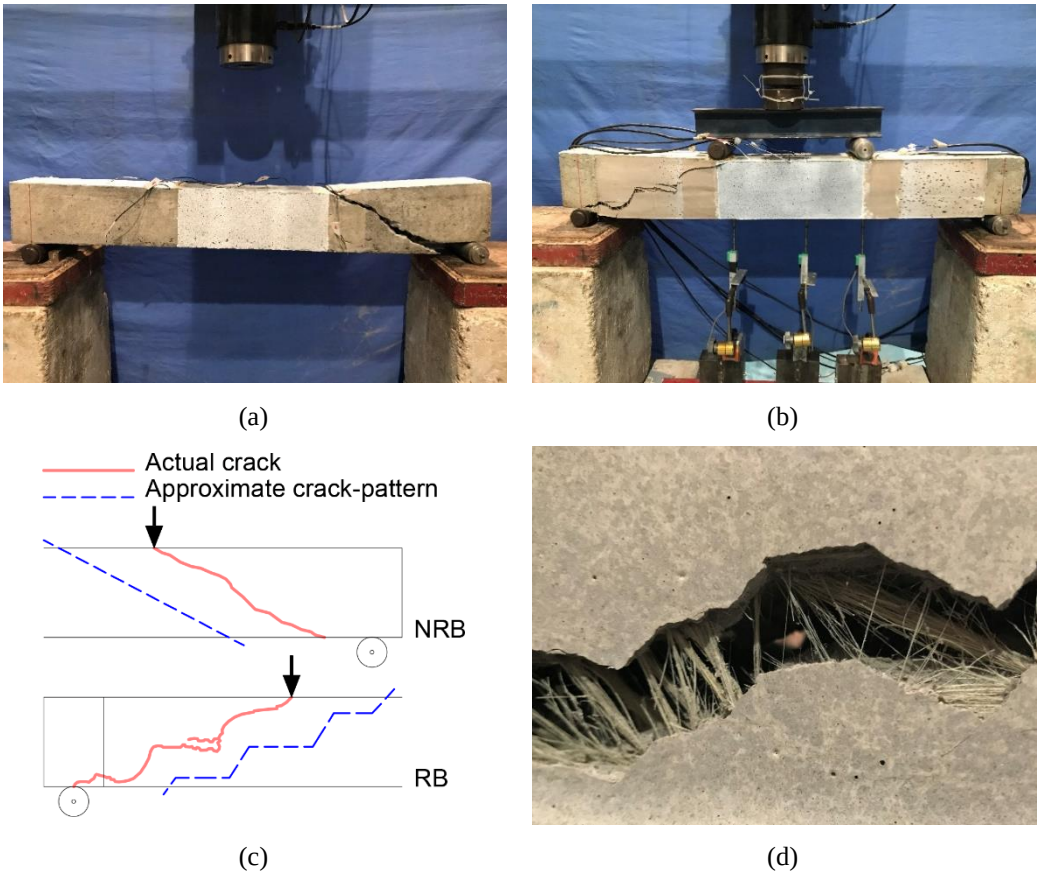

Figure 5-14. The failed non-reinforced beam (a) and reinforced beam (b), a schematic NRB and RB crack propagation pattern (c), and the stretched curauá fibers connecting two separated matrix parts and transfer its load (d).

Moreover, the RB crack pattern made possible to identify different angles along the crack and, consequently, different interactions during shear stress. **Fig. 5-15** schematically illustrates the cracking pattern of the reinforced beam, analyzing the approximate angles along the shear crack and the formed angle by stretched curauá fibers (**Fig. 5-15b** based on **Fig. 5-14d**).

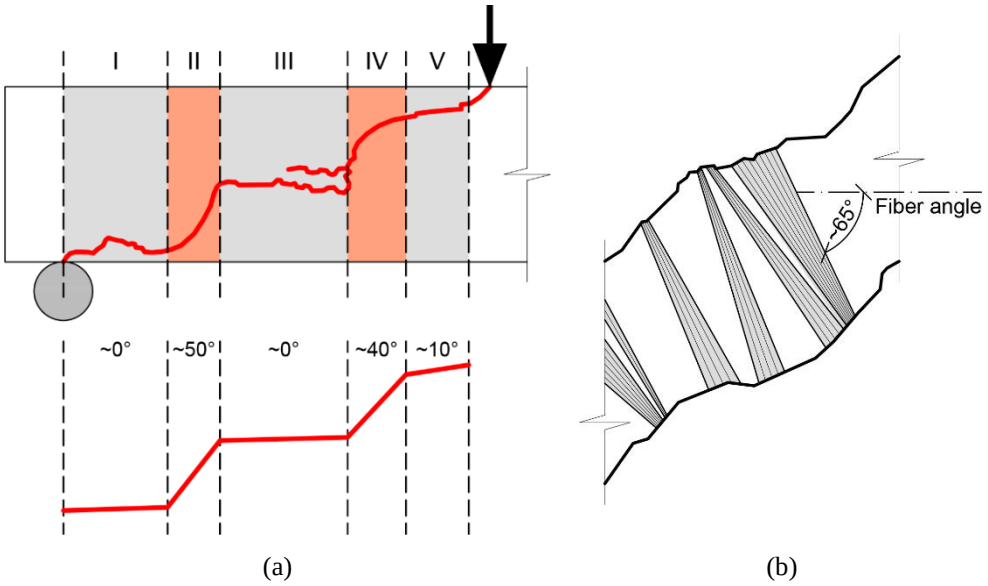

(a) (b)

Figure 5-15. The cracking pattern angles analysis (a) and the angle formed by stretched curauá fibers (b).

5.5. Analytical Study

5.5.1. Analytical Models and Comparison

The use of fiber reinforced-composite externally bonded on structural members to enhance its shear strength can be predicted by analytical models such as ACI 549.4R-20 [144] and the *fib*-Bulletin 14 [145], which are based on the assumption that the combined strength of all elements can provide the ultimate shear resistance of the specimen (V_u) (**Eq. 5-3**).

$$V_u = V_c + V_s + V_f \qquad \textbf{(Eq. 5-3)}$$

Where V_c, V_s, and V_f are the shear contributions of the concrete, the steel, and the composite reinforcement, respectively. Following this model, ACI549 recommends the contribution of fiber reinforced-composite external reinforcement, V_f, to be obtained according to **Eq. 5-4**, where n is the number of fabric layers, A_f is the area of fabric by unit width effective in shear, ε_f and E_f are the strain and modulus of the composite, and d is the effective depth of the composite shear reinforcement.

$$V_{f\ ACI549} = nA_f\varepsilon_f E_f d \qquad \textbf{(Eq. 5-4)}$$

fib-Bulletin 14, on the other hand, recommends V_f to be computed according to **Eq. 5-5**, where ε_f and E_f are the strain and modulus of composite at the principal reinforcement orientation, ρ_f is the composite reinforcement ratio, b_w and d are the

width and the effective depth of the structural beam cross section, α is the angle between principal fiber orientation and longitudinal axis of beam, and θ is the angle of diagonal crack concerning the beam axis.

$$V_{f\,fib14} = 0.9\varepsilon_f E_f \rho_f b_w d(cot\alpha + cot\theta)sin\alpha \qquad \textbf{(Eq. 5-5)}$$

The composite tensile properties (mentioned in the previous chapter) and the geometrical parameters adopted to ACI549 and *fib*14 models are summarized in **Table 5-6**.

Table 5-6. Properties and parameters adopted to ACI549 and fib-Bulletin 14 models.

n	A_f **(mm²/mm)**	ε_f **(%)**	E_f **(GPa)**	***d*** **(mm)**	***t*** **(mm)**	b_w **(mm)**
3	0.19	1.90	2.83	114.7	10.0	120.0

It is worth to mentioning that the ACI549 considers only two wrapping systems: U-jacketing (beams) or continuous complete wraps (beams and columns); however, the studied beam in this work was reinforced using the side bonding system. Another parameter to be considered in the present work is the fabric area (A_f). In the current work the used curauá natural fabric presented only one orientation, unlike most commercial bi-directional fabrics made of carbon, glass, polypropylene and PBO. Besides, ε_f was not restricted to 0.004 mm/mm (0.4%), as defined by ACI549, but considered the composite ultimate tensile strain. This consideration aims to not limiting the model result, as described by Escrig et al. [148]. About the *fib*-Bulletin 14, the angle between the principal orientation of fibers and the longitudinal beam axis needs to meet the condition $\alpha > 0$; however, the proposed design for curauá unidirectional fabric follows the beam longitudinal orientation. Considering that the fiber-reinforcement naturally tends to re-orientate during the crack opening (**Fig. 88**), for the model simplification was adopted α = 45°.

Based on these facts and seeking an approach that matches the experimental conditions presented in this work, a model for the shear strengthening of beams was developed based on the shear mechanical behavior of the studied composite, obtained from the Iosipescu tests. **Fig. 5-16** (based on **Fig. 5-9b**) illustrates the cracking pattern obtained from shear test and the distribution of forces at the notched section (pure shear).

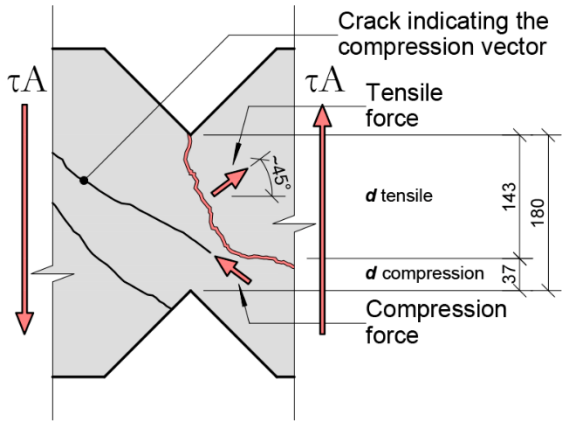

Figure 5-16. Schematic of stresses distribution in the composite during the shear test. All dimensions in mm.

The proposed analytical model was based on the following premises: 1) The resulting tensile force, F_t, is transferred by the fibers; 2) The compression force, F_c, is transferred by the uncracked matrix; 3) The forces are oriented at 45º; and 4) To comply with balance of forces at the notched section, the tensile force is equal to the compression force, and the sum of their vertical components is equal to the shear force. This latter hypothesis leads to:

$$F_c \, sen\, 45° + F_t \, sen\, 45° = \tau \, A \qquad \textbf{(Eq. 5-6)}$$

where A is the cross-section area between notches and τ is shear stress. Making $F_c = \tau_c \, A_c$, where τ_c is a representative shear stress at the uncracked area under compression, A_c, and $F_t = \tau_t \, A_t$, in which τ_t is the shear acting at the cracked area under tension, A_t, **Eq. 5-6** can be rewritten as:

$$(\tau_c A_c + \tau_t A_t) \, sen\, 45° = \tau \, A \qquad \textbf{(Eq. 5-7)}$$

Since $F_c = F_t$, τ_t can be obtained from **Eq. 5-7** as:

$$\tau_t = \tau \, A/(2A_t \, sen\, 45°) \qquad \textbf{(Eq. 5-8)}$$

In the experimental result for the externally reinforced beam, it can be seen that the beam did not present shear-hardening behavior, as observed in the Iosipescu test. This may be associated to the influence of bending moment. Due to the low conventional reinforcement ratio adopted, the area of the compression zone is very small and, therefore, the load-carrying capacity is limited by shear failure at the compression zone, and not by the external reinforcement. Therefore, the maximum shear stress considered for the model was 4.5 MPa (the maximum stress before the appearande of thefull vertical crack in the composite). From this reference value, the average shear stress transferred by the fibers can be computed according to **Eq.**

5-8, considering τ = 4.5 MPa, A = 171 mm^2, and A_t = 136 mm^2, i.e. τ_t = 4.0 MPa. Thus, the shear contribution provided by the composite reinforcement can be described by the **Eq. 5-9**, where b (10 mm) and d (114.7 mm) are the width (at both sides of the beam) and the effective depth of the laminate composite cross section.

$$V_f = \tau_t \, b \, d \qquad \textbf{(Eq. 5-10)}$$

Table 5-7 presents the reinforcement shear strengthening contribution according to ACI549, *fib*-Bulletin 14, and the proposed model. For comparison, the ACI549 restriction (ε_f = 0.4 %) and the experimental result are also presented.

Table 5-7. Strengthening contribution predicted by the analytical models.

Method	Shear strengthening (kN)	Variation* (%)
ACI 549.4R-20 [23]	7.2	12 (lower)
ACI 549.4R-20 [23] (ε_f = 0.4 %)	1.5	82 (lower)
fib-Bulletin 14 [24]	88.8	983 (higher)
Proposed model	9.2	12 (higher)
Experimental result	8.2	-

*Variations based on the experimental result

The ACI549 model, considering ε_f = 0.4 %, truly underestimated the experimental results (82 % lower) and presented a significant variation regarding the prediction that adopted the original material modulus (79 %).

Comparing the ACI549 (without ε_f restriction) and the proposed model, it is noticeable that its predictions were approximate, while the *fib*-Bulletin 14 highly overestimated de experimental result. These behaviors were also observed by other authors [148] for PBO-FRCM applied as a structural shear strengthening. Escrig et al. [148] describes that the ACI549 model was conservative regarding the experimental results, presenting a variation range from 15 % to 21 % lower (using their real ε_f), while the *fib*-Bulletin 14 model reached a prediction 251 % higher (101.4 kN) than that obtained experimentally (28.9 kN). It may be related to the fact that the *fib*-Bulletin 14 model was originally developed for fiber-reinforced polymer composites.

The analytical model proposed in this study showed a reasonable accuracy considering the complexity of the mechanisms involved. However, it is feasible to affirm that it demands to be deeply analyzed to become more conservative before its application. Nevertheless, it showed the potential of the Iosipescu test for the

development of a model capable to predict the shear strengthening provided by fiber-cement composites applied as external reinforcement.

5.6. Conclusions

The cement-based composite reinforced with curauá fibers under the Iosipescu test showed a strain-hardening behavior with well defined mechanical stages. The composite performance was compared to another literature specimen, reinforced with carbon fibers, and presented higher shear stress capacity. About the cracking pattern, it was possible to observe an orientation changing along with its propagation, probably guided by the longitudinal alignment of the fibers.

For its use as external shear reinforcement, the applying method proved to be effective, presenting no signs of failure due to delamination or displacement. The composite reinforcement provided stiffness enhancement to the beam, which demonstrated a strengthening level comparable to other composite systems reinforced with synthetic fibers applied for structural strengthening.

The shear strengthened beam presented an irregular cracking pattern (staggered), creating different angles along with its propagation. However, due to the curauá fibers' flexibility, their angles were re-orientated, maintaining the shear strength enhancement.

The analytical study compared *fib*-Bulletin 14 and ACI549 models and proposed a new model based on the Iosipescu test. The ACI549 model showed the highest accuracy, while the *fib*-Bulletin model overestimated the experimental result. The proposed model also presented reasonable accuracy, but it needs to be corrected to provide more conservative results.

6. General Conclusions

This thesis presented the characterization results of natural fibers, as its application in cement-based composites. The mechanical behavior of these developed composites was widely analyzed and then applied as a structural reinforcement.

The curauá, hemp, and sisal fibers when exposed to 100 ^{o}C for 24 h, show an increase in resistance due to moisture loss. However, when exposure occurs above 100 ^{o}C up to 200 ^{o}C, the fibers lose their mechanical capacity, which goes against the definition of stability commonly suggested by the TG and XRD tests at the same range. Among the studied natural fibers, the curauá presented the best performance.

The cement-based composites reinforced with curauá fibers showed excellent mechanical results in general. The specimens' scale effect, in the tensile and flexural tests, did not show significant result variations, especially regarding their resistance. The overlap system proved to be effective, providing to the LP1000 the same strain-hardening behavior pattern observed in the other specimens. The application of the natural fiber composite as a structural reinforcement, under bending load tests, provided significant gains in strength and ductility. In addition, a better stress distribution was observed resulting in a yield delay of the steel rebars. The comparison of experimental results with the adopted theoretical model showedto be accurate.

The analysis of this composite under shear test showed a strain-hardening behavior with well defined mechanical stages. The material showed significant stress and strain capacity, consistent with that obtained in the previous tests. The application of this composite for the shear strengthening showed a markable increase, comparable with other reinforcement systems by synthetic fibers.

Finally, the cement-based composite reinforced with curauá fibers provided the expected mechanical improvement to structural beams. The used manufacturing and applying techniques did not demand industrial processes and can be manually reproduced, which reduced operational costs. The results of this work proved the

effectiveness of the developed natural fiber composite as a structural reinforcement, corroborating its high potential for structural applications.

References

[1] S.R. Ferreira, F. de A. Silva, P.R.L. Lima, R.D. Toledo Filho, Effect of hornification on the structure, tensile behavior and fiber matrix bond of sisal, jute and curauá fiber cement based composite systems, Constr. Build. Mater. 139 (2017) 551–561. doi:10.1016/j.conbuildmat.2016.10.004.

[2] S.R. Ferreira, F.D.A. Silva, P.R.L. Lima, R.D. Toledo Filho, Effect of fiber treatments on the sisal fiber properties and fiber-matrix bond in cement based systems, Constr. Build. Mater. 101 (2015) 730–740. doi:10.1016/j.conbuildmat.2015.10.120.

[3] M.E. Alves Fidelis, T.V.C. Pereira, O.D.F.M. Gomes, F. De Andrade Silva, R.D. Toledo Filho, The effect of fiber morphology on the tensile strength of natural fibers, J. Mater. Res. Technol. 2 (2013) 149–157. doi:10.1016/j.jmrt.2013.02.003.

[4] F. de A. Silva, B. Mobasher, R.D.T. Filho, Cracking mechanisms in durable sisal fiber reinforced cement composites, Cem. Concr. Compos. 31 (2009) 721–730. doi:10.1016/j.cemconcomp.2009.07.004.

[5] F.D.A. Silva, B. Mobasher, C. Soranakom, R.D.T. Filho, Effect of fiber shape and morphology on interfacial bond and cracking behaviors of sisal fiber cement based composites, Cem. Concr. Compos. 33 (2011) 814–823. doi:10.1016/j.cemconcomp.2011.05.003.

[6] F. de A. Silva, N. Chawla, R.D. de T. Filho, Tensile behavior of high performance natural (sisal) fibers, Compos. Sci. Technol. 68 (2008) 3438–3443. doi:10.1016/j.compscitech.2008.10.001.

[7] J.D.A.M. Filho, F.D.A. Silva, R.D. Toledo Filho, Degradation kinetics and aging mechanisms on sisal fiber cement composite systems, Cem. Concr. Compos. 40 (2013) 30–39. doi:10.1016/j.cemconcomp.2013.04.003.

[8] A. Komuraiah, N.S. Kumar, B.D. Prasad, Chemical Composition of Natural Fibers and its Influence on their Mechanical Properties, Mech. Compos. Mater. 50 (2014) 359–376. doi:10.1007/s11029-014-9422-2.

[9] B. Zukowski, F. de Andrade Silva, R.D. Toledo Filho, Design of strain hardening cement-based composites with alkali treated natural curauá fiber, Cem. Concr. Compos. 89 (2018) 150–159. doi:10.1016/j.cemconcomp.2018.03.006.

[10] H. Savastano Jr, V. Agopyan, A.M. Nolasco, L. Pimentel, Plant fibre reinforced cement components for roofing, Constr. Build. Mater. 13 (2000) 433–438. doi:10.1016/S0950-0618(99)00046-X.

[11] L.C. Roma, L.S. Martello, H. Savastano, Evaluation of mechanical, physical and thermal performance of cement-based tiles reinforced with vegetable fibers, Constr. Build. Mater. 22 (2008) 668–674. doi:10.1016/j.conbuildmat.2006.10.001.

[12] G.H.D. Tonoli, S.F. Santos, H. Savastano, S. Delvasto, R. Mejía De Gutiérrez, M.D.M. Lopez De Murphy, Effects of natural weathering on microstructure and mineral composition of cementitious roofing tiles reinforced with fique fibre, Cem. Concr. Compos. 33 (2011) 225–232.

doi:10.1016/j.cemconcomp.2010.10.013.
[13] P. Zak, T. Ashour, A. Korjenic, S. Korjenic, W. Wu, The influence of natural reinforcement fibers, gypsum and cement on compressive strength of earth bricks materials, Constr. Build. Mater. 106 (2016) 179–188. doi:10.1016/j.conbuildmat.2015.12.031.
[14] P.S. Kundu, S. Chakraborty, S. Chakraborty, Effectiveness of the surface modified jute fibre as fibre reinforcement in controlling the physical and mechanical properties of concrete paver blocks, Constr. Build. Mater. 191 (2018) 554–563. doi:10.1016/j.conbuildmat.2018.10.045.
[15] T. Jami, S.R. Karade, L.P. Singh, A review of the properties of hemp concrete for green building applications, J. Clean. Prod. 239 (2019) 117852. doi:10.1016/j.jclepro.2019.117852.
[16] E. Sassoni, S. Manzi, A. Motori, M. Montecchi, M. Canti, Novel sustainable hemp-based composites for application in the building industry : Physical , thermal and mechanical characterization, Energy Build. 77 (2014) 219–226. doi:10.1016/j.enbuild.2014.03.033.
[17] A.C. Abdullah, C.C. Lee, Effect of treatments on properties of cement-fiber bricks utilizing rice husk, corncob and coconut Coir, Procedia Eng. 180 (2017) 1266–1273. doi:10.1016/j.proeng.2017.04.288.
[18] Z.N. Azwa, B.F. Yousif, A.C. Manalo, W. Karunasena, A review on the degradability of polymeric composites based on natural fibres, Mater. Des. 47 (2013) 424–442. doi:10.1016/j.matdes.2012.11.025.
[19] L. Yan, B. Kasal, L. Huang, A review of recent research on the use of cellulosic fibres, their fibre fabric reinforced cementitious, geo-polymer and polymer composites in civil engineering, Compos. Part B Eng. 92 (2016) 94–132. doi:10.1016/j.compositesb.2016.02.002.
[20] M. El Messiry, S. El-Tarfawy, R. El Deeb, Study pultruded Jute fabric effect on the cementitious thin composites mechanical properties with low fiber volume fraction, Alexandria Eng. J. 56 (2017) 415–421. doi:10.1016/j.aej.2017.05.026.
[21] L. Oliveira de Souza, L.M. Silva de Souza, F. de Andrade Silva, Mechanics of Natural Curauá Textile Reinforced Concrete, Mag. Concr. Res. (2019) 1–31. doi:10.1680/jmacr.18.00473.
[22] C.L. Hwang, V.A. Tran, J.W. Hong, Y.C. Hsieh, Effects of short coconut fiber on the mechanical properties, plastic cracking behavior, and impact resistance of cementitious composites, Constr. Build. Mater. 127 (2016) 984–992. doi:10.1016/j.conbuildmat.2016.09.118.
[23] A. Kicińska-Jakubowska, E. Bogacz, J. Małgorzata, Review of Natural Fibers. Part I—Vegetable Fiberse, J. Nat. Fibers. 9 (2012) 150–167. doi:10.1080/15440478.2012.703370.
[24] J. Wei, C. Meyer, Degradation mechanisms of natural fiber in the matrix of cement composites, Cem. Concr. Res. 73 (2015) 1–16. doi:10.1016/j.cemconres.2015.02.019.
[25] U.G.K. Wegst, H. Bai, E. Saiz, A.P. Tomsia, R.O. Ritchie, Bioinspired structural materials, Nat. Mater. 14 (2015) 23–36. doi:10.1038/nmat4089.
[26] K. Liu, H. Takagi, R. Osugi, Z. Yang, Effect of lumen size on the effective transverse thermal conductivity of unidirectional natural fiber composites, Compos. Sci. Technol. 72 (2012) 633–639. doi:10.1016/j.compscitech.2012.01.009.
[27] S.R. Ferreira, F. de A. Silva, P.R.L. Lima, R.D. Toledo Filho, Effect of

Natural Fiber Hornification on the Fiber Matrix Interface in Cement Based Composite Systems, Key Eng. Mater. 668 (2015) 118–125. doi:10.4028/www.scientific.net/KEM.668.118.

[28] M.A. Pereira, Influência da Temperatura e Umidade nos Ciclos de Degradação Acelerada de Fibrocimentos com Cinza de Casca de Arroz Como Adição Mineral, Centro Federal de Educação Tecnológica de Minas Gerais – CEFET MG, 2011.

[29] J.A. Khan, M.A. Khan, The use of jute fibers as reinforcements in composites, in: Biofiber Reinf. Compos. Mater., Elsevier, 2015: pp. 3–34. doi:10.1533/9781782421276.1.3.

[30] T.H.. Sydenstricker, S. Mochnaz, S.C. Amico, Pull-out and other evaluations in sisal-reinforced polyester biocomposites, Polym. Test. 22 (2003) 375–380. doi:10.1016/S0142-9418(02)00116-2.

[31] D.B. Dittenber, H.V.S. Gangarao, Critical review of recent publications on use of natural composites in infrastructure, Compos. Part A Appl. Sci. Manuf. 43 (2012) 1419–1429. doi:10.1016/j.compositesa.2011.11.019.

[32] O. Onuaguluchi, N. Banthia, Plant-based natural fibre reinforced cement composites: A review, Cem. Concr. Compos. 68 (2016) 96–108. doi:10.1016/j.cemconcomp.2016.02.014.

[33] M.A.S. Spinacé, C.S. Lambert, K.K.G. Fermoselli, M.A. De Paoli, Characterization of lignocellulosic curaua fibres, Carbohydr. Polym. 77 (2009) 47–53. doi:10.1016/j.carbpol.2008.12.005.

[34] F. Yao, Q. Wu, Y. Lei, W. Guo, Y. Xu, Thermal decomposition kinetics of natural fibers: Activation energy with dynamic thermogravimetric analysis, Polym. Degrad. Stab. 93 (2008) 90–98. doi:10.1016/j.polymdegradstab.2007.10.012.

[35] V.A. Alvarez, A. Vázquez, Thermal degradation of cellulose derivatives/starch blends and sisal fibre biocomposites, Polym. Degrad. Stab. 84 (2004) 13–21. doi:10.1016/j.polymdegradstab.2003.09.003.

[36] L.B. Manfredi, E.S. Rodríguez, M. Wladyka-Przybylak, A. Vázquez, Thermal degradation and fire resistance of unsaturated polyester, modified acrylic resins and their composites with natural fibres, Polym. Degrad. Stab. 91 (2006) 255–261. doi:10.1016/j.polymdegradstab.2005.05.003.

[37] A.R. Martin, M. a. Martins, L.H.C. Mattoso, O.R.R.F. Silva, Caracterização química e estrutural de fibra de sisal da variedade Agave sisalana, Polímeros. 19 (2009) 40–46. doi:10.1590/S0104-14282009000100011.

[38] P. Krishnaiah, C.T. Ratnam, S. Manickam, Enhancements in crystallinity, thermal stability, tensile modulus and strength of sisal fibres and their PP composites induced by the synergistic effects of alkali and high intensity ultrasound (HIU) treatments, Ultrason. Sonochem. 34 (2017) 729–742. doi:10.1016/j.ultsonch.2016.07.008.

[39] S.R. Ferreira, P.R.L. Lima, F.A. Silva, R.D. Toledo Filho, Influência de ciclos molhagem-secagem em fibras de sisal sobre a aderência com matrizes de cimento Portland, Rev. Mater. 17 (2012) 1024–1034. doi:10.1590/S1517-70762012000200008.

[40] S.R. Ferreira, P.R.L. Lima, F.A. Silva, R.D. Toledo Filho, Effect of Sisal Fiber Hornification on the Fiber-Matrix Bonding Characteristics and Bending Behavior of Cement Based Composites, Key Eng. Mater. 600 (2014) 421–432. doi:10.4028/www.scientific.net/KEM.600.421.

[41] M.J. John, S. Thomas, Biofibres and biocomposites, Carbohydr. Polym. 71

(2008) 343–364. doi:10.1016/j.carbpol.2007.05.040.
[42] R.M. Kozlowski, M. Muzyczek, J. Walentowska, Flame Retardancy and Protection against Biodeterioration of Natural Fibers, in: Polym. Green Flame Retard., Elsevier, 2014: pp. 801–836. doi:10.1016/B978-0-444-53808-6.00023-8.
[43] J. Wei, C. Meyer, Degradation mechanisms of natural fiber in the matrix of cement composites, Cem. Concr. Res. 73 (2015) 1–16. doi:10.1016/j.cemconres.2015.02.019.
[44] M.C. Symington, W.M. Banks, D.W. Opukuro, R. a. Pethrick, Tensile testing of cellulose based natural fibers for structural composite applications, J. Compos. Mater. 43 (2009) 1083–1108. doi:10.1177/0021998308097740.
[45] K.J. Wong, B.F. Yousif, K.O. Low, The effects of alkali treatment on the interfacial adhesion of bamboo fibres, Proc. Inst. Mech. Eng. Part L J. Mater. Des. Appl. 224 (2010) 139–148. doi:10.1243/14644207JMDA304.
[46] N. Herlina Sari, I.N.G. Wardana, Y.S. Irawan, E. Siswanto, Characterization of the Chemical, Physical, and Mechanical Properties of NaOH-treated Natural Cellulosic Fibers from Corn Husks, J. Nat. Fibers. 0478 (2017) 1–14. doi:10.1080/15440478.2017.1349707.
[47] A.M. Brandt, Fibre reinforced cement-based (FRC) composites after over 40 years of development in building and civil engineering, Compos. Struct. 86 (2008) 3–9. doi:10.1016/j.compstruct.2008.03.006.
[48] A. Ross, M. Cpeng, Steel fibre reinforced concrete (SFRC) – Quality , performance and specification, in: New Zeal. Concr. Conf., 2009: p. 7.
[49] J. Yang, J. Kim, D. Yoo, Performance of shotcrete containing amorphous fibers for tunnel applications, Tunn. Undergr. Sp. Technol. Inc. Trenchless Technol. Res. 64 (2017) 85–94. doi:10.1016/j.tust.2017.01.012.
[50] F.H. Wittmann, G.P.A.G. van Zijl, Durability of Strain-Hardening Fibre-Reinforced Cement-Based Composites (SHCC), Springer Netherlands, 2011. doi:10.1007/978-94-007-0338-4.
[51] V.C. Li, ENGINEERED CEMENTITIOUS COMPOSITES (ECC) – TAILORED COMPOSITES THROUGH MICROMECHANICAL MODELING, Fiber Reinf. Concr. Present Futur. Eds N. Banthia, A. Bentur, A. Mufti, Can. Soc. Civ. Eng. (1998) 64– 97.
[52] A. Bentur, S. Mindess, Fibre Reinforced Cementitious Composites, 2nd Ed, Taylor & Francis, New York, NY, USA, 2007.
[53] A.P. Fantilli, H. Mihashi, P. Vallini, Cement and Concrete Research Multiple cracking and strain hardening in fi ber-reinforced concrete under uniaxial tension, Cem. Concr. Res. 39 (2009) 1217–1229. doi:10.1016/j.cemconres.2009.08.020.
[54] I. LÖFGREN, Fibre-reinforced Concrete for Industrial Construction - a fracture mechanics approach to material testing and structural analysis, Chalmers University of Technology, 2005.
[55] V.. C. Li, Micromechanics of crack bridging in fibre-reinforced concrete, Mater. Struct. (1993) 486–494. doi:10.1007/bf02472808.
[56] Y. Yao, F.A. Silva, M. Butler, V. Mechtcherine, B. Mobasher, Tension stiffening in textile-reinforced concrete under high speed tensile loads, Cem. Concr. Compos. 64 (2015) 49–61. doi:10.1016/j.cemconcomp.2015.07.009.
[57] B. Mobasher, J. Pahilajani, A. Peled, Analytical simulation of tensile response of fabric reinforced cement based composites, Cem. Concr. Compos. 28 (2006) 77–89. doi:10.1016/j.cemconcomp.2005.06.007.

[58] S. Diamond, J. Huang, The ITZ in concrete ± a di € erent view based on image analysis and SEM observations, Cem. Concr. Compos. 23 (2001) 179–188. doi:10.1016/S0958-9465(00)00065-2.

[59] X.H. Wang, S. Jacobsen, J.Y. He, Z.L. Zahng, S.F. Lee, H.L. Lein, Application of nanoindentation testing to study of the interfacial transition zone in steel fi ber reinforced mortar, Cem. Concr. Res. 39 (2009) 701–715. doi:10.1016/j.cemconres.2009.05.002.

[60] L. Xu, F. Deng, Y. Chi, Nano-mechanical behavior of the interfacial transition zone between steel-polypropylene fiber and cement paste, Constr. Build. Mater. 145 (2017) 619–638. doi:10.1016/j.conbuildmat.2017.04.035.

[61] F. Lea, C. Desch, Lea's Chemistry of Cement and Concrete, Elsevier Science & Technology Books, 2004.

[62] S. Rocha, M. Pepe, E. Martinelli, F. De Andrade, R. Dias, T. Filho, Influence of natural fibers characteristics on the interface mechanics with cement based matrices, Compos. Part B. 140 (2018) 183–196. doi:10.1016/j.compositesb.2017.12.016.

[63] R. de S. Castoldi, L.M.S. de Souza, F. de Andrade Silva, Comparative study on the mechanical behavior and durability of polypropylene and sisal fiber reinforced concretes, Constr. Build. Mater. 211 (2019) 617–628. doi:10.1016/j.conbuildmat.2019.03.282.

[64] S.R. Ferreira, F.D.A. Silva, P.R.L. Lima, R.D. Toledo Filho, Effect of fiber treatments on the sisal fiber properties and fiber-matrix bond in cement based systems, Constr. Build. Mater. 101 (2015) 730–740. doi:10.1016/j.conbuildmat.2015.10.120.

[65] S. Singh, A. Shukla, R. Brown, Pullout behavior of polypropylene fibers from cementitious matrix, Cem. Concr. Res. 34 (2004) 1919–1925. doi:10.1016/j.cemconres.2004.02.014.

[66] D. Asprone, M. Durante, A. Prota, G. Manfredi, Potential of structural pozzolanic matrix – hemp fiber grid composites, 25 (2011) 2867–2874. doi:10.1016/j.conbuildmat.2010.12.046.

[67] M.E.A. Fidelis, DESENVOLVIMENTO E CARACTERIZAÇÃO MECÂNICA DE COMPÓSITOS CIMENTÍCIOS TÊXTEIS REFORÇADOS COM FIBRAS DE JUTA, Universidade Federal do Rio de Janeiro, 2014.

[68] M. Ernestina Alves Fidelis, F. de Andrade Silva, R. Dias Toledo Filho, S. Müller, V. Mechtcherine, The Mechanics of Natural Jute Textile Reinforced Concrete, in: W. Brameshuber (Ed.), 11th Int. Symp. Ferrocem. Text. Reinf. Concr. 3rd ICTRC, Aachen, 2015: pp. 255–266. https://publications.rwth-aachen.de/record/483483?ln=de.

[69] M.E.A. Fidelis, R.D. Toledo Filho, F. de A. Silva, V. Mechtcherine, M. Butler, S. Hempel, The effect of accelerated aging on the interface of jute textile reinforced concrete, Cem. Concr. Compos. 74 (2016) 7–15. doi:10.1016/j.cemconcomp.2016.09.002.

[70] A.L.S. d'Almeida, J.A. Melo Filho, R.D. Toledo Filho, Use of Curaua Fibers as Reinforcement in Cement Composites, Chem. Eng. Trans. 17 (2009) 1717–1722. doi:10.3303/CET0917287.

[71] D.G. Soltan, P. das Neves, A. Olvera, H. Savastano Junior, V.C. Li, Introducing a curauá fiber reinforced cement-based composite with strain-hardening behavior, Ind. Crops Prod. 103 (2017) 1–12. doi:10.1016/j.indcrop.2017.03.016.

[72] R.S. Olivito, O.A. Cevallos, A. Carrozzini, Development of durable cementitious composites using sisal and flax fabrics for reinforcement of masonry structures, J. Mater. 57 (2014) 258–268. doi:10.1016/j.matdes.2013.11.023.
[73] K.M. Sadiq, D.K.H. Bzeni, F.U.A. Shaikh, Deflection hardening behaviour of jute strands reinforced lightweight cementitious composite, Constr. Build. Mater. 96 (2015) 102–111. doi:10.1016/j.conbuildmat.2015.08.004.
[74] J.D.A.M. Filho, F.D.A. Silva, R.D. Toledo Filho, Degradation kinetics and aging mechanisms on sisal fiber cement composite systems, Cem. Concr. Compos. 40 (2013) 30–39. doi:10.1016/j.cemconcomp.2013.04.003.
[75] J. Wei, D. Ph, B. Gencturk, D. Ph, A.M. Asce, Degradation of Natural Fiber in Cement Composites Containing Diatomaceous Earth, 30 (2018) 1–17. doi:10.1061/(ASCE)MT.1943-5533.0002486.
[76] J. Claramunt, R. Dias, T. Filho, Cellulosic fiber reinforced cement-based composites : A review of recent, 79 (2015) 115–128. doi:10.1016/j.conbuildmat.2015.01.035.
[77] R.D. Toledo Filho, F. d A. Silva, E.M.R. Fairbairn, J. d A.M. Filho, Durability of compression molded sisal fiber reinforced mortar laminates, Constr. Build. Mater. 23 (2009) 2409–2420. doi:10.1016/j.conbuildmat.2008.10.012.
[78] B.J. Mohr, H. Nanko, K.E. Kurtis, Durability of kraft pulp fiber – cement composites to wet / dry cycling, Cem. Concr. Compos. 27 (2005) 435–448. doi:10.1016/j.cemconcomp.2004.07.006.
[79] B.J. Mohr, J.J. Biernacki, K.E. Kurtis, Microstructural and chemical effects of wet/dry cycling on pulp fiber-cement composites, Cem. Concr. Res. 36 (2006) 1240–1251. doi:10.1016/j.cemconres.2006.03.020.
[80] J. Claramunt, M. Ardanuy, J.A. Garc??a-Hortal, R.D.T. Filho, The hornification of vegetable fibers to improve the durability of cement mortar composites, Cem. Concr. Compos. 33 (2011) 586–595. doi:10.1016/j.cemconcomp.2011.03.003.
[81] J. Wei, C. Meyer, Sisal fiber-reinforced cement composite with Portland cement substitution by a combination of metakaolin and nanoclay, J. Mater. Sci. 49 (2014) 7604–7619. doi:10.1007/s10853-014-8469-8.
[82] P.R.L. Lima, R.D. Toledo Filho, Uso de metacaulinita para incremento da durabilidade de compósitos à base de cimento reforçados com fibras de sisal, Assoc. Nac. Tecnol. Do Ambient. Construído. 8 (2008) 7–19.
[83] B.J. Mohr, J.J. Biernacki, K.E. Kurtis, Supplementary cementitious materials for mitigating degradation of kraft pulp fiber-cement composites, Cem. Concr. Res. 37 (2007) 1531–1543. doi:10.1016/j.cemconres.2007.08.001.
[84] F. de A. Silva, R.D.T. Filho, J. de A.M. Filho, E. de M.R. Fairbairn, Physical and mechanical properties of durable sisal fiber-cement composites, Constr. Build. Mater. 24 (2010) 777–785. doi:10.1016/j.conbuildmat.2009.10.030.
[85] G.H.D. Tonoli, V.D. Pizzol, G. Urrea, S.F. Santos, L.M. Mendes, V. Santos, V.M. John, Rationalizing the impact of aging on fiber – matrix interface and stability of cement-based composites submitted to carbonation at early ages, J Mater Sci. (2016) 7929–7943. doi:10.1007/s10853-016-0060-z.
[86] R. Tolêdo Filho, K. Ghavami, G.L. England, K. Scrivener, Development of vegetable fibre-mortar composites of improved durability, Cem. Concr. Compos. 25 (2003) 185–196. doi:10.1016/S0958-9465(02)00018-5.
[87] K. Ghavami, Ultimate Load Behavior of Bamboo-Reinforced Lightweight

Concrete Beams, Cem. Concr. Compos. 17 (1995) 281–288. http://gateway.isiknowledge.com/gateway/Gateway.cgi?GWVersion=2&SrcAuth=AegeanSoftware&SrcApp=NoteExpress&DestLinkType=FullRecord&DestApp=WOS&KeyUT=A1995TF62600004.

[88] K. Bilba, M.-A. Arsene, Silane treatment of bagasse fiber for reinforcement of cementitious composites, Compos. Part A Appl. Sci. Manuf. 39 (2008) 1488–1495. doi:10.1016/j.compositesa.2008.05.013.

[89] A.E. Naaman, HIGH PERFORMANCE FIBER REINFORCED CEMENT COMPOSITES: CLASSIFICATION AND APPLICATIONS DEFINITION, in: CBM-CI Int. Work., Karachi, Pakistan, 2008: pp. 389–401.

[90] B. Aggregate, M. Sassu, L. Giresini, E. Bonannini, M.L. Puppio, On the Use of Vibro-Compressed Units with Bio-Natural Aggregate, 34 (2016). doi:10.3390/buildings6030040.

[91] P.R.L. Lima, J.A.O. Barros, A.B. Roque, C.M.A. Fontes, J.M.F. Lima, Short sisal fiber reinforced recycled concrete block for one-way precast concrete slabs, Constr. Build. Mater. 187 (2018) 620–634. doi:10.1016/j.conbuildmat.2018.07.184.

[92] A. Duval, A. Bourmaud, L. Augier, C. Baley, Influence of the sampling area of the stem on the mechanical properties of hemp fibers, Mater. Lett. 65 (2011) 797–800. doi:10.1016/j.matlet.2010.11.053.

[93] M. Liu, D. Fernando, A.S. Meyer, B. Madsen, G. Daniel, A. Thygesen, Characterization and biological depectinization of hemp fibers originating from different stem sections, Ind. Crops Prod. 76 (2015) 880–891. doi:10.1016/j.indcrop.2015.07.046.

[94] H. Yang, Characteristics of hemicellulose , cellulose and lignin pyrolysis, 86 (2007) 1781–1788. doi:10.1016/j.fuel.2006.12.013.

[95] F. Collard, J. Blin, A review on pyrolysis of biomass constituents : Mechanisms and composition of the products obtained from the conversion of cellulose , hemicelluloses and lignin, Renew. Sustain. Energy Rev. 38 (2014) 594–608. doi:10.1016/j.rser.2014.06.013.

[96] S.A.O. Cristian, B.M.Y. Combariza, Exploring the composition of raw and deligni fi ed Colombian fi que fi bers , tow and pulp, Cellulose. (2017). doi:10.1007/s10570-017-1599-9.

[97] J. Yu, N. Paterson, J. Blamey, M. Millan, Cellulose , xylan and lignin interactions during pyrolysis of lignocellulosic biomass, Fuel. 191 (2017) 140–149. doi:10.1016/j.fuel.2016.11.057.

[98] V. Placet, Characterization of the thermo-mechanical behaviour of Hemp fibres intended for the manufacturing of high performance composites, Compos. Part A Appl. Sci. Manuf. 40 (2009) 1111–1118. doi:10.1016/j.compositesa.2009.04.031.

[99] American Society for Testing and Materials, Standard Test Method for Tensile Strength and Young's Modulus of Fibers, Astm C1557-14. (2014) 1–10. doi:10.1520/C1557-14.2.

[100] F. Martins, F.P. Teixeira, J.F. Lima, F. de A. Silva, ON THE MEASUREMENT OF CROSS-SECTIONAL AREA OF NATURAL FIBERS, in: Rio de Janeiro, 2018: pp. 1–8. doi:10.21452/bccm4.2018.10.10.

[101] J. Schindelin, I. Arganda-carreras, P. Vasco, E. Herriko, J. Schindelin, I. Arganda-carreras, E. Frise, V. Kaynig, Fiji: An Open-Source Platform for Biological- Image Analysis, Nat. Methods. 9 (2012) 676–682.

doi:10.1038/nmeth.2019.
[102] C.A. Schneider, W.S. Rasband, K.W. Eliceiri, NIH Image to ImageJ: 25 years of image analysis, Nat. Methods. 9 (2012) 671–675. doi:10.1038/nmeth.2089.
[103] T. Zimmermann, E. Pöhler, T. Geiger, Cellulose fibrils for polymer reinforcement, Adv. Eng. Mater. 6 (2004) 754–761. doi:10.1002/adem.200400097.
[104] M.D.H. Beg, K.L. Pickering, Accelerated weathering of unbleached and bleached Kraft wood fibre reinforced polypropylene composites, Polym. Degrad. Stab. 93 (2008) 1939–1946. doi:10.1016/j.polymdegradstab.2008.06.012.
[105] H.L. Ornaghi, M. Poletto, A.J. Zattera, S.C. Amico, Correlation of the thermal stability and the decomposition kinetics of six different vegetal fibers, Cellulose. 21 (2014) 177–188. doi:10.1007/s10570-013-0094-1.
[106] S.A. Ovalle-serrano, F.N. Gómez, C. Blanco-tirado, M.Y. Combariza, Isolation and characterization of cellulose nano fi brils from Colombian Fique decortication by-products, Carbohydr. Polym. 189 (2018) 169–177. doi:10.1016/j.carbpol.2018.02.031.
[107] S. Park, J.O. Baker, M.E. Himmel, P.A. Parilla, D.K. Johnson, Cellulose crystallinity index: measurement\ntechniques and their impact on interpreting\ncellulase performance, Biotechnol. Biofuels. 3 (2010) 1–10. http://www.biotechnologyforbiofuels.com/content/3/1/10%5Cnfile:///C:/Users/takehiko/Desktop/Cellulose crystallinity index_measurement techniques and their impact on interpreting cellulase performance.pdf.
[108] M. Poletto, H.L. Ornaghi Júnior, A.J. Zattera, Native cellulose: Structure, characterization and thermal properties, Materials (Basel). 7 (2014) 6105–6119. doi:10.3390/ma7096105.
[109] J.P.V. Diaz, F. de A. Silva, J.R.M. D'Almeida, Effect of Peach Palm Fiber Microstructure on its Tensile Behavior, BioResources. 11 (2016) 10140–10157. doi:10.15376/biores.11.4.10140-10157.
[110] B. Puangsin, Q. Yang, T. Saito, A. Isogai, International Journal of Biological Macromolecules Comparative characterization of TEMPO-oxidized cellulose nanofibril films prepared from non-wood resources, Int. J. Biol. Macromol. 59 (2013) 208–213. doi:10.1016/j.ijbiomac.2013.04.016.
[111] Y. Xue, Y. Du, S. Elder, K. Wang, J. Zhang, Temperature and loading rate effects on tensile properties of kenaf bast fiber bundles and composites, Compos. Part B Eng. 40 (2009) 189–196. doi:10.1016/j.compositesb.2008.11.009.
[112] M.F.M. Zain, M.M. Hossain, M.R. Karim, M. Hasan, M.K. Hossain, Durability of mortar and concrete made up of pozzolans as a partial replacement of cement: A review, Constr. Build. Mater. 116 (2016) 128–140. doi:10.1016/j.conbuildmat.2016.04.147.
[113] C. Kulasuriya, V. Vimonsatit, W.P.S. Dias, P. De Silva, Design and development of Alkali Pozzolan Cement (APC), Constr. Build. Mater. 68 (2014) 426–433. doi:10.1016/j.conbuildmat.2014.06.095.
[114] M. Valipour, F. Pargar, M. Shekarchi, S. Khani, Comparing a natural pozzolan , zeolite , to metakaolin and silica fume in terms of their effect on the durability characteristics of concrete : A laboratory study, Constr. Build. Mater. 41 (2013) 879–888. doi:10.1016/j.conbuildmat.2012.11.054.
[115] J.J. Chang, W. Yeih, T.J. Chung, R. Huang, Properties of pervious concrete

made with electric arc furnace slag and alkali-activated slag cement, Constr. Build. Mater. 109 (2016) 34–40. doi:10.1016/j.conbuildmat.2016.01.049.
[116] F.P. Teixeira, O. da F.M. Gomes, F. de A. Silva, Degradation Mechanisms of Curaua, Hemp, and Sisal Fibers Exposed to Elevated Temperatures, BioResources. 14 (2019) 1494–1511. doi:10.15376/biores.14.1.1494-1511.
[117] J. Wei, C. Meyer, Degradation rate of natural fiber in cement composites exposed to various accelerated aging environment conditions, Corros. Sci. 88 (2014) 118–132. doi:10.1016/j.corsci.2014.07.029.
[118] R.D. Toledo Filho, K. Ghavami, M.A. Sanjuán, G.L. England, Free, restrained and drying shrinkage of cement mortar composites reinforced with vegetable fibres, Cem. Concr. Compos. 27 (2005) 537–546. doi:10.1016/j.cemconcomp.2004.09.005.
[119] O. Onuaguluchi, N. Banthia, Plant-based natural fibre reinforced cement composites: A review, Cem. Concr. Compos. 68 (2016) 96–108. doi:10.1016/j.cemconcomp.2016.02.014.
[120] R.D.T. Filho, M.A. Sanjuán, Effect of low modulus sisal and polypropylene fibre on the free and restrained shrinkage of mortars at early age, Cem. Concr. Res. 29 (1999) 1597–1604. doi:10.1016/S0008-8846(99)00136-2.
[121] H. Singh, R. Gupta, Influence of cellulose fiber addition on self-healing and water permeability of concrete, Case Stud. Constr. Mater. 12 (2020). doi:10.1016/j.cscm.2019.e00324.
[122] L. Souza, L. Souza, F. Silva, Autogenous healing capability of natural curauá textile reinforced concrete, in: Procedia Eng., Elsevier B.V., 2017: pp. 290–294. doi:10.1016/j.proeng.2017.07.041.
[123] Y.Y. Kim, B.Y. Lee, J.W. Bang, B.C. Han, L. Feo, C.G. Cho, Flexural performance of reinforced concrete beams strengthened with strain-hardening cementitious composite and high strength reinforcing steel bar, Compos. Part B Eng. 56 (2014) 512–519. doi:10.1016/j.compositesb.2013.08.069.
[124] H. Do Yun, Flexural behavior and crack-damage mitigation of plain concrete beam with a strain-hardening cement composite (SHCC) layer at tensile region, Compos. Part B Eng. 45 (2013) 377–387. doi:10.1016/j.compositesb.2012.05.053.
[125] S.K. Shin, J.J.H. Kim, Y.M. Lim, Investigation of the strengthening effect of DFRCC applied to plain concrete beams, Cem. Concr. Compos. 29 (2007) 465–473. doi:10.1016/j.cemconcomp.2007.02.005.
[126] F. Schladitz, M. Frenzel, D. Ehlig, M. Curbach, Bending load capacity of reinforced concrete slabs strengthened with textile reinforced concrete, Eng. Struct. 40 (2012) 317–326. doi:10.1016/j.engstruct.2012.02.029.
[127] S.W. Kim, H. Do Yun, Crack-damage mitigation and flexural behavior of flexure-dominant reinforced concrete beams repaired with strain-hardening cement-based composite, Compos. Part B Eng. 42 (2011) 645–656. doi:10.1016/j.compositesb.2011.02.022.
[128] F. Tomczak, K.G. Satyanarayana, T.H.D. Sydenstricker, Studies on lignocellulosic fibers of Brazil: Part III - Morphology and properties of Brazilian curauá fibers, Compos. Part A Appl. Sci. Manuf. 38 (2007) 2227–2236. doi:10.1016/j.compositesa.2007.06.005.
[129] M.A.S. Spinacé, L.G. Janeiro, F.C. Bernardino, T.A. Grossi, M.A. De Paoli, Poliolefinas reforçadas com fibras vegetais curtas: Sisal vs. curauá, Polimeros. 21 (2011) 168–174. doi:10.1590/S0104-14282011005000036.

[130] M.C. Gutiérrez, M.A. De Paoli, M.I. Felisberti, Cellulose acetate and short curauá fibers biocomposites prepared by large scale processing: Reinforcing and thermal insulating properties, Ind. Crops Prod. 52 (2014) 363–372. doi:10.1016/j.indcrop.2013.10.054.
[131] ABNT NBR 16697, ABNT NBR 16697 Cimento Portland – Requisitos, Cim. Portl. – Requisitos. (2018).
[132] V.N. Lima, D.C.T. Cardoso, F.A. Silva, Flexural creep behavior of steel and polypropylene fiber reinforced concrete, in: Proc. 10th Int. Conf. Fract. Mech. Concr. Concr. Struct., IA-FraMCoS, 2019: p. 7. doi:10.21012/FC10.234778.
[133] ASTM International, ASTM Standard D6641/D6641M-14: Compressive Properties of Polymer Matrix Composite Materials Using a Combined Loading Compression (CLC) Test Fixture, (2014) 13. doi:10.1520/D6641.
[134] B. Boulekbache, M. Hamrat, M. Chemrouk, S. Amziane, Flexural behaviour of steel fibre-reinforced concrete under cyclic loading, Constr. Build. Mater. 126 (2016) 253–262. doi:10.1016/j.conbuildmat.2016.09.035.
[135] H.A. Bruck, S.R. McNeill, M.A. Sutton, W.H. Peters, Digital image correlation using Newton-Raphson method of partial differential correction, Exp. Mech. 29 (1989) 261–267. doi:10.1007/BF02321405.
[136] M. Sutton, W. Wolters, W. Peters, W. Ranson, S. McNeill, Determination of displacements using an improved digital correlation method, Image Vis. Comput. 1 (1983) 133–139. doi:10.1016/0262-8856(83)90064-1.
[137] M.E.A. Fidelis, F.D.A. Silva, R.D. Toledo Filho, The Influence of Fiber Treatment on the Mechanical Behavior of Jute Textile Reinforced Concrete, Key Eng. Mater. 600 (2014) 469–474. doi:10.4028/www.scientific.net/KEM.600.469.
[138] Z. Soric, J. Galic, T. Rukavina, Determination of tensile strength of glass fiber straps, Mater. Struct. 41 (2008) 879–890. doi:10.1617/s11527-007-9291-4.
[139] B. Mobasher, A. Bonakdar, M. Bakhshi, Back-calculation procedure for cyclic flexural fracture tests in fiber reinforced concrete, in: Fract. Mech. Appl. Concr., ACI Technical Publication, 2015. https://linkinghub.elsevier.com/retrieve/pii/S0360132310003549.
[140] S.H. Said, H.A. Razak, I. Othman, Strength and deformation characteristics of engineered cementitious composite slabs with different polymer fibres, J. Reinf. Plast. Compos. 34 (2015) 1950–1962. doi:10.1177/0731684415607393.
[141] BRITISH STANDARD. BS EN 1992-1-1:2004, Eurocode 2: Design of concrete structures – Part 1-1: General rules and rules for buildings, 3 (2004) 230.
[142] Y. Yao, F.A. Silva, M. Butler, V. Mechtcherine, B. Mobasher, Tension stiffening in textile-reinforced concrete under high speed tensile loads, Cem. Concr. Compos. 64 (2015) 49–61. doi:10.1016/j.cemconcomp.2015.07.009.
[143] R. Guo, L. Cai, S. Hino, B. Wang, Experimental Study on Shear Strengthening of RC Beams with an FRP Grid-PCM Reinforcement Layer, Appl. Sci. 9 (2019) 2984. doi:10.3390/app9152984.
[144] American Concrete Institute, ACI 549.4R-20: Guide to Design and Construction of Externally Bonded Fabric-Reinforced Cementitious Matrix and Steel-Reinforced Grout Systems for Repair and Strengthening of Concrete Structures, 2020.

[145] fib Task Group 9.3 FRP Reinforcement for Concrete Structures, fib-Bulletin 14: Externally Bonded FRP Reinforcement for RC Structures, 2011.
[146] H.K. Lee, S.H. Cheong, S.K. Ha, C.G. Lee, Behavior and performance of RC T-section deep beams externally strengthened in shear with CFRP sheets, Compos. Struct. 93 (2011) 911–922. doi:10.1016/j.compstruct.2010.07.002.
[147] R. Contamine, A.S. Larbi, P. Hamelin, Identifying the contributing mechanisms of textile reinforced concrete (TRC) in the case of shear repairing damaged and reinforced concrete beams, Eng. Struct. 46 (2013) 447–458. doi:10.1016/j.engstruct.2012.07.024.
[148] C. Escrig, L. Gil, E. Bernat-maso, F. Puigvert, Experimental and analytical study of reinforced concrete beams shear strengthened with different types of textile-reinforced mortar, Constr. Build. Mater. 83 (2015) 248–260. doi:10.1016/j.conbuildmat.2015.03.013.
[149] G. Loreto, S. Babaeidarabad, L. Leardini, A. Nanni, ORIGINAL RESEARCH RC beams shear-strengthened with fabric-reinforced-cementitious-matrix (FRCM) composite, Int. J. Adv. Struct. Eng. 7 (2015) 341–352. doi:10.1007/s40091-015-0102-9.
[150] L. Ombres, Structural performances of reinforced concrete beams strengthened in shear with a cement based fiber composite material, Compos. Struct. 122 (2015) 316–329. doi:10.1016/j.compstruct.2014.11.059.
[151] R. Azam, K. Soudki, S. West, M. Noël, Shear strengthening of RC deep beams with cement-based composites, 172 (2018) 929–937. doi:10.1016/j.engstruct.2018.06.085.
[152] O. Onuaguluchi, N. Banthia, Plant-based natural fibre reinforced cement composites: A review, Cem. Concr. Compos. 68 (2016) 96–108. doi:10.1016/j.cemconcomp.2016.02.014.
[153] L. Yan, B. Kasal, L. Huang, A review of recent research on the use of cellulosic fibres, their fibre fabric reinforced cementitious, geo-polymer and polymer composites in civil engineering, Compos. Part B Eng. 92 (2016) 94–132. doi:10.1016/j.compositesb.2016.02.002.
[154] A. International, ASTM Standard D5379/D5379M-12: Standard test method for shear properties of composite materials by the V-notched beam method, (2014) 1–14. doi:10.1520/D5379.
[155] H. Baghi, J.A.O. Barros, Shear Properties of the Strain Hardening Cementitious Composite Material, J. Mater. Civ. Eng. 28 (2016) 1–13. doi:10.1061/(ASCE)MT.1943-5533.0001603.
[156] F. Isla, G. Ruano, B. Luccioni, Analysis of steel fibers pull-out. Experimental study, Constr. Build. Mater. 100 (2015) 183–193. doi:10.1016/j.conbuildmat.2015.09.034.